

AD-A213 973

WRDC-TR-89-4072

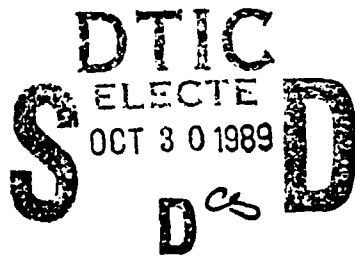
CARBON FIBER MORPHOLOGY: WIDE-ANGLE  
X-RAY STUDIES OF PITCH- AND PAN-BASED  
CARBON FIBERS

Dr. David P. Anderson

University of Dayton Research Institute  
300 College Park Avenue  
Dayton, OH 45469-0001

July 1989

Interim Report for Period January 1988 - December 1988



Approved for public release; distribution unlimited.

MATERIALS LABORATORY  
WRIGHT RESEARCH AND DEVELOPMENT CENTER  
AIR FORCE SYSTEMS COMMAND  
WRIGHT-PATTERSON AIR FORCE BASE, OHIO 45433-6533

DTIC FILE COPY

1



89 10 27 192

NOTICE

When Government drawings, specifications, or other data are used for any purpose other than in connection with a definitely Government-related procurement, the United States Government incurs no responsibility or any obligation whatsoever. The fact that the Government may have formulated or in any way supplied the said drawings, specifications, or other data, is not to be regarded by implication, or otherwise in any manner construed, as licensing the holder, or any other person or corporation; or as conveying any rights or permission to manufacture, use, or sell any patented invention that may in any way be related thereto.

This report is releasable to the National Technical Information Service (NTIS). At NTIS, it will be available to the general public, including foreign nations.

This technical report has been reviewed and is approved for publication.

*Marvin Knight*

MARVIN KNIGHT, Project Engineer  
Mechanics & Surface Interactions Br  
Nonmetallic Materials Division

FOR THE COMMANDER

*Dr. S. Eichelman Jr.*

MERRILL L. MINGES  
Director  
Nonmetallic Materials Division

If your address has changed, if you wish to be removed from our mailing list, or if the addressee is no longer employed by your organization, please notify WRDC/MILBM, Wright-Patterson AFB, OH 45433-6533 to help maintain a current mailing list.

Copies of this report should not be returned unless return is required by security considerations, contractual obligations, or notice on a specific document.

## UNCLASSIFIED

SECURITY CLASSIFICATION OF THIS PAGE

Form Approved  
OMB No. 0704-0188

## REPORT DOCUMENTATION PAGE

1a. REPORT SECURITY CLASSIFICATION Unclassified		1b. RESTRICTIVE MARKINGS	
2a. SECURITY CLASSIFICATION AUTHORITY		3. DISTRIBUTION/AVAILABILITY OF REPORT Approved for public release; distribution unlimited.	
2b. DECLASSIFICATION/DOWNGRADING SCHEDULE			
4. PERFORMING ORGANIZATION REPORT NUMBER(S) UDR-TR-89-61		5. MONITORING ORGANIZATION REPORT NUMBER(S) WRDC-TR-89-4072	
6a. NAME OF PERFORMING ORGANIZATION University of Dayton Research Institute	6b. OFFICE SYMBOL (If applicable)	7a. NAME OF MONITORING ORGANIZATION Materials Laboratory (WRDC/MLBM) Wright Research and Development Center	
6c. ADDRESS (City, State, and ZIP Code) 300 College Park Avenue Dayton, OH 45469-0001		7b. ADDRESS (City, State, and ZIP Code) Air Force Systems Command Wright-Patterson AFB, OH 45433-6533	
8a. NAME OF FUNDING/SPONSORING ORGANIZATION Materials Laboratory Wright Research & Devel. Center	8b. OFFICE SYMBOL (If applicable) WRDC/MLBM	9. PROCUREMENT INSTRUMENT IDENTIFICATION NUMBER F33615-87-C-5239	
8c. ADDRESS (City, State, and ZIP Code) Air Force Systems Command Wright-Patterson AFB, OH 45433-6533		10. SOURCE OF FUNDING NUMBERS	
		PROGRAM ELEMENT NO. 62102F	PROJECT NO. 2419
		TASK NO. 02	WORK UNIT ACCESSION NO. 25
11. TITLE (Include Security Classification) CARBON FIBER MORPHOLOGY: WIDE-ANGLE X-RAY STUDIES OF PITCH- AND PAN-BASED CARBON FIBERS			
12. PERSONAL AUTHOR(S) Dr. David P. Anderson			
13a. TYPE OF REPORT Interim	13b. TIME COVERED FROM Jan 88 TO Dec 88	14. DATE OF REPORT (Year, Month, Day) July 1989	15. PAGE COUNT 119
16. SUPPLEMENTARY NOTATION <i>... by ...</i>			
17. COSATI CODES		18. SUBJECT TERMS (Continue on reverse if necessary and identify by block number) carbon fibers; graphite fiber; x-ray diffraction crystals; graphitization crystallite size; orientation	
19. ABSTRACT (Continue on reverse if necessary and identify by block number)  This report describes the wide-angle x-ray diffraction techniques used to examine carbon and graphite fibers and the results of several fibers. A series of commercial PAN- and pitch-based carbon fibers whose tensile moduli spanned the generally available range were examined. Crystal perfection, size, orientation, and degree of graphitization correlated well with tensile moduli but less well with tensile and compressive strength.			
20. DISTRIBUTION/AVAILABILITY OF ABSTRACT <input checked="" type="checkbox"/> UNCLASSIFIED/UNLIMITED <input type="checkbox"/> SAME AS RPT. <input type="checkbox"/> DTIC USERS		21. ABSTRACT SECURITY CLASSIFICATION Unclassified	
22a. NAME OF RESPONSIBLE INDIVIDUAL Marvin Knight		22b. TELEPHONE (Include Area Code) (513)255-7131	22c. OFFICE SYMBOL WRDC/MLBM

## FOREWORD

This Interim Technical Report was prepared by the University of Dayton Research Institute, 300 College Park Avenue, Dayton, OH 45469-0001, under Air Force Contract No. F33615-87-C-5239. It was administered under the direction of the Materials Laboratory, Wright Research and Development Center, Air Force Systems Command, Wright-Patterson Air Force Base, OH, with Mr. Marvin Knight (WRDC/MLBM) as the Project Engineer.

The use of commercial names of materials in this report is included for completeness and ease of scientific comparison only. It in no way constitutes an endorsement of these materials or manufacturers.

This report covers work conducted from January through December 1988.



Accession For	
NTIS	CRAB <sup>2</sup> <input checked="" type="checkbox"/>
DTIC TAB	<input type="checkbox"/>
Unclassified	<input type="checkbox"/>
Classification	
By	
Distribution /	
Availability Codes	
Dist	Aval and/or Special
A-1	

#### **ACKNOWLEDGEMENTS**

The author would like to thank Dr. Satish Kumar of UDRI and especially Major Joseph Hager of WRDC/MLBC for comments and criticisms on this report during its assembly.

## TABLE OF CONTENTS

SECTION	PAGE
1      INTRODUCTION	1
2      NOMENCLATURE	3
2.1    Hexagonal Indexing	3
2.2    Diffractometer	6
2.3    Fiber Diffraction	11
3      CARBON/GRAphite REFLECTIONS	19
3.1    Graphite Crystals	19
3.2    Two-Dimensional Lattices	25
3.3    Crystallite Sizes	26
3.4    Misorientation	33
4      RESULTS	40
4.1    Materials	40
4.2    (00,2) Results	40
4.3    Advanced $L_c$ Results	45
4.4    3-D and $L_a$ Results	51
4.5    Other	66
5      CONCLUSIONS	67
REFERENCES	68
APPENDIX A: Flat-Film WAXD Photographs of Carbon Fibers	71
APPENDIX B: Diffraction Scans ( $\chi=70^\circ$ ) of the (10) and (10,1) Region of the Carbon Fibers	79
APPENDIX C: Diffraction Scans ( $\chi=70^\circ$ ) of the (11) and (11,2) Region of the Carbon Fibers	95

## LIST OF ILLUSTRATIONS

FIGURE	PAGE
1 Hexagonal Axes and Crystal Planes in the Graphite Basal Plane	4
2 Diagrams of Planes Having Various Miller Indices in an Orthorhombic Unit Cell With Edges a, b, and c	5
3 Bragg's Law Diffraction	7
4 Schematic of X-ray Flat-Film Camera ( $S_1$ , $S_2$ , and $S_3$ are the camera's collimator)	9
5 Flat-Film WAXD Photograph of P-100 Carbon Fiber	9
6 Four-Circle Diffractometer Geometry With a Fiber Sample	10
7 Equatorial Diffraction Geometry	12
8 Meridional Diffraction Geometry	14
9 Cone Defined by Fiber Off-Axis Plane Normals	15
10 Off-Axis Diffraction Geometry - Omega Circle Adjustments	16
11 Off-Axis Diffraction Geometry - Chi Circle Adjustments	17
12 Comparison of Turbostratic and 3-D Graphite Crystals in Carbon Fibers	20
13 The Entwined Fibrils Model of Carbon Fiber Morphology of Diefendorf and Tokarsky	22
14 The Wavy Fibrils Model of Carbon Fiber Morphology of Perret et al.	22
15 The Thumb-Print Cross-Section Model of Carbon Fiber Morphology of Bacon	23
16 The Holey Curved Bundles of Graphite Sheets Model of Carbon Fiber Morphology of Barnet and Noor	23
17 The Holey Curved Bundles of Graphite Sheets Model of Carbon Fiber Morphology of Bennett and Johnson	24

LIST OF ILLUSTRATIONS (Continued)

FIGURE	PAGE
18      Theoretical Intensity Profiles of the 2-D Graphite (11) Peak from Randomly Oriented Crystals of Several Sizes	27
19      Intensity Distribution from 2-D Crystal Sheets Oriented Parallel to the Fiber Axis	28
20      Comparison Between Gaussian and Cauchy Distributions	30
21      Curve-Fit Beryllium Acetate Diffraction Scan Used to Measure Instrumental Broadening Effects	32
22      Theoretical (00,2) Reflection With and Without Instrumental Broadening Folded in for $L_C = 100\text{\AA}$	34
23      Theoretical Asymmetric 2-D Profile With and Without Instrumental Broadening Folded in for $L_a = 100\text{\AA}$	35
24      Typical Fiber Sample Bundles: a) Mounted With Tape at Fiber Ends and b) Mounted in Cyanomethyl-acrylate Glue	36
25      Plots of (00,2) Azimuthal Distributions for P-25 and P-100 Carbon Fibers	38
26      Curve-Fit (00,2) Bragg Reflection of P-55	43
27      Curve-Fit (00,2) Azimuthal Scan of P-55	44
28      Complete Equatorial Bragg Scan of P-100	46
29      Hosemann Plot for P-55 Assuming a Gaussian Distribution for Crystalline Disorder	47
30      Hosemann Plot for P-55 Assuming a Cauchy Distribution for Crystalline Disorder	48
31      Buchanan and Miller Plot for P-55 Assuming a Gaussian Distribution for Crystalline Disorder	49
32      Buchanan and Miller Plot for P-55 Assuming a Cauchy Distribution for Crystalline Disorder	50
33      P-100 Diffraction Showing the Emergence of the (10,1) Off-Axis Reflection by Fiber Tilting	55

LIST OF ILLUSTRATIONS (Concluded)

FIGURE	PAGE
34      Complete Meridional ( $\text{Chi}=90^\circ$ ) Bragg Scan of P-100	57
35      Complete Off-Axis ( $\text{Chi}=70^\circ$ ) Bragg Scan of P-100	58
36      Bragg Scan of (10,1) Region in Some Pitch-Based Fibers	59
37      Bragg Scan of (11,2) Region in Some Pitch-Based Fibers	60
38      Bragg Scan of (10,1) Region in Some PAN-Based Fibers	61
39      Bragg Scan of (11,2) Region in Some PAN-Based Fibers	62

## LIST OF TABLES

TABLE		PAGE
1	Fiber Mechanical Properties	41
2	Summary of (00,2) WAXD Carbon Fiber Results	42
3	Advanced $L_c$ Analysis Comparison	51
4	Advanced $L_c$ Analysis Results	52
5	Summary of (hk) WAXD Crystal Plane Size ( $L_a$ ) Measurement Techniques (Sizes in Angstroms)	53
6	Summary of (hk) WAXD Crystal Plane Sizes ( $L_a$ in Angstroms)	64
7	Summary of Carbon Fiber 2-D and 3-D Crystal Content	65

## 1. INTRODUCTION

Carbon fibers are extremely important components in high performance composites as they are the primary reinforcing material. Because the mechanical properties of fibers are dependent on their structures, the structure of carbon fibers has been examined by many researchers [1-13]. A continued interest in this area results from the emergence of new carbon fibers with improved properties.

Pitch-based fibers traditionally had high stiffnesses but had weak tensile strengths. PAN-based fibers were strong but lacked high moduli. Recent developments have improved these fibers' properties, and more work is focusing on the compressive properties as well. These property changes result from structural differences created during the fiber manufacture.

Several diffraction techniques have been used to examine the crystalline microstructure of carbon fibers. Wide-angle x-ray diffraction (WAXD), as its name implies, uses the diffraction of x-rays to examine the basic crystalline structure at scattering angles in excess of several degrees (i.e.  $>5^\circ$ ). Structures about the size of crystalline interplanar spacings (1 to 15 $\text{\AA}$ ) are studied. Small-angle x-ray scattering (SAXS), on the other hand, examines the scattering of x-rays at lower angles. In SAXS larger structures, such as crystallites, are examined (sizes up to several 1000 $\text{\AA}$ ). Both x-ray methods examine relatively large volume ( $1 \text{ mm}^3$ ), bulk properties. Smaller sample volumes can be examined using selected area diffraction (SAD) which uses scattering of electrons to examined structures which are comparable in size to those in WAXD but using much smaller sample volumes ( $0.1 \mu\text{m}^3$ ). SAD also has the advantage of being used in conjunction with transmission electron microscopy (TEM) so that images of the diffracting area may be obtained (but of course also has the complex sample preparation difficulties of TEM).

WAXD has been used to examine carbon fibers [1-3,14] in terms of the basic graphitic-like crystals present. This technique is now usually used only to quantify specific properties such as graphite plane orientation and degree of graphitization. In this study some of the newer fibers were examined with WAXD, and some interesting and heretofore unreported properties of the crystalline nature of carbon fibers were discovered.

Most of the publications on x-ray diffraction of carbon fibers are either aimed at experts or only use this technique in a minor role. For this reason significant space in this report is devoted to explaining the terms and notations used in WAXD.

## 2. NOMENCLATURE

### 2.1 HEXAGONAL INDEXING

Carbon fibers have a graphite-like crystal nature. Graphite unit cell is hexagonal corresponding to the hexagonal grid of the basal plane structure. In Figure 1 the hexagonal grid represents the aromatic C-C bonds in the basal plane sheets; a carbon atom is located at each grid vertex.

Conventional Miller's indices for crystals consist of three numbers:  $h$ ,  $k$ , and  $l$  written as  $(hkl)$ . These numbers equal the reciprocal value of where the designated plane cuts the unit cell boundaries along the  $x$ -,  $y$ -, and  $z$ -axes respectively. Thus an index set of  $(210)$  describes a plane which is parallel to the  $z$ -axis and cuts the unit cell at  $a/2$  and  $b/1$  ( $a$ ,  $b$ , and  $c$  are the dimensions of the unit cell along respective axes). Planes that intersect the unit cell on a negative axis have a bar over them (e.g.,  $\bar{1}\bar{1}1$ ). For orthorhombic unit cells,  $a$ ,  $b$ ,  $c$  are different but all at right angles which resemble a rectangular box. Figure 2 shows several examples of planes defined by their Miller's indices.

The literature shows several ways in which the graphitic planes of carbon and graphite fibers are described by Miller indices:

<u>(hk)</u>	<u>(hkl)</u>	<u>(hkil)</u>	<u>(hk,l)</u>
$(10)$	$(100)$	$(10\bar{1}0)$	$(10,0)$
$(11)$	$(110)$	$(11\bar{2}0)$	$(11,0)$
	$(002)$	$(0002)$	$(00,2)$
$(112)$	$(11\bar{2}2)$		$(11,2)$

In hexagonal crystals, such as graphite, the angle between the  $a$ - and  $b$ -axes is  $120^\circ$ . Here, three axes of symmetry of which two are arbitrarily assigned as unit cell axes in the three index

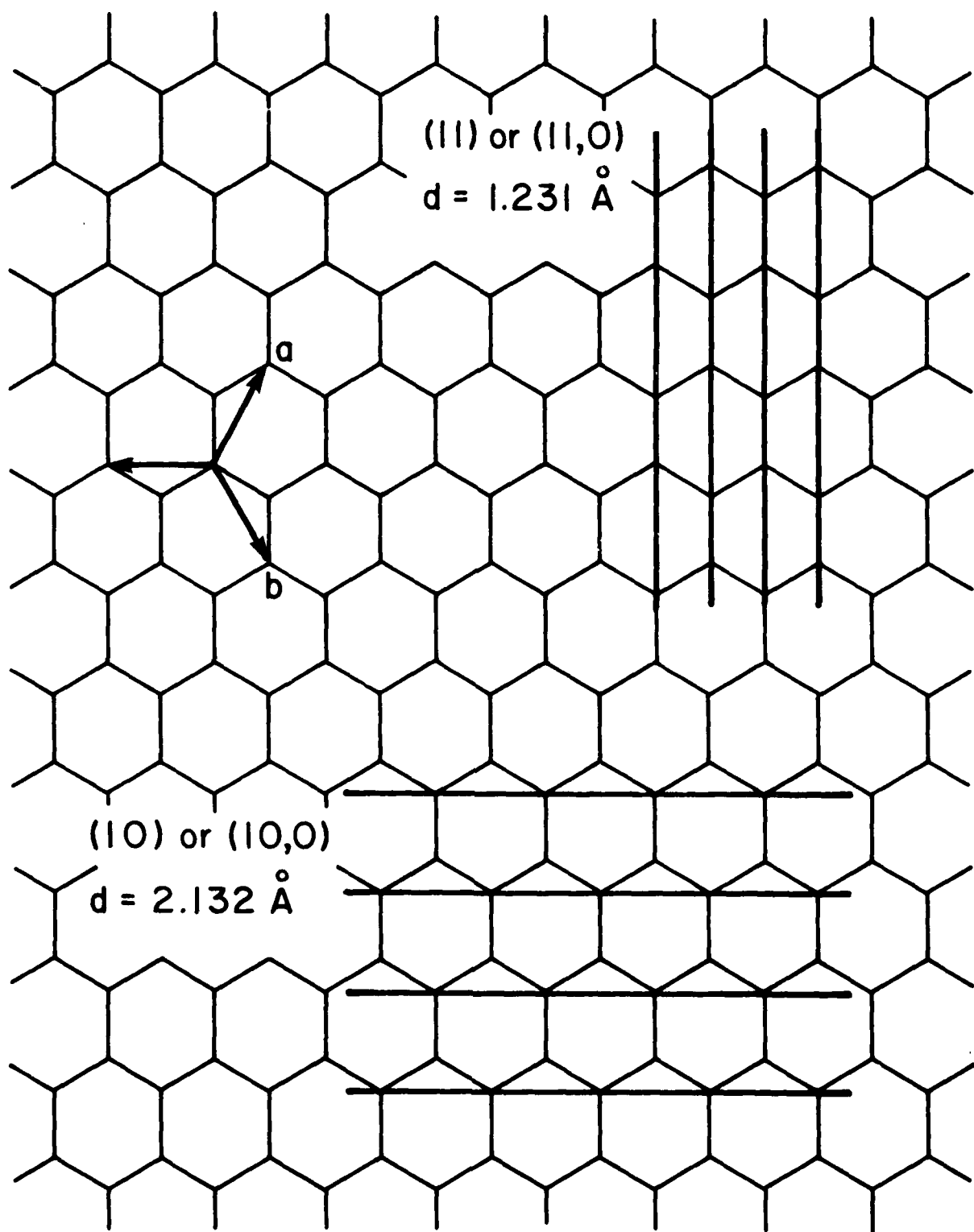
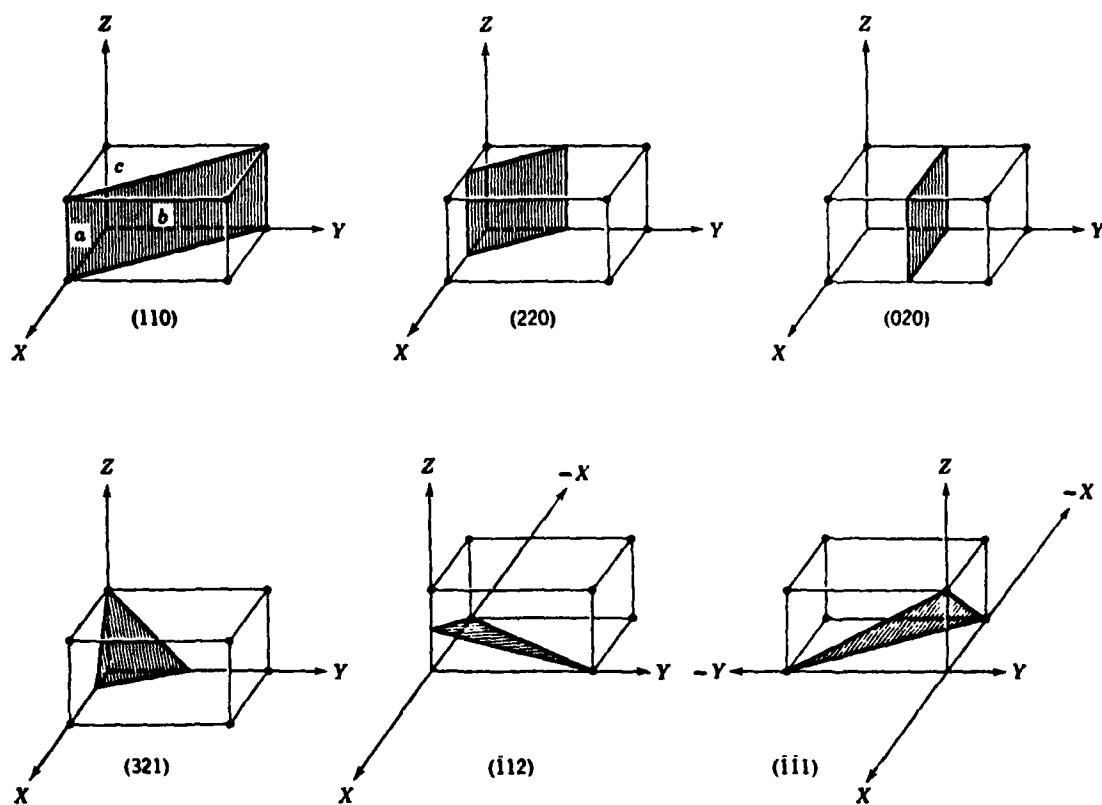


Figure 1. Hexagonal Axes and Crystal Planes in the Graphite Basal Plane.



**Figure 2.** Diagrams of Planes Having Various Miller Indices in an Orthorhombic Unit Cell with Edges  $a$ ,  $b$ , and  $c$  (from Alexander [15]).

systems are given above or all three assigned as in the four index system. Figure 1 shows these unit cell axes as well as the example  $(hk, 0)$  crystal plane projections from the first two rows above (the crystal planes are perpendicular to the diagrammed plane). Recognize that because the  $a$  and  $b$  axes are arbitrarily assigned, there are equivalent planes at  $\pm 120^\circ$  from those diagrammed. The  $c$ -axis is perpendicular to the graphite basal plane so that the  $(00, 2)$  crystal planes coincide with the basal planes.

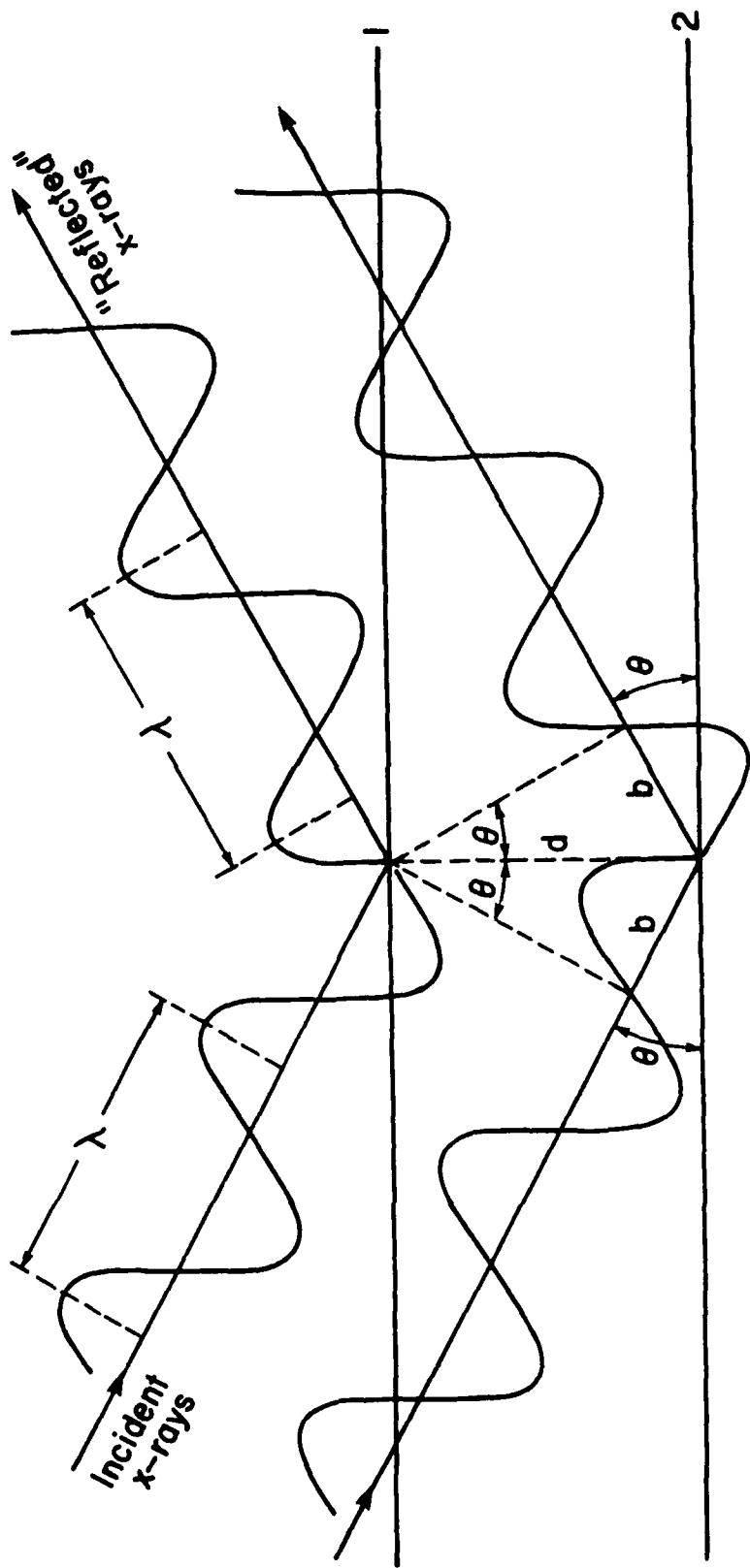
The first column listed actually refers to single graphitic sheets, as these 2-D crystals require only two indices; these are important in carbon fibers as will be explained later. The second and fourth columns are abbreviations of the third column in hexagonal indices. The second column, while used extensively in the literature, does not convey the hexagonal nature of the crystals (versus orthorhombic for example) to the reader as do the last two columns. The third column is the typical hexagonal indices which includes a third in-plane index defined such that the first three indices always sum to zero. Since that third in-plane index is defined by the first two, it is unnecessary; thus the last column line fully defines the crystal planes and conveys their hexagonal nature.

The advantage of column three over four is the ability to spot equivalent planes from the indices. Generally in graphite one refers to only one set of indices when discussing that family of equivalent planes, negating that advantage. As a matter of convenience, the indices as shown in the last column will be used in the report.

## 2.2 DIFFRACTOMETER

For any crystalline plane to appear in WAXD, it must meet the Bragg conditions (see Figure 3). This means that the crystal plane normal must lie in the x-ray collection plane (plane containing the incident beam and diffracted ray detector) and bisects the incident and diffracted rays. To understand this one

## GEOMETRY OF BRAGG'S LAW



CONSTRUCTIVE INTERFERENCE WHEN:

$$n\lambda = 2b = 2d \sin \theta$$

Figure 3. Bragg's Law Diffraction.

must first understand the multiple "geometries" of the data collection system, the sample, the crystals within the sample, and crystal planes within the crystals.

There are two typical types of data collection: flat-film and diffractometer. In the flat-film technique, a fiber bundle is placed directly in front of the collimators (metal tubes with small holes in either end that only allow parallel beams of x-rays to pass), and a flat film pack is placed on the other side perpendicular to the x-ray main-beam and parallel to the fiber bundle (see Figure 4). The sample-to-film distances are typically 29 or 50 mm for WAXD and much longer (e.g. 290 mm) for SAXS. The upper limit of diffraction angle accessible in flat-film photos is about  $50^\circ 2\theta$ . Figure 5 is a typical flat-film photo of a carbon fiber. Appendix A contains flat-film photographs of the commercially available fibers examined.

The diffractometer is much more general in its sample positioning and data collection precision. The main x-ray beam is collimated to hit the center of a 4-circle sample holder; the detector is in the horizontal plane pivoting about the center of the sample holder. Figure 6 shows the rotations available in the sample holder of a 4-circle diffractometer (this diffractometer is basically a computer-controlled 4-axis sample holder) relative to a fiber sample. The sample holder is rotated one half the scattering angle of the detector in the so-called  $\theta$ - $2\theta$  collection geometry; these rotations are the first and second circles. You may wish the sample to be other than this simple arrangement, and the second circle (omega) allows one to deviate from the  $\theta$ - $2\theta$  condition but still keep the rotation about a vertical line. Note that some machines define omega as the total angle the sample plane moves or theta plus omega by the current definition. The azimuthal circle (chi) tilts the sample in the vertical plane defined by the first two circles. The last circle (phi) is a rotation of the sample about its base as defined by the first three circles. (Note that if chi=0°, then phi rotation is the same as an omega rotation.)

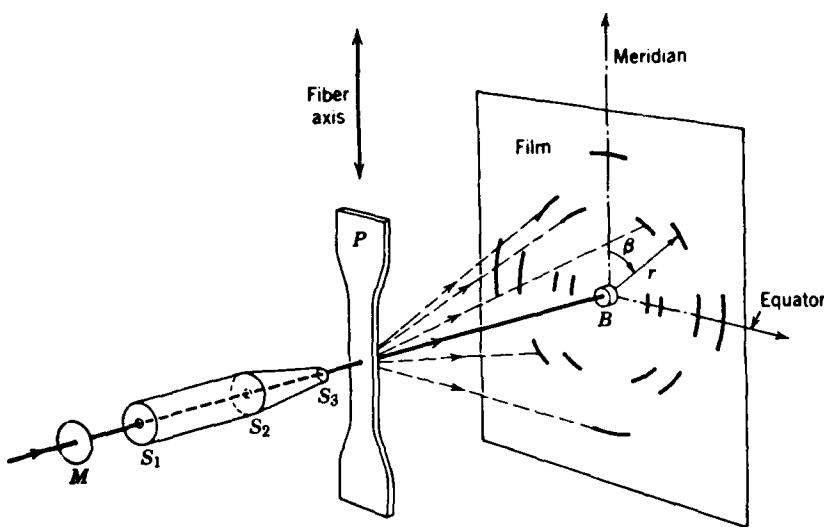


Figure 4. Schematic of X-ray Flat-Film Camera ( $S_1$ ,  $S_2$ , and  $S_3$  are the camera's collimator) (from Alexander [15]).

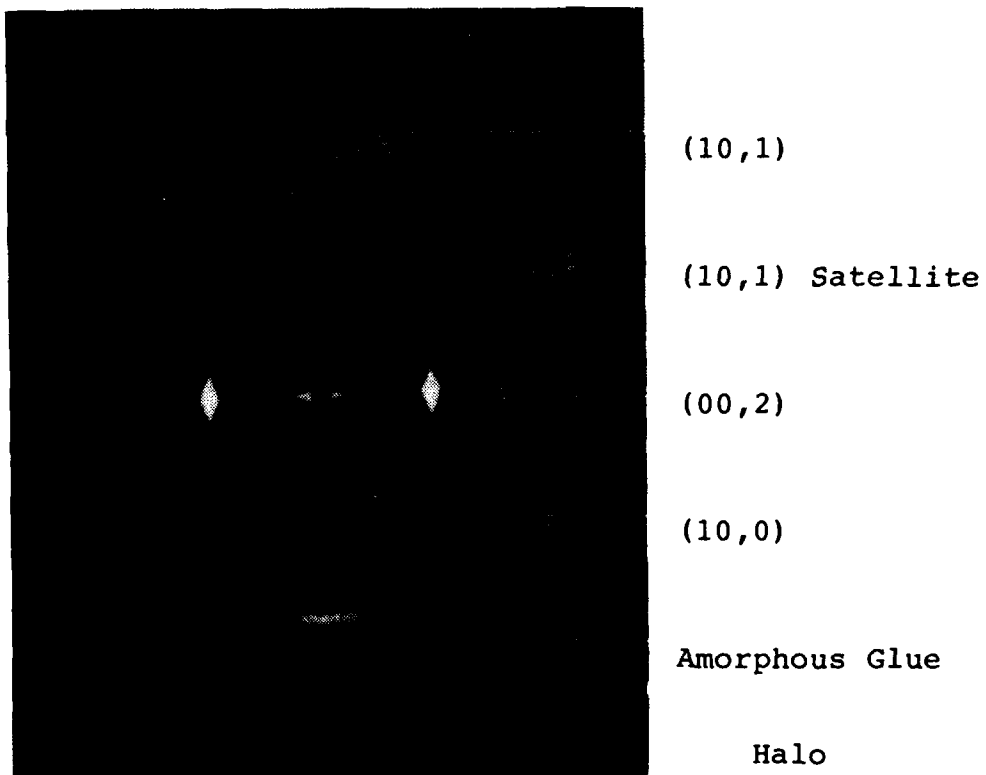


Figure 5. Flat-Film WAXD Photograph of P-100 Carbon Fiber.

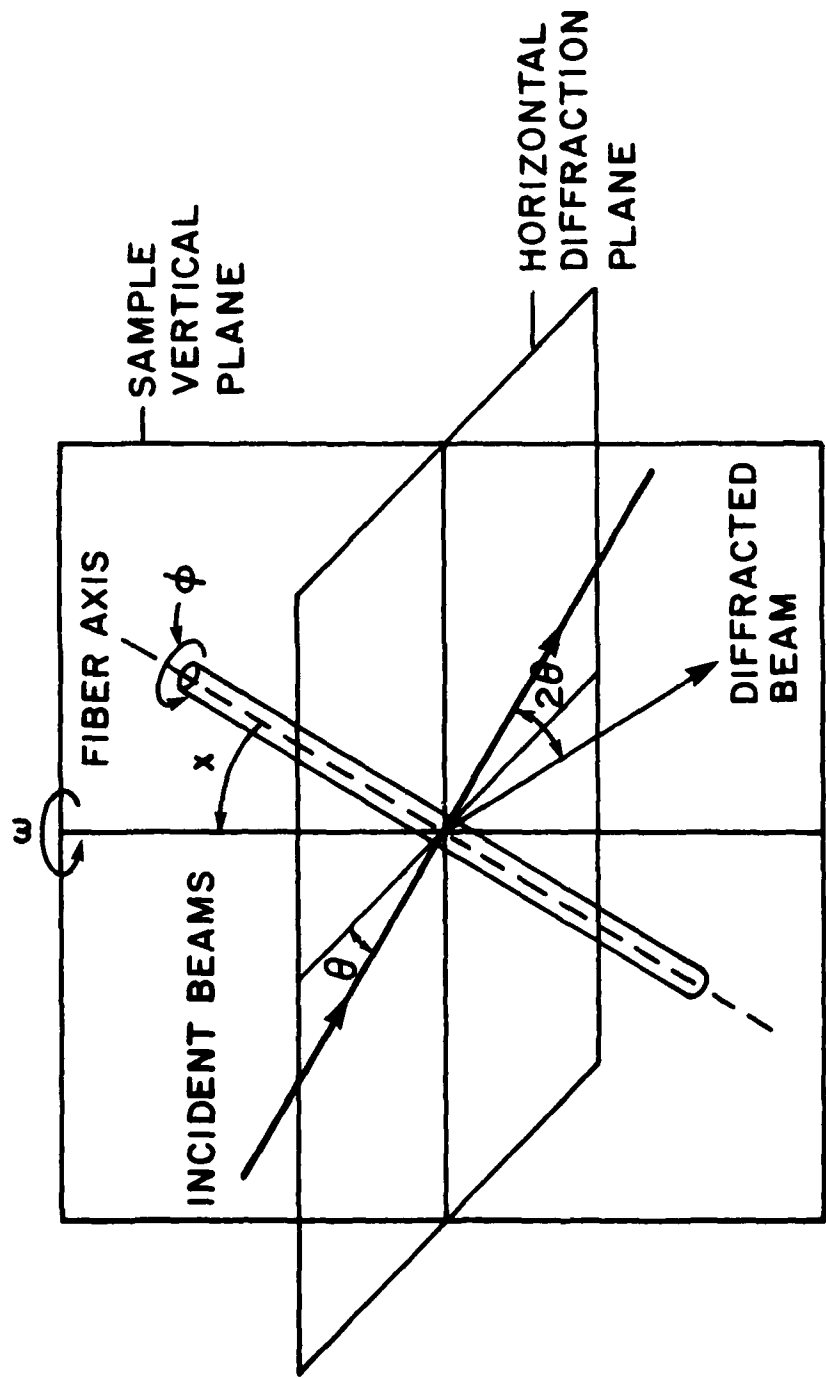


Figure 6. Four-Circle Diffractometer Geometry with a Fiber Sample.

Single crystal diffraction yields spots for each crystal plane which meets the Bragg condition. To measure the intensity of these spots, the  $2\theta$  detector scans must be made at sample orientations of all phi, chi, and omega. The other extreme is powder samples (or bulk crystallized polymers) which have within their sample volume crystals already oriented in all directions. Powder samples produce rings instead of spots, and therefore simple Bragg scans are adequate.

Common diffraction scans for powders and polymers include Bragg and azimuthal (or chi) scans. A Bragg scan is when a sample's scattering intensity is measured by stepping the detector through  $2\theta$  (usually in steps of  $0.1^\circ$ ) while the sample plane is moved one-half that angle ( $\theta-2\theta$  collection geometry). The azimuthal scan is when the scattering intensity is measured by rotating the sample through the chi circle (or fraction of the chi circle since each quadrant is equivalent) with the detector at a fixed Bragg angle. In both scans phi and omega may be fixed at any desired position.

### 2.3 FIBER DIFFRACTION

Fibers in general and carbon fibers specifically are axially symmetric; that is, a rotation about the fiber axis (phi) does not change its diffraction pattern. Any axial nonsymmetry in individual fibers can be averaged out by using a randomly assembled fiber bundle so that the fiber bundle pattern is axially symmetric.

The easiest way of understanding the terminology of fiber diffraction is to imagine the fiber stretched from pole to pole of a hollow globe. "Equatorial" reflections result from crystal planes parallel to the fiber axis such that their normals all fall in the sample equatorial plane, and diffraction appears at the globe's equator with both the main and diffracted beams in the equatorial plane ( $\chi=0^\circ$ , see Figure 7). In flat-film photos the equatorial reflections appear along the horizontal axis when the fibers were held vertically (see Figure 4).

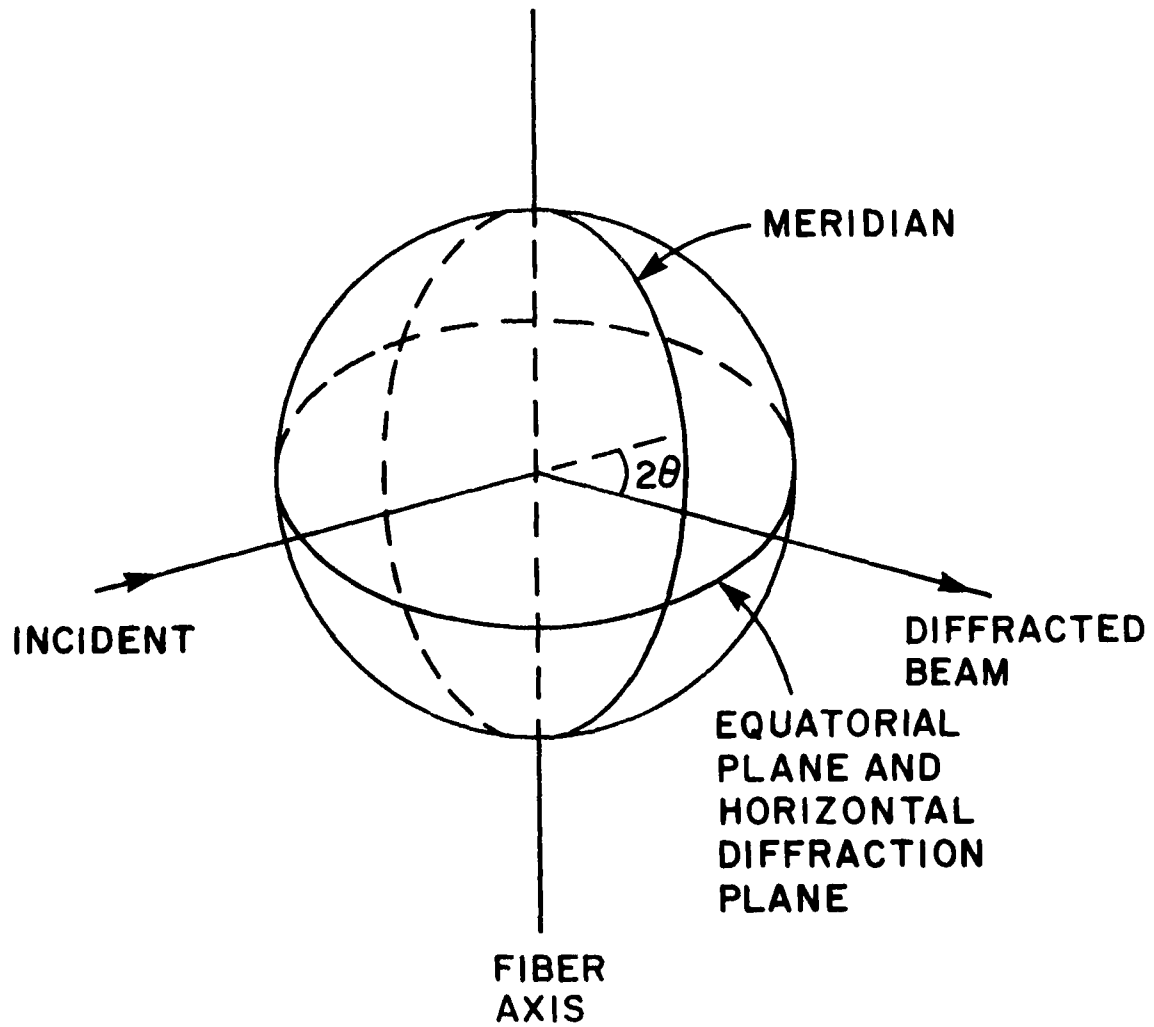


Figure 7. Equatorial Diffraction Geometry.

"Meridional" reflections are from crystal planes in the fiber that are perpendicular to the fiber axis such that their normals are parallel to the fiber axis or pointed to the globe's poles. These diffraction spots appear on any of the globe's meridians as the main and diffracted beams occur at the same latitude on opposite sides of the globe. The fiber must be at  $\chi=90^\circ$  to fulfill that condition (see Figure 8). In a flat-film photo meridional reflections should not be visible, although they sometimes are due to misalignment of the crystals in the fiber which will be discussed below.

"Off-axis" reflections arise from crystal planes tilted at some angle other than  $90^\circ$  and  $0^\circ$  to the fiber axis. The plane normals will sweep out a cone at both ends of the globe (see Figure 9) requiring the fiber to be tilted. In fact the angle the crystal planes make with the fiber axis (one-half the cone angle) is the amount of tilt the fiber must make from the meridional conditions to show off-axis reflections. Figure 10 shows the fiber being tilted by an omega rotation, and Figure 11 shows a chi rotation ( $90^\circ$  minus one-half the cone angle).

The need to tilt the fibers to observe off-axis diffraction was recognized for Pitch-based carbon fibers in early electron diffraction SAD studies [16]. The SAD technique looks at a small section of the fiber and is very sensitive to local variations in the crystal alignment. PAN-based fibers of that day showed no off-axis reflections in either SAD or WAXD. The same rules apply to WAXD except the average misalignment in a fiber bundle is generally large enough to generate the required tilt for some of the crystals even if the bundle isn't tilted.

Off-axis reflections show up on flat-film photos only when  $\theta$  equals one-half the cone angle (and when misalignment allows the crystal to fulfill the Bragg condition). The graphite sheets in carbon fibers only lie approximately parallel to the fiber axis (see section 3.1) with varying degrees of misalignment (or tilting) of those planes away from the fiber axis. In carbon fibers the (10,1) reflection occurs at  $2\theta=44.6^\circ$ , and this plane is

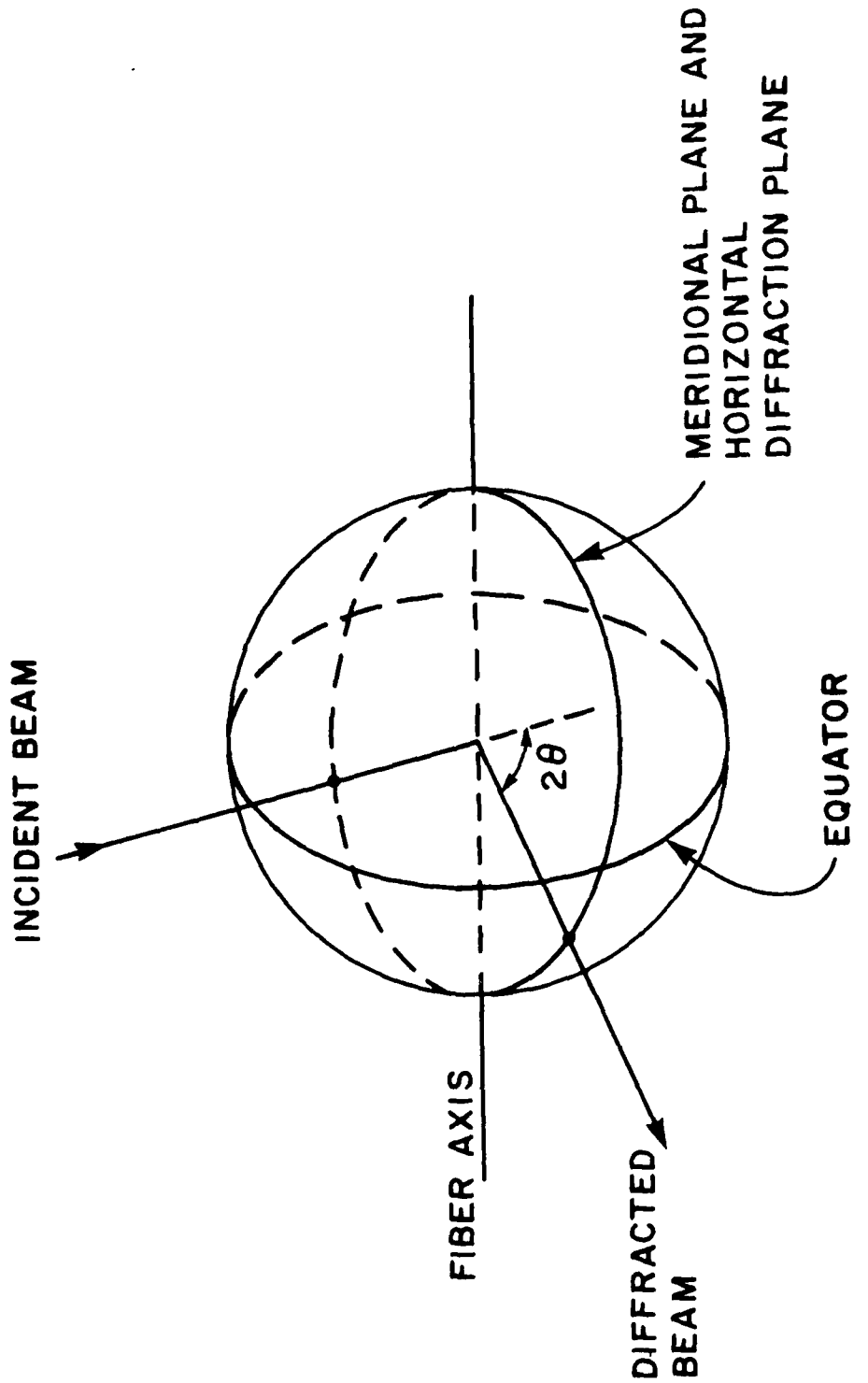


Figure 8. Meridional Diffraction Geometry.

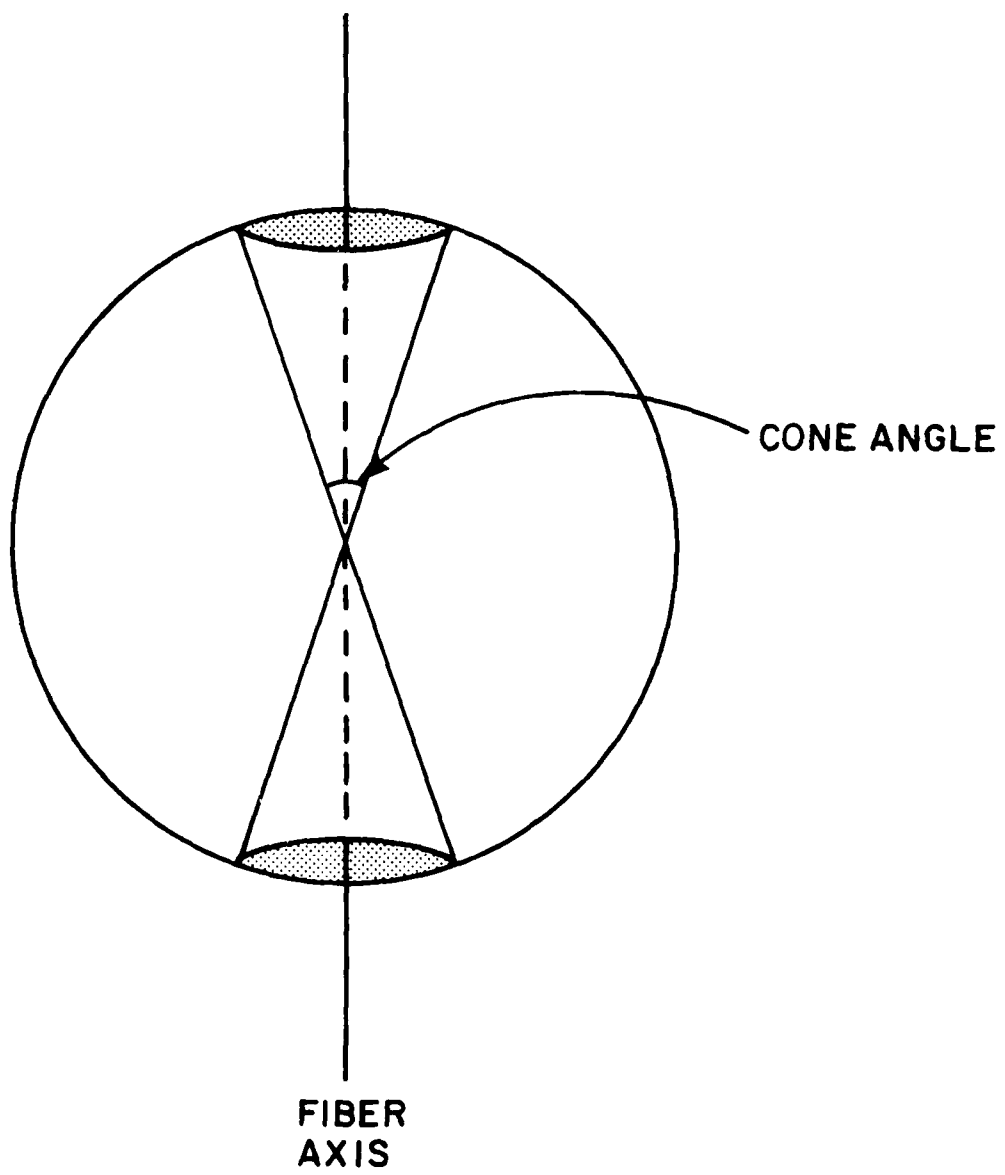


Figure 9. Cone Defined by Fiber Off-Axis Plane Normals.

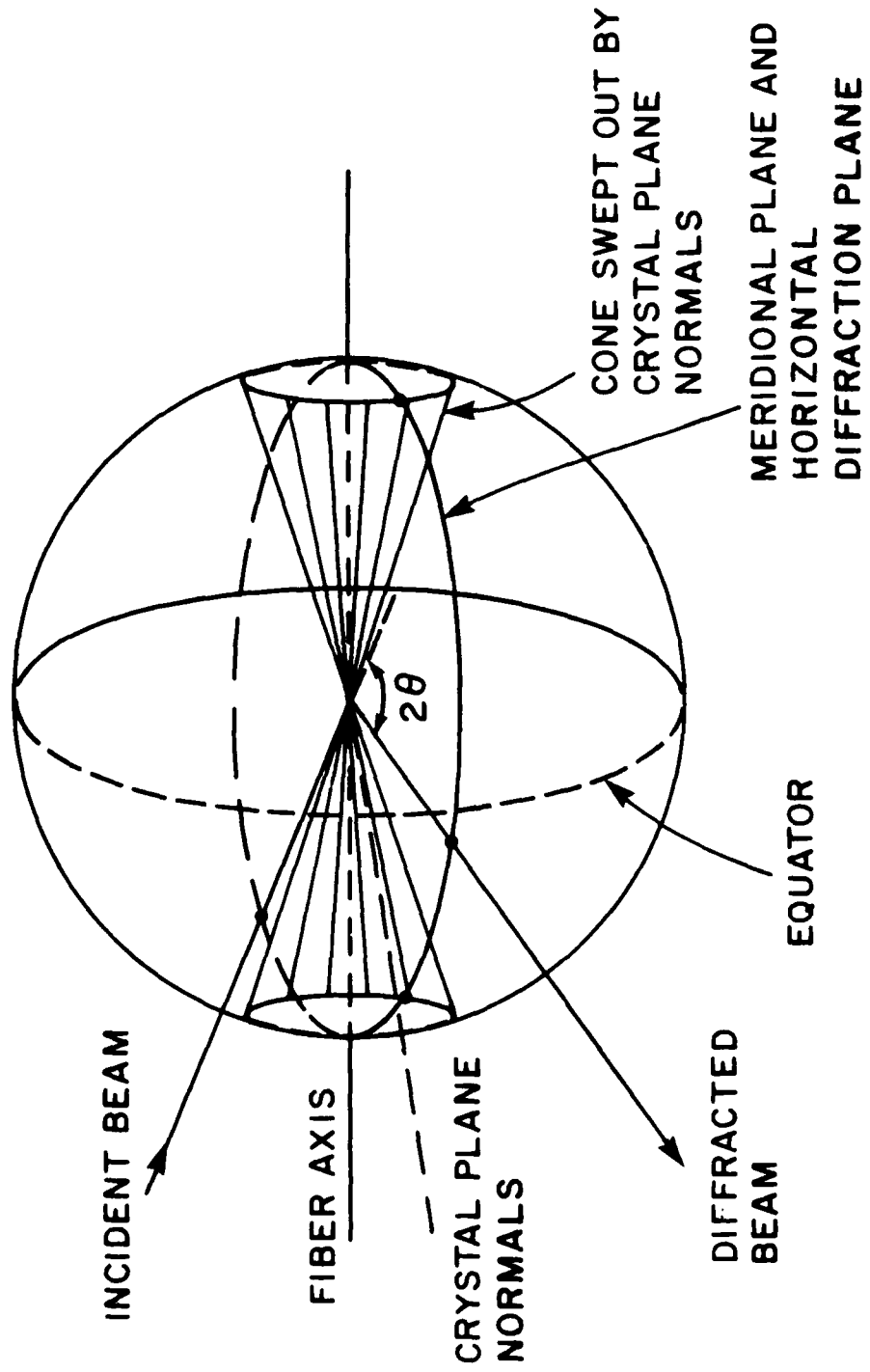


Figure 10. Off-Axis Diffraction Geometry - Omega Circle Adjustments.

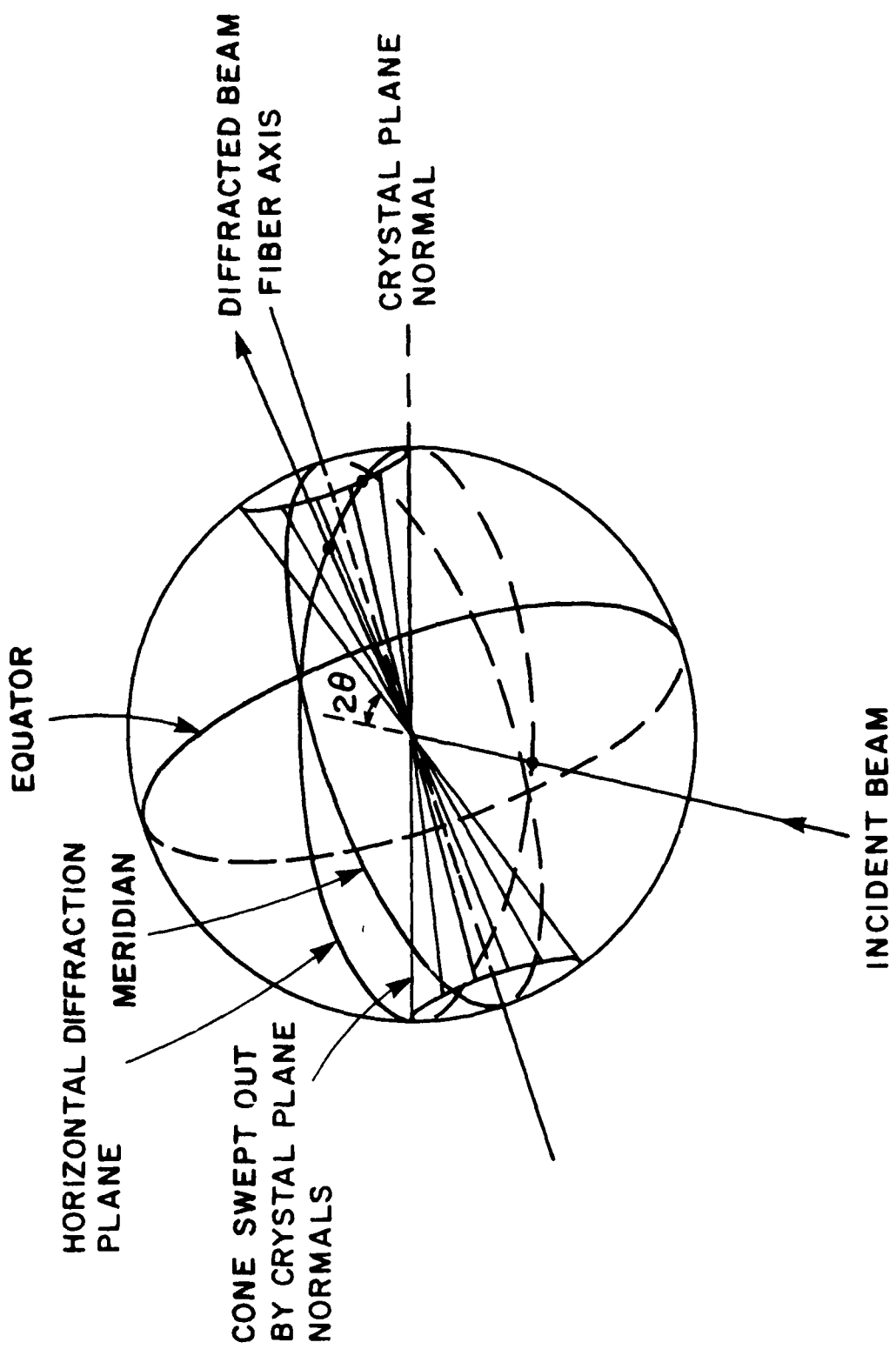


Figure 11. Off-Axis Diffraction Geometry - Chi Circle Adjustments.

tilted 17.6° from the fiber axis; since the difference between 22.3° and 17.6° is less than the typical basal plane misalignment, the (10,1) reflection should be visible in flat-film photos and can be seen in high modulus fibers such as P-100 (see Appendix A).

Meridional reflections can be seen as special cases of the general off-axis case; crystal plane tilt is 0°, therefore the cone angle is zero and diffraction occurs at  $\chi=90^\circ$  and  $\omega=0^\circ$ . Likewise in the equatorial reflections, the crystal tilt is 90° from the fiber axis in which case the cone has opened up to 180° or simply the equatorial plane.

### 3. CARBON/GRAphite REFLECTIONS

#### 3.1 GRAPHITE CRYSTALS

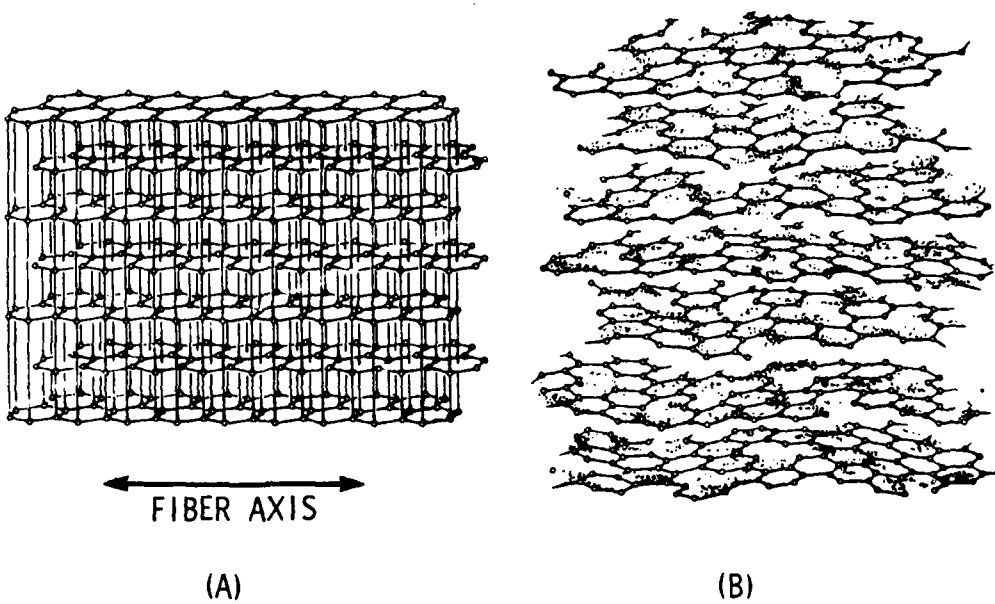
In carbon fibers the orientations of the crystalline graphite planes are approximately parallel to the fiber bundle but randomly placed within the fiber cross section with the a- and b-axes of the graphite planes randomly oriented. Thus the (00,1) reflections are equatorial while (hk,0) are usually associated with the meridional region.

The graphite sheets in carbon fibers are by themselves two-dimensional crystals (i.e. the atoms that make up the sheets are in precise locations relative to the other atoms). If these two-dimensional crystalline graphitic sheets are randomly placed with respect to the next sheet, this is the so-called "turbostratic" structure. In highly graphitized fibers, 3-D crystals are formed when the atoms of one sheet are placed in a specific position relative to the atoms in the next sheet (i.e., in precise crystallographic registry). Figure 12 shows a comparison of the above two cases.

A review by Ruland [17] gives the "best" values for the graphite crystal dimensions as  $a = b = 2.4614\text{\AA}$ ,  $c = 6.707\text{\AA}$ . These values are slightly different from the JCPDS [18] values for basal crystalline graphite but not significantly so for most carbon fiber work ( $a = b = 2.463\text{\AA}$ ,  $c = 6.714\text{\AA}$ ). Ruland [17] also lists an interplane spacing for turbostratic carbon of  $3.440\text{\AA}$  (interplane spacing in crystalline graphite =  $3.3535\text{\AA}$ ).

Because the a- and b-axes are randomly oriented with respect to the fiber axis, the (hk,0) plane normals sweep out a complete circle in the sample planes parallel to the fiber; and because the fibers are axially symmetric, the normals of all the (hk,0) planes sweep out a complete sphere. Such planes should have a ring-like diffraction pattern similar to that for a powder but, in fact, behave like meridional reflections.

The graphite planes in fibers, however, are not large flat sheets. Several models of carbon fiber microstructure are shown



SCHEMATIC DIAGRAMS OF (A) A THREE-DIMENSIONAL GRAPHITE AND (B) A TURBOSTRATIC STRUCTURE

Figure 12. Comparison of Turbostratic and 3-D Graphite Crystals in Carbon Fibers.

here. These include the entwined fibrils observed by Diefendorf and Tokarsky [8] (Figure 13), the wavy fibrils of Perret et al. [1-3] (Figure 14), the thumb-print cross section of Bacon [5] (Figure 15), and the holey curved bundles of graphite sheets of Barnet and Noor [6,7] (Figure 16) and Bennett and Johnson [9,10] (Figure 17). In the fiber axis direction, the ordering of atoms in the  $(hk,0)$  planes is sufficient to generate diffraction. That is to say that along the fiber, the number of crystal planes is sufficiently large enough to produce constructive interference in a Bragg scan. The size of this stack of planes is called the persistence length.

The average random orientation of the  $a$ - and  $b$ -axes in the graphite sheets or bundles is such that all  $(hk,0)$  planes that can produce diffraction do so in the meridional region. Sheets or bundles that produce the  $(10)$  or  $(10,0)$  reflection will not show the  $(11)$  or  $(11,0)$  reflection, but other sheets or bundles will. Also a distribution of orientations within those bundles will generate diffraction; as one rotates from vertical to horizontal, the persistence length along the effective flat area drops dramatically. Thus the effective size of the  $(hk)$  crystals and number capable of diffracting decrease. From the globe analogy (section 2.2) instead of the probabilities all concentrated at the poles coincident with the fiber bundle, a distribution of probabilities exist, centered about poles, finite but rapidly decreasing as one gets further away from the poles. This analogy is also complicated by the change in the crystals sizes and orientations.

The off-axis  $(hk,1)$  plane normals in graphite will sweep out the cone described in section 2.2 above at each pole. If the graphite planes were large and flat, they would sweep out an entire sphere minus the cone at the poles. As described in the paragraph above, the  $(hk,1)$  reflections also have probabilities of diffracting at more than the ring on the globe defined by the cone. Note however that the cone defines the upper limit for the probabilities with zero probability at latitudes greater and a decreasing probability at lower latitudes.

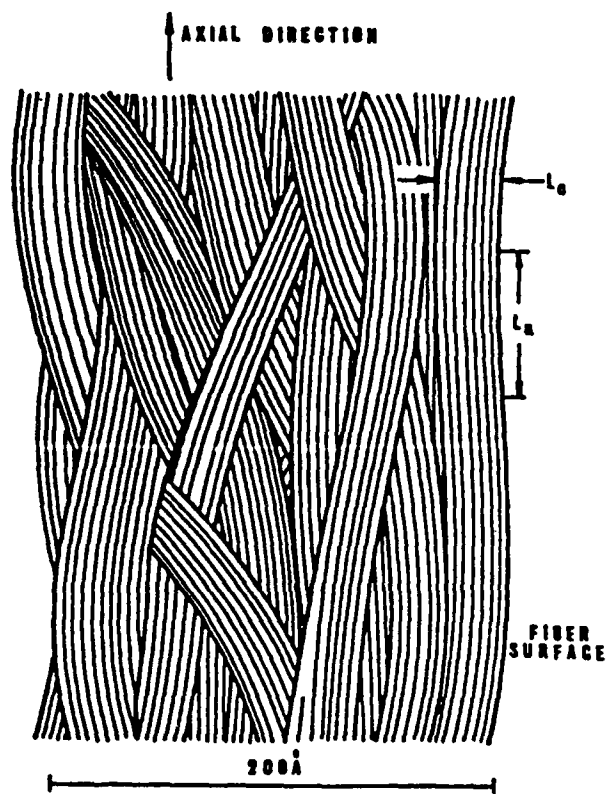
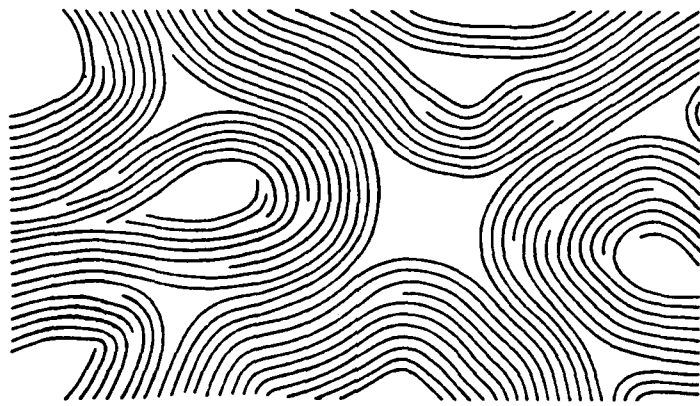


Figure 13. The Entwined Fibrils Model of Carbon Fiber Morphology of Diefendorf and Tokarsky [8].



Figure 14. The Wavy Fibrils Model of Carbon Fiber Morphology of Perret et al. [1-3].



FIBER CROSS SECTION

Figure 15. The Thumb-Print Cross-Section Model of Carbon Fiber Morphology of Bacon [5].

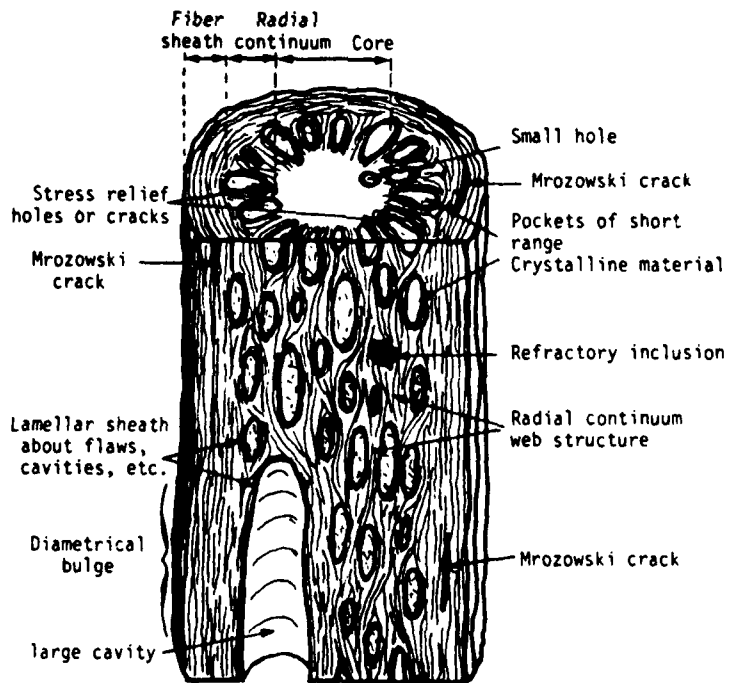


Figure 16. The Holey Curved Bundles of Graphite Sheets Model of Carbon Fiber Morphology of Barnet and Noor [6,7].

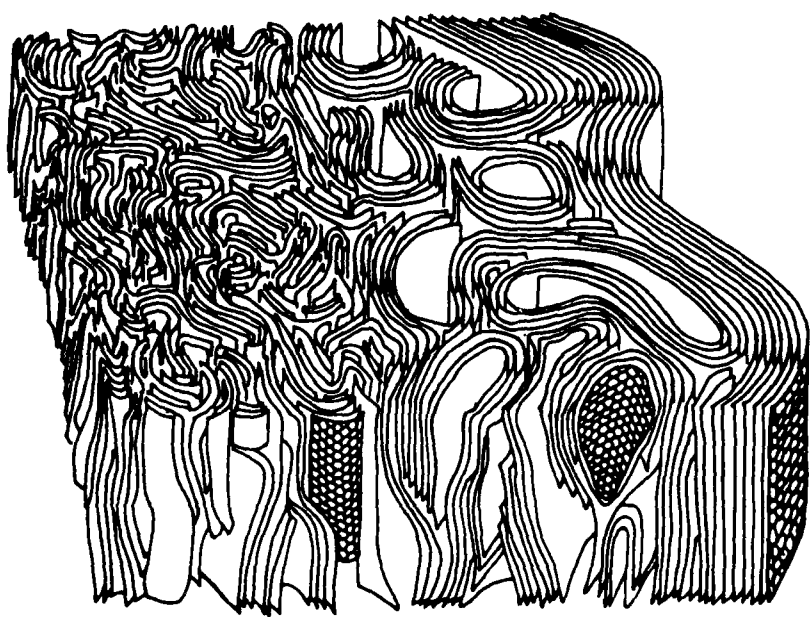


Figure 17. The Holey Curved Bundles of Graphite Sheets Model of Carbon Fiber Morphology of Bennett and Johnson [9,10].

### 3.2 TWO-DIMENSIONAL LATTICES

The dimensionality of the graphitic crystals in carbon fiber is a source of some controversy - the turbostratic carbon structure being 2-D and crystalline graphite being 3-D. Carbon fibers of low modulus <25 Msi being predominantly turbostratic and gradually increasing to more crystalline graphitic nature as one goes to higher modulus fibers. The observation of off-axis reflections is considered necessary proof of 3-D crystals; and generally only high modulus Pitch based carbon fibers exhibit these off-axis reflections.

The diffraction from a three-dimensional crystal lattice is very nearly symmetric. That is, the maximum peak intensity is very close to the position with equal intensity on both sides (the peak centroid). This is true whether the intensity is plotted versus  $2\theta$  or versus s-space. S-space is the inverse of the interplane spacing ( $d$ ) and is commonly used to express the scattering position independent of the wavelength (it is also the magnitude of the reciprocal space vector). A peak's position is determined by the interplane spacing of the crystal plane diffracting according to Bragg's Law.

$$d = n\lambda/2 \sin\theta \quad \text{Bragg's Law} \quad (1)$$

$$s = 2 \sin\theta/\lambda \quad \text{s-space} \quad (2)$$

Two-dimensional lattices do not produce symmetrical peaks. This is of particular interest in carbon fibers since many of the fibers are turbostratic composed of graphitic sheets randomly arrayed in stacks. Each of those sheets constitutes a 2-D lattice.

Several workers [14,19-22] have calculated the line profiles from randomly oriented 2-D reflections. Warren and Bodenstein [14] estimated the shape of 2-D reflections of finite size in the commonly-used crystal size equation:

$$L_{(hk)} = \frac{1.77 \lambda}{B(1/2, 2\theta) \cos\theta} \quad \text{Warren and Bodenstein} \quad (3)$$

where  $L$  is the crystal size and  $B(1/2, 2\theta)$  is the full width in  $2\theta$  at 1/2 the peak maximum.

Ruland [22] calculated the exact solution for randomly oriented crystals of finite size (see Equations 4 and 5):

$$I(s) = \frac{1}{4s} \left(\frac{L}{\pi s}\right)^{1/2} F \left[ \frac{\pi L}{2s} \left(s^2 - s_k^2 - \frac{1}{2L^2}\right) \right] \quad (4)$$

$$F(z) = \left( \frac{(z^2 + 1)^{1/2} + z}{z^2 + 1} \right)^{1/2} \quad (5)$$

Figure 18 shows several of Ruland's theoretical intensity profiles. Ruland and Tompa [23] calculated the profiles for highly ordered infinite 2-D reflections which showed an intensity distribution similar to that shown in Figure 19 with an intensity profile similar to that of the randomly ordered 2-D crystals.

The exact profiles of oriented finite sized such as the  $(hk)$  reflections in carbon fibers has not been published. One can assume that the size and profiles of randomly oriented finite sized 2-D crystals of equations 3-5 will apply with an intensity probability distribution as given in Figure 19.

### 3.3 CRYSTALLITE SIZES

In the previous section the effects on WAXD profiles from finite sized crystals were introduced. Derived for 2-D crystals, equation 3 is most commonly used in the literature with (10) and (11) profiles to obtain the persistence lengths ( $L_a$ ) of the graphite sheets parallel to the fiber as shown in Figures 13 and 14. A similar equation was derived by Ruland [22,17]:

$$L_{(hk)} = \frac{1.84 \lambda}{B(1/2, 2\theta) \cos\theta} \quad (6)$$

The constant in equation 3 differs from equation 6 due to the assumptions of Gaussian versus Cauchy distribution of sizes:

## 2-D THEORETICAL PROFILES

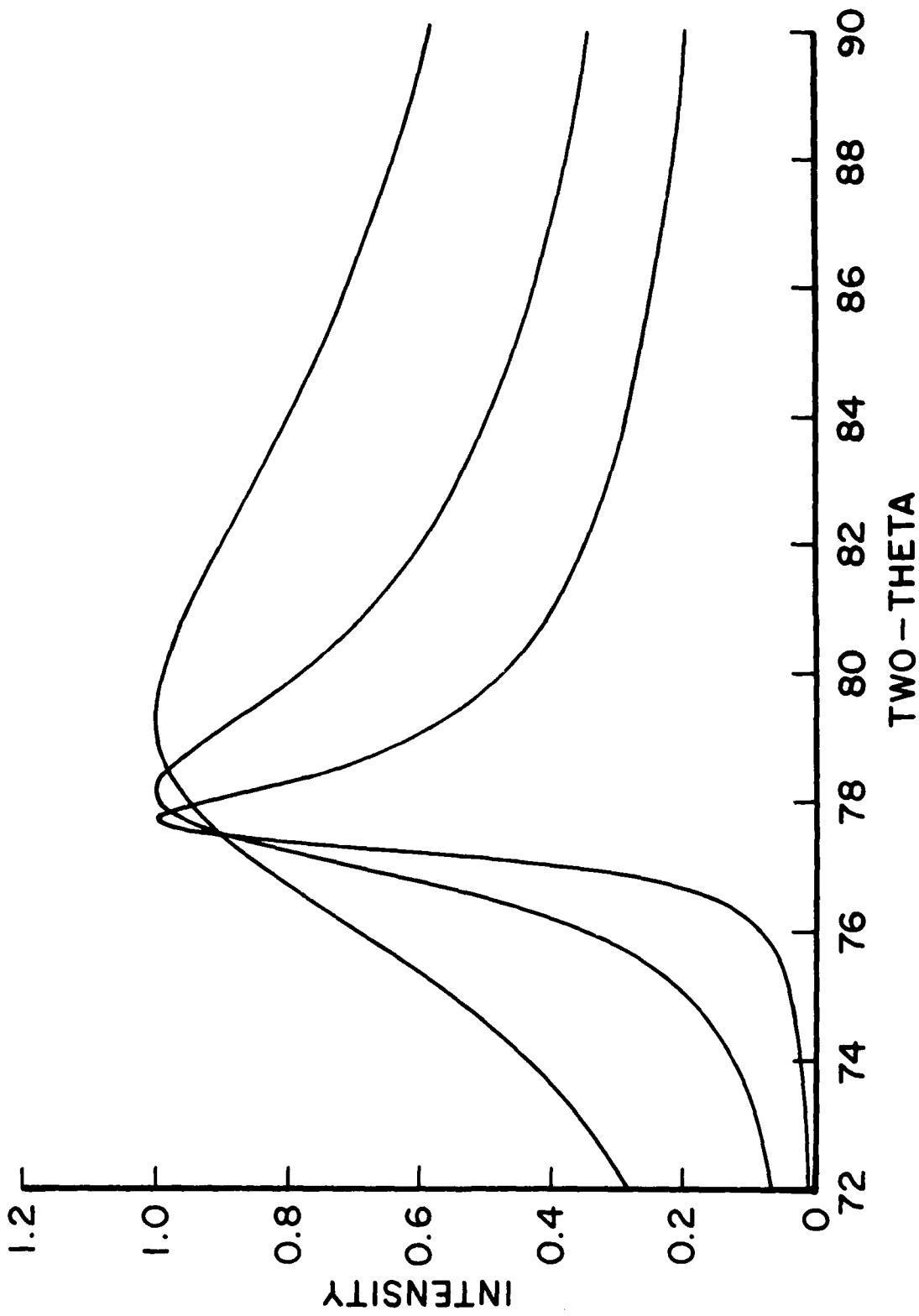


Figure 18. Theoretical Intensity Profiles of the 2-D Graphite (111) Peak from Randomly Oriented Crystals of Several Sizes.

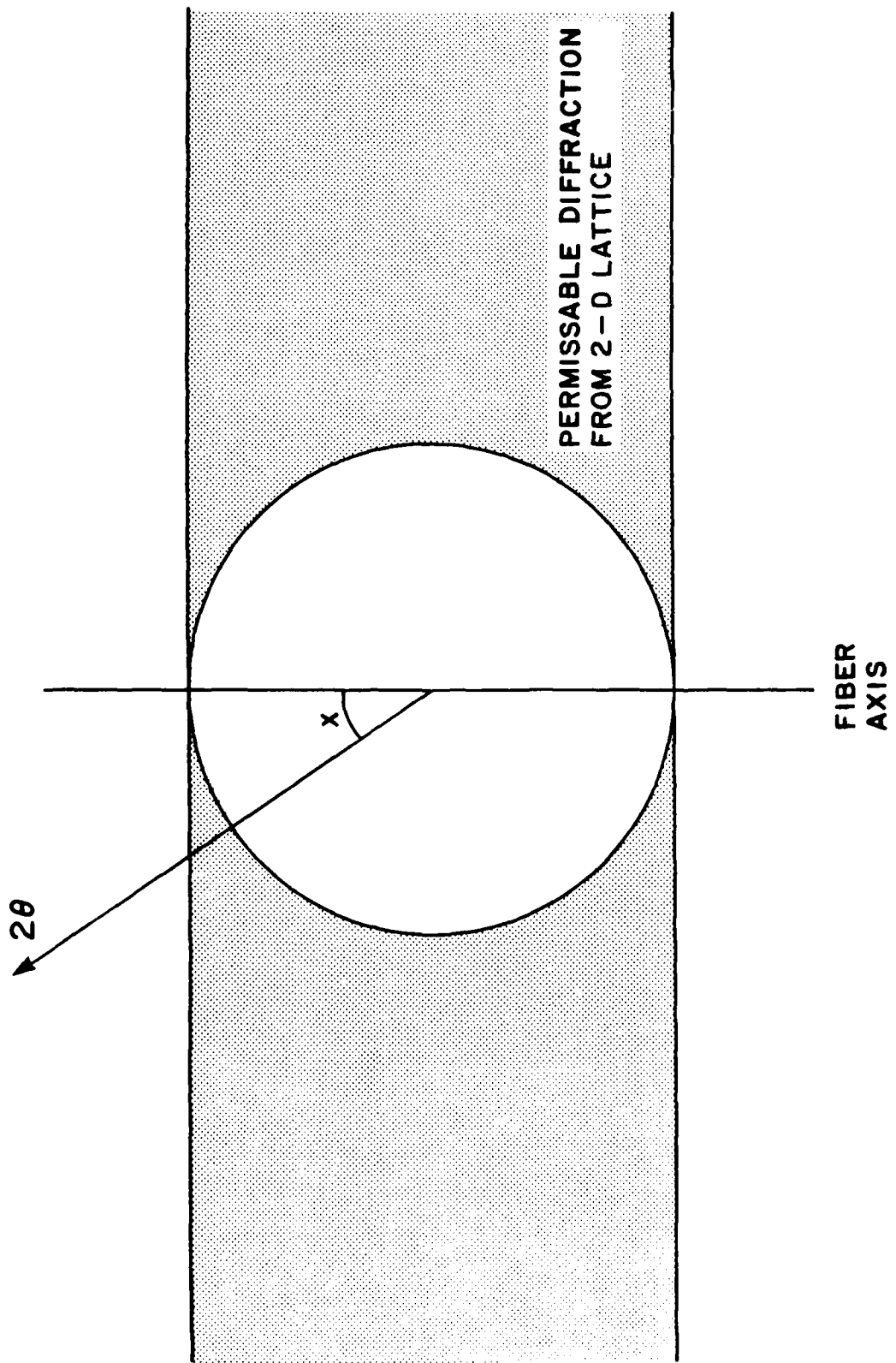


Figure 19. Intensity Distribution from 2-D Crystal Sheets Oriented Parallel to the Fiber Axis.

the latter allowing an exact solution. A Gaussian distribution defines the well known "normal" bell-shaped curve. The Cauchy (or modified Lorentzian) distribution is commonly used in defining x-ray peaks and is characterized by a slightly different curve which has greater area in the tail regions and less area in the center (see Figure 20).

Similarly the shift to higher angle in the peak maximum from 2-D crystals is related to this size:

$$L_{(hk)} = \frac{k'}{s_{\max} - s_h} \quad (7)$$

The constant  $k'$  has values of 0.28 to 0.39 depending on the distribution of sizes used in the derivation (0.32 in Ruland's analysis).

Neither method is applicable if 3-D crystals are present, since the measured profiles result from overlapping 2-D and 3-D reflections or only 3-D (not likely in fibers but would use Scherrer equation below). Neither method distinguished among size, disorder, and strain broadening effects, but since the atoms in the sheets are covalently bonded, size should dominate (this has been disputed in pyrolyzed carbons [24]). Also the methods that can separate these factors require higher order reflections which are not present in most carbon fibers.

The graphite bundle thickness ( $L_c$ ) shown in Figures 13 and 14 is most commonly measured by WAXD [17] using the (00,2) reflection profile in the Scherrer equation [25]:

$$L = \frac{K \lambda}{\beta \cos \theta} \quad \text{Scherrer} \quad (8)$$

where  $K$  is a shape parameter usually taken as unity and  $\beta$  is the integral breadth in  $2\theta$ .

More advanced methods also using the (00,4) and (00,6) reflections are not commonly used because of the complexity of the calculations. They can be used to separate the size information from strain and disorder. The details are explained

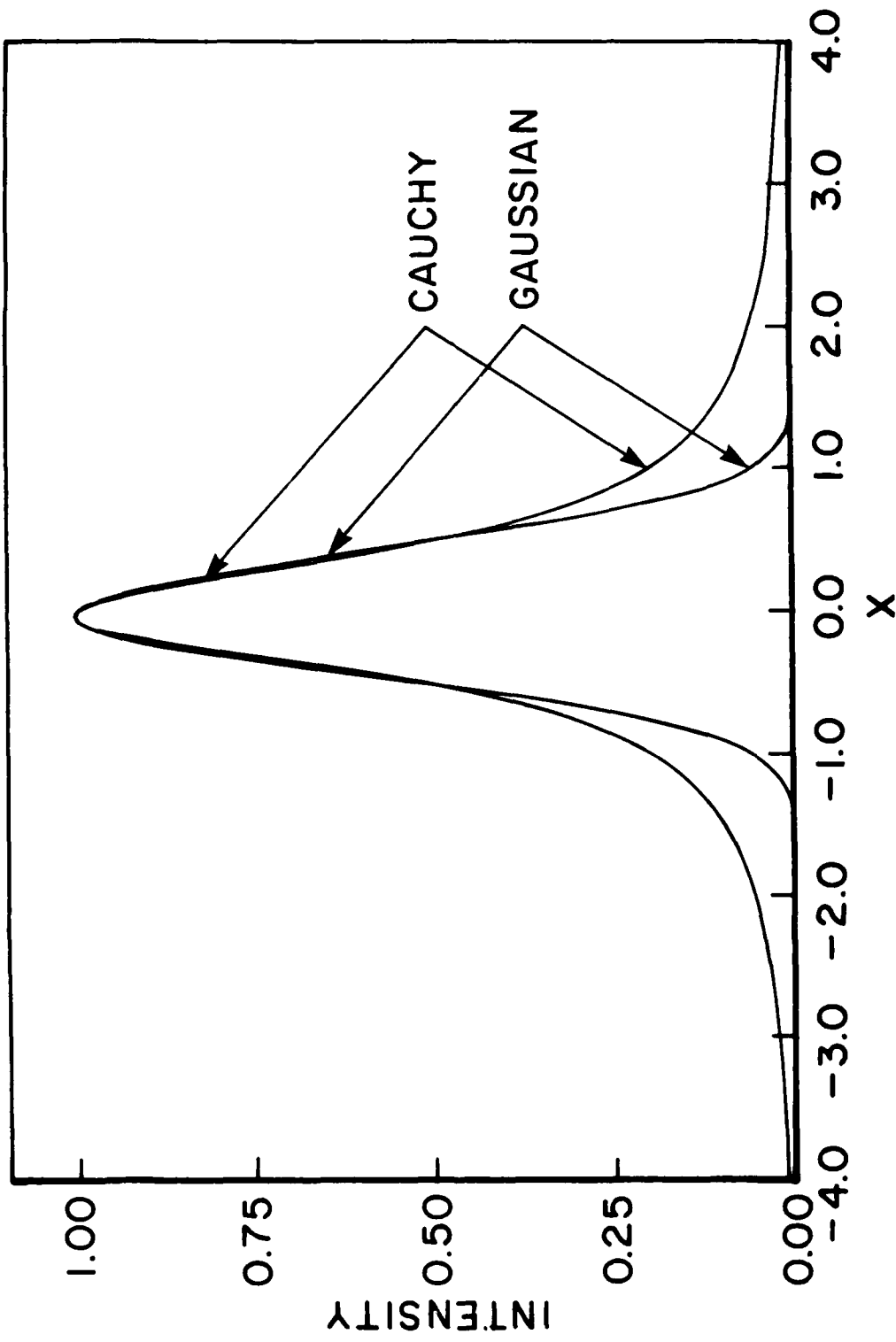


Figure 20. Comparison between Gaussian and Cauchy Distributions.

elsewhere [15], but simply stated the breadth of a series of reflections such as (00,2), (00,4), and (00,6) increases at the higher order because of the crystalline disorder and strain.

Hosemann [26] plots the square of the sample integral breadth ( $\beta^2$  or  $(\delta s)^2$ ) versus  $m^4$  (where  $m$  is 1, 2, and 3 respectively with  $d = d_{00,2}$ ); while Buchanan and Miller [27] (assuming Gaussian profiles) plot  $(\delta s)^2$  versus  $s^2$ . The intercept in both cases is the square of the reciprocal crystal size:

$$(\delta s)_o^2 = (1/L^2) + [(\pi g_{II})^4 m^4/d^2] \quad \text{Hosemann} \quad (9)$$

$$(\delta s)_o^2 = (1/L^2) + 4 e^2 s^2 \quad \text{Buchanan and Miller} \quad (10)$$

The intercept in either plot is inversely related to the crystal size,  $L$ . The slope of these plots are related to the crystal disorder; both  $g_{II}$  and  $e$  above are described as average relative deviations of the lattice spacing ( $\Delta d/d$ ). Similar equations can be derived for Cauchy distributions and look the same as above with each term the square root of the terms in the equations above.

A major complication of the size analysis for both (hk) and (00,1) reflections is the measured broadening resulting from both the sample and instrumental sources. A profile of instrumental broadening can be measured using large near-perfect crystals such as beryllium acetate. Figure 21 shows the diffraction of beryllium acetate at  $61.8^\circ 2\theta$  with an angular spread of  $0.25^\circ$  fit to a Gaussian curve. Separation of the breadths resulting from the convoluted profiles (convolution means two profiles are folded into each other) uses one of the these two equations (the instrumental profile is nearly Gaussian favoring equation 11):

$$(\delta s)_m^2 = (\delta s)_i^2 + (\delta s)_o^2 \quad \text{Gaussian} \quad (11)$$

$$\delta s_m = \delta s_i + \delta s_o \quad \text{Cauchy} \quad (12)$$

THU. 17 NOV 1988 16:34:18

HMTA 0.54mm 2 June 88

GRAPH NUMBER 3

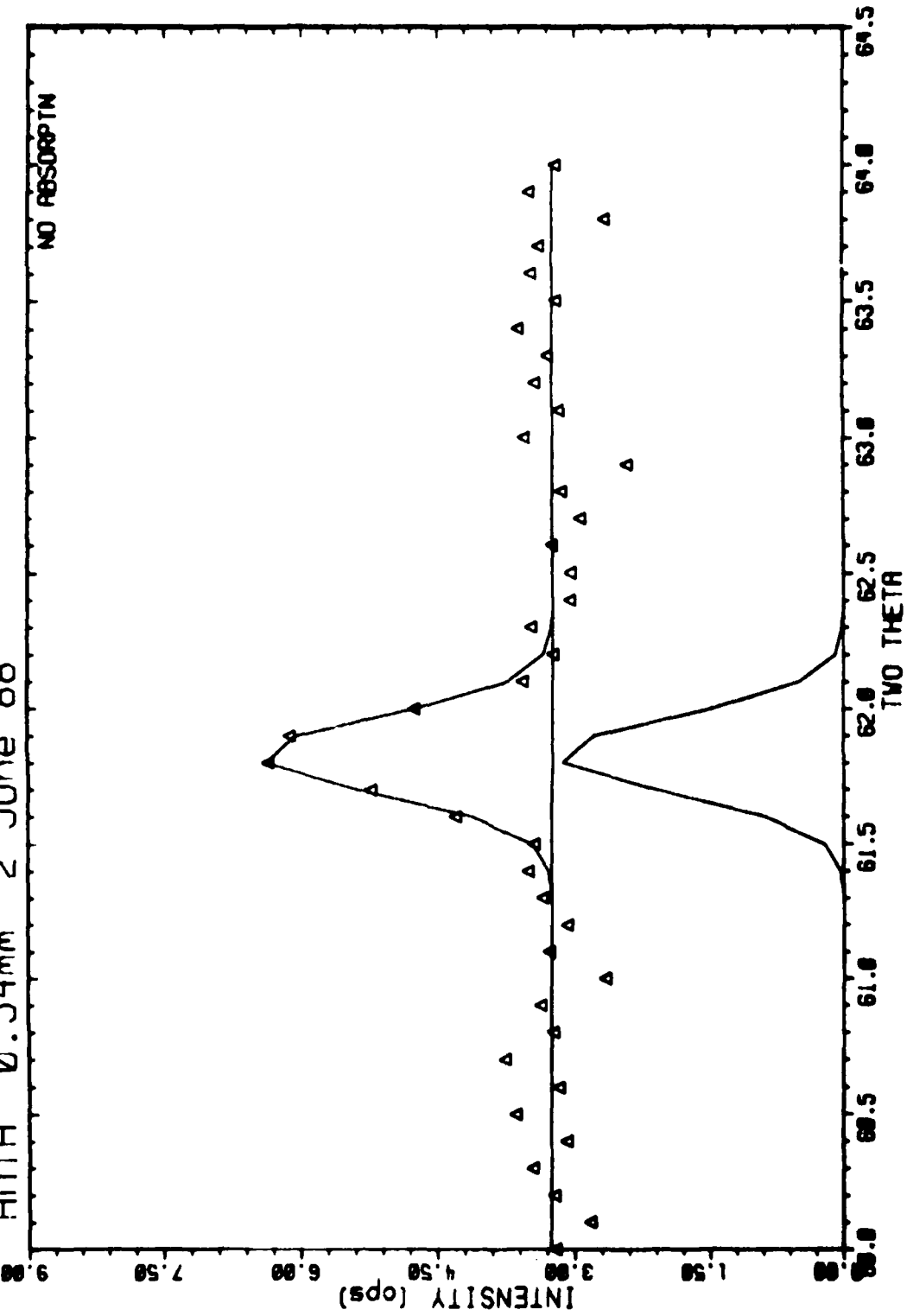


Figure 21. Curve-Fit Beryllium Acetate Diffraction Scan Used to Measure Instrumental Broadening Effects.

An example of the convolution effect of the instrumental broadening on a theoretical (00,2) reflection of  $L_C = 100\text{\AA}$  is shown in Figure 22 along with the original curve. With larger graphite crystals with narrower profiles, this effect is more pronounced. A theoretical asymmetric 2-D profile constructed from equations 4 and 5 is shown in Figure 23 as well as this reflection convoluted with the instrumental profile. Note that convolution of the theoretical peak with the instrumental breadth not only increases the profile width but shifts the peak maximum to a higher angle as well.

### 3.4 MISORIENTATION

The structural models shown in section 3.1 show varying amounts of misorientation of the graphite crystals relative to the fiber axis. Guigon et al. [11-13] have recently shown that there are two forms of misalignment: the broad meandering of fibrils as shown in Figures 13 and 14, as well as crystals within fibrils misaligned in so-called "wrinkled sheets." WAXD only sees the average misalignment including the internal structures and any misalignment of the fibers in the sample bundle.

Figure 24 shows two typical fiber bundles mounted for WAXD; both show very little if any misalignment of the fibers in their bundles. This source of error can be considered negligible.

The primary effect of crystal misalignment in WAXD is to broaden the azimuthal dependence of the intensity. For perfectly aligned crystals, intensity should be confined to a pair of spots in a WAXD photo; as the crystals become more misaligned, the spots will grow into arcs which will eventually become rings for completely random arrangements of crystals. This broadening of arcs can be seen in the WAXD photos in Appendix A by examining the P-series whose arcs become narrower as the fiber modulus increases.

Several methods for quantifying the azimuthal dependence have been tabulated [5,17,29], but at best they are only useful for relative ranking of materials. The absolute values of the

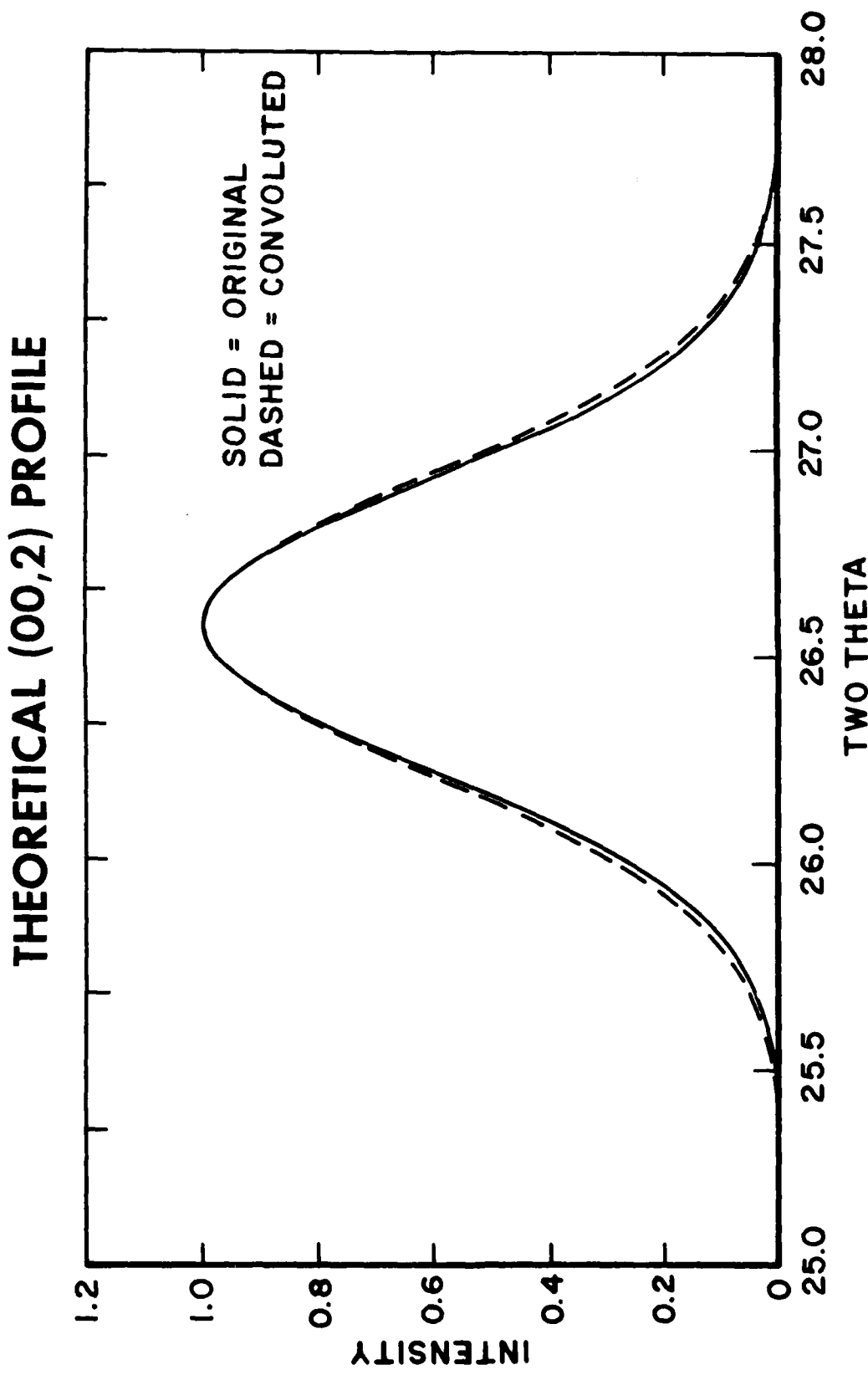


Figure 22. Theoretical (00,2) Reflection With and Without Instrumental Broadening Folded in for  $L_c = 100 \text{ \AA}$ .

## 2-D THEORETICAL PROFILES

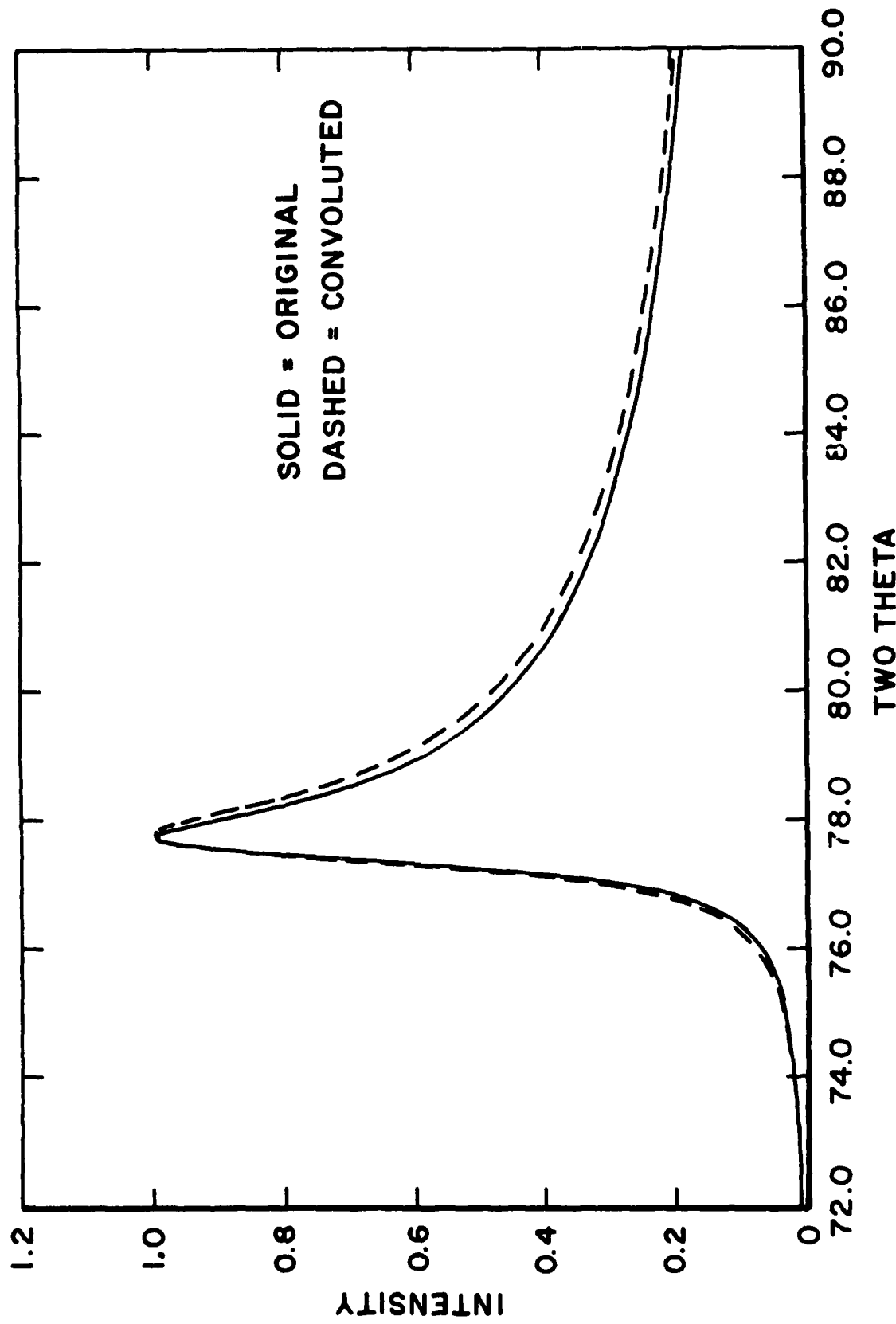
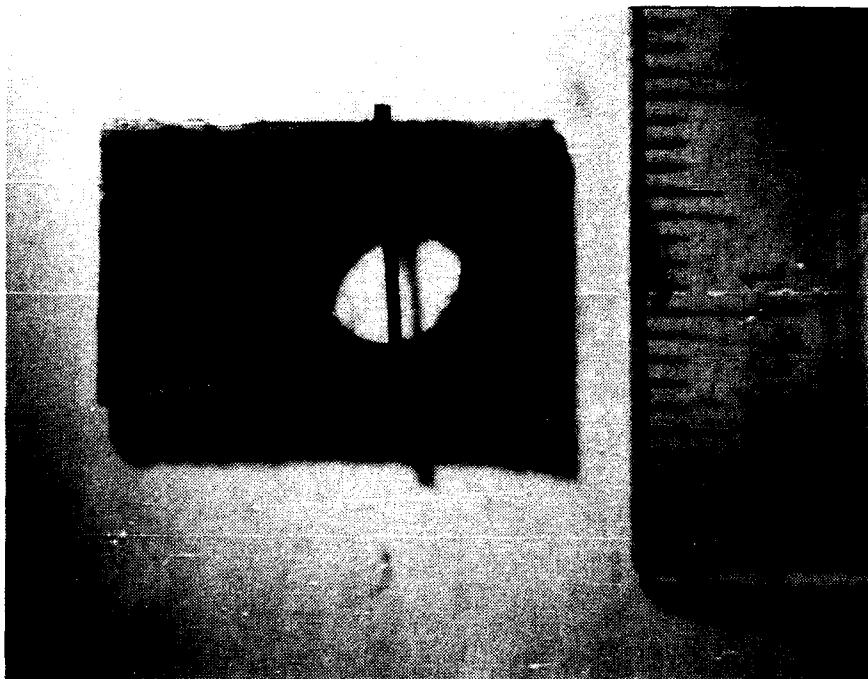


Figure 23. Theoretical Asymmetric 2-D Profile With and Without Instrumental Broadening Folded in for  $L_a = 100 \text{ \AA}$ .

(b)



(a)

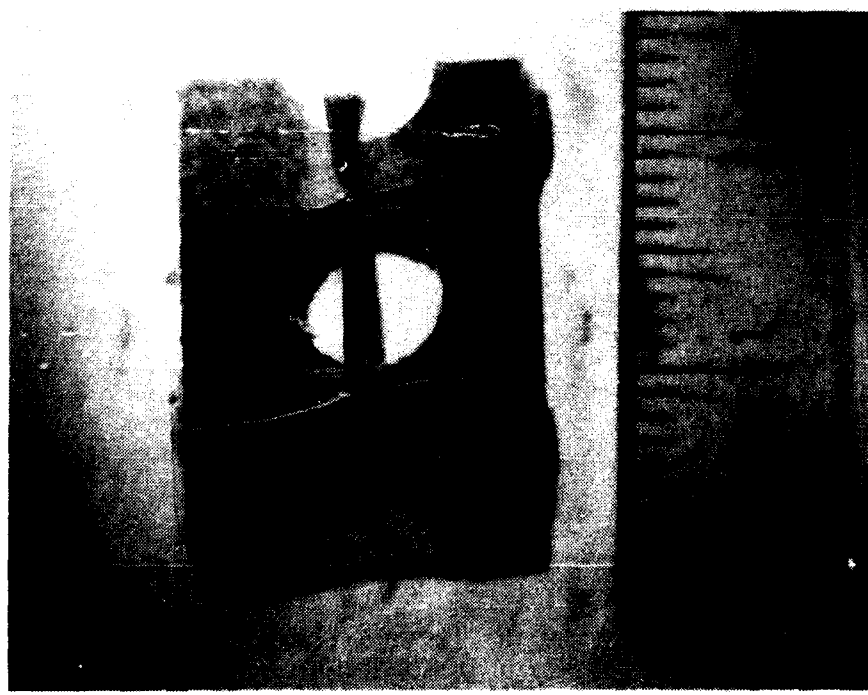


Figure 24. Typical Fiber Sample Bundles: (a) Mounted With Tape at Fiber Ends and  
(b) Mounted in Cyanomethylacrylate Glue.

azimuthal dependence have been used [see e.g. 13,28] to estimate fiber modulus, but these semi-empirical techniques are not as accurate as direct mechanical measurements of the fibers.

Figure 25 shows two azimuthal distributions for fibers showing the greater breadth for the lower modulus fiber. Reduction of the intensity distributions to single numbers includes:

$$Z = B(1/2, \phi) = \text{full-width at half maximum in } \phi \quad (13)$$

$$R_{0z} = \frac{\int_0^{\pi/2} I(\phi) \sin^3 \phi \, d\phi}{\int_0^{\pi/2} I(\phi) \sin \phi \, d\phi} \quad (14)$$

$$a_{10} = \frac{\int_0^{\pi/18} \pi F(\phi)^2 \, d\phi}{\int_0^{\pi/2} \pi F(\phi)^2 \, d\phi} \quad (15)$$

where  $\phi$  is the fiber colatitude ( $90^\circ - \chi$  when the fiber is parallel to  $\chi = 0^\circ$ ),  $F(\phi)$  is the azimuthal intensity normalized to  $\phi = 0^\circ$ , and  $\pi/18 = 10^\circ$ .

Equations 14 and 15 require significantly more work than equation 13 but do not give any additional or more useful information. Equation 13 is the method of choice for misorientation of the fibers' graphite planes using the  $(00,2)$  reflection full-width at half maximum (FW-HM).

Misorientation of the graphitic planes has been shown above to generate azimuthal dependence of intensity. For the  $(00,2)$  reflection, this is equivalent to the crystal plane normals sweeping out not a plane but a solid figure centered about the equator. One can think of a continuous mountain ridge of constant height circling the equator, the height of this ridge proportional to the probability of a crystal normal existing at that latitude. A very sharp ridge corresponds to a highly

THU. 17 NOV 1988 16:58:48

GRAPH NUMBER 2

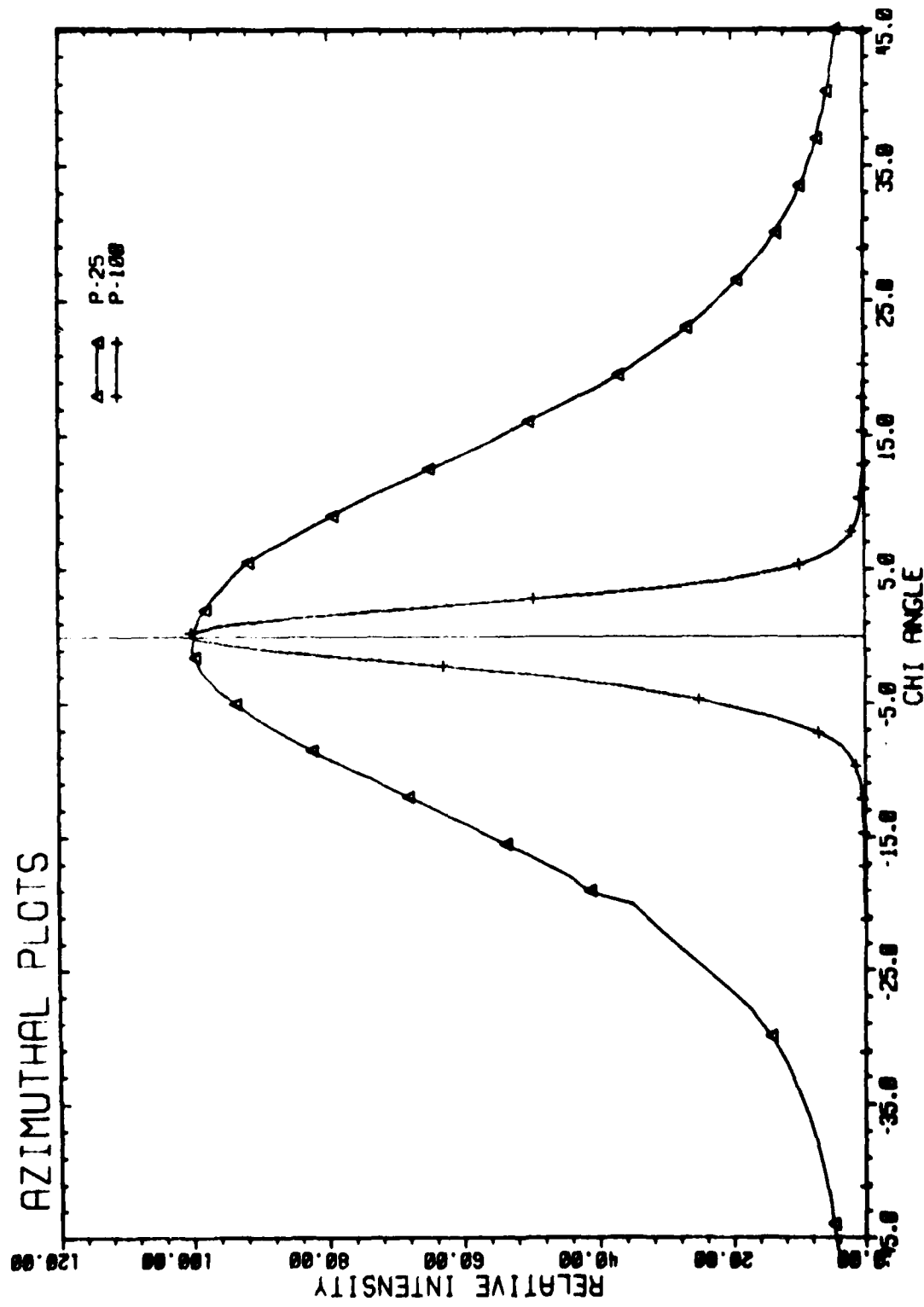


Figure 25. Plots of  $(00, 2)$  Azimuthal Distributions for P-25 and P-100 Carbon Fibers.

oriented fiber, and a poorly oriented fiber would have a gently sloping ridge.

The meridional reflections'  $(hk)$  and  $(hk, 0)$  normals orientation probabilities can be viewed as mountains at each of the poles. The  $(00, 2)$  full-width at half maximum will also define the  $(hk)$  and  $(hk, 0)$  misorientation mountain FW-HM (this will be convoluted into the persistence length probabilities mountain of section 3.1). Misorientation is the major reason the  $(10)$  and/or  $(10, 0)$  reflection is visible in flat-film photos and why its intensity decreases as the crystal orientation increases (see again the P-series of photos in Appendix A).

Off-axis reflections also become visible from misorientation as explained near the end of section 2.2. The intensity of the  $(10, 1)$  reflections in the WAXD photos of higher modulus fibers is generally greater than  $(10)$  and  $(10, 0)$  even though the maximum probability is lower, because at the collection angles relative to the fiber axis (also called colatitudes) which are equal to one-half the respective Bragg angles, the probabilities are generally greater.

## 4. RESULTS

### 4.1 MATERIALS

A series of commercially available carbon fibers were examined in this study. Those fibers, their manufacturers, and some of their published mechanical properties are listed in Table 1. These fibers were picked because of their range of properties and availability. Both Pitch-based (P-series) and PAN-based fibers were included for comparison.

In addition, an experimental annealed vapor grown carbon fiber was included as an example of a very highly graphitized fiber. This fiber was supplied courtesy of Dr. Karren K. Brito of Applied Sciences, Inc., Yellow Springs, OH.

### 4.2 (00,2) RESULTS

The (00,2) results from WAXD for the samples above are given in Table 2. These results include  $d_{00,2}$ ,  $L_c$ , and  $Z_{00,2}$ . The  $d_{00,2}$  is from the position of the (00,2) reflection measured by curve fitting [34] the WAXD Bragg scan at  $\chi=0^\circ$  (equatorial scan) and using Bragg's Law (equation 2). Figure 26 shows an example of the curve-fit (00,2) reflection using P-55 with a  $\beta = 0.859^\circ$  and  $d_{00,2} = 3.523\text{\AA}$  from a maximum at  $25.28^\circ 2\theta$ . In this table  $L_c$  is calculated from the Scherrer equation (equation 8) using the same curve fit as  $d_{00,2}$  corrected for instrumental broadening by equation 11. An azimuthal scan of (00,2) reflection was curve fit to obtain the full-width at half maximum or  $Z_{00,2}$  of each fiber. Figure 27 shows P-55's azimuthal scan for the (00,2) reflection ( $Z_{00,2} = 14.1^\circ$ ).

The trends seen here have been observed before:  $d_{00,2}$  and  $Z_{00,2}$  decrease, while  $L_c$  increases as the measured tensile modulus increases. Apparently the big changes occur as the modulus passes 50 Msi:  $L_c$  increases from  $20-30\text{\AA}$  to greater than  $100\text{\AA}$ , and  $Z_{00,2}$  drops rapidly to single digits.

The differences between Pitch- and PAN-based fibers can be seen by comparing equivalent (modulus) pairs of fibers; e.g. P-25

TABLE 1  
FIBER MECHANICAL PROPERTIES [30-33]

<u>Fiber</u>	<u>Manufacturer</u>	Tensile Modulus <u>Msi (GPa)</u>	Tensile Strength <u>ksi (GPa)</u>	Compressive Strength <u>ksi (GPa)</u>
P-25	AMOCO	23 (159)	200 (1.38)	167 (1.15)
P-55	"	55 (379)	250 (1.72)	123 (0.85)
P-75	"	75 (517)	300 (2.07)	100 (0.69)
P-100	"	105 (724)	325 (2.24)	70 (0.48)
P-120	"	120 (827)	325 (2.24)	65 (0.45)
T-300	AMOCO	34 (231)	470 (3.24)	417 (2.88)
AS4	Hercules/Magnamite	34 (231)	528 (3.64)	390 (2.69)
T-40	AMOCO	42 (290)	500 (3.45)	400 (2.76)
G40-700	BASF/Celion	44 (300)	720 (4.96)	na
IM6	Hercules/Magnamite	45 (308)	620 (4.27)	na
G45-700	BASF/Celion	45 (310)	700 (4.83)	na
HMS	Hercules/Magnamite	50 (345)	320 (2.21)	na
T-50	AMOCO	57 (393)	350 (2.41)	233 (1.61)
GY-70	BASF/Celion	75 (517)	270 (1.86)	153 (1.05)

na - Not available

TABLE 2  
SUMMARY OF (00,2) WAXD CARBON FIBER RESULTS

<u>Fiber</u>	$d_{00,2}$ <u>(Angstroms)</u>	$L_c$ <u>(Angstroms)</u>	$\theta_{00,2}$ <u>(degrees FW-HM)</u>
<u>Pitch-Based</u>			
P-25	3.479	26	31.9
P-55	3.426	114	14.1
P-75	3.416	157	11.0
P-100	3.385	208	5.6
P-120	3.378	228	5.6
<u>PAN-Based</u>			
T-300	3.496	16	35.1
AS4	3.521	10	36.8
T-40	3.515	17	30.2
G40-700	3.495	21	29.1
IM6	3.464	20	33.7
G45-700	3.470	25	26.7
HMS	3.427	62	19.7
T-50	3.429	57	16.4
GY-70	3.405	173	9.6
<u>Vapor Grown</u>			
Applied Sciences	3.373	345	14.8

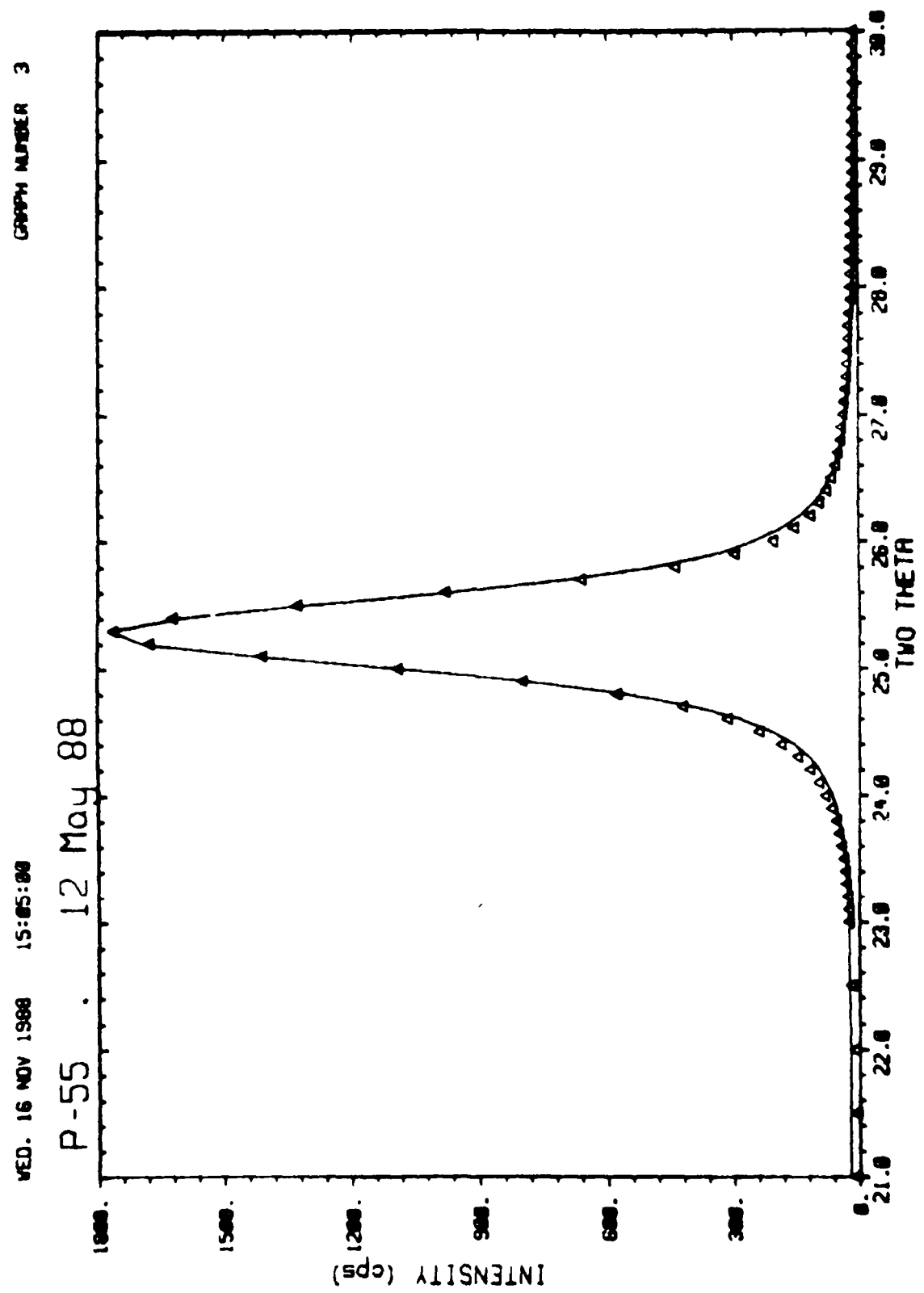


Figure 26. Curve-Fit (00,2) Bragg Reflection of P-55.

WED. 16 NOV 1988 15:10:34

GRAPH NUMBER 3

P-55 2th=25.3 13 May 88

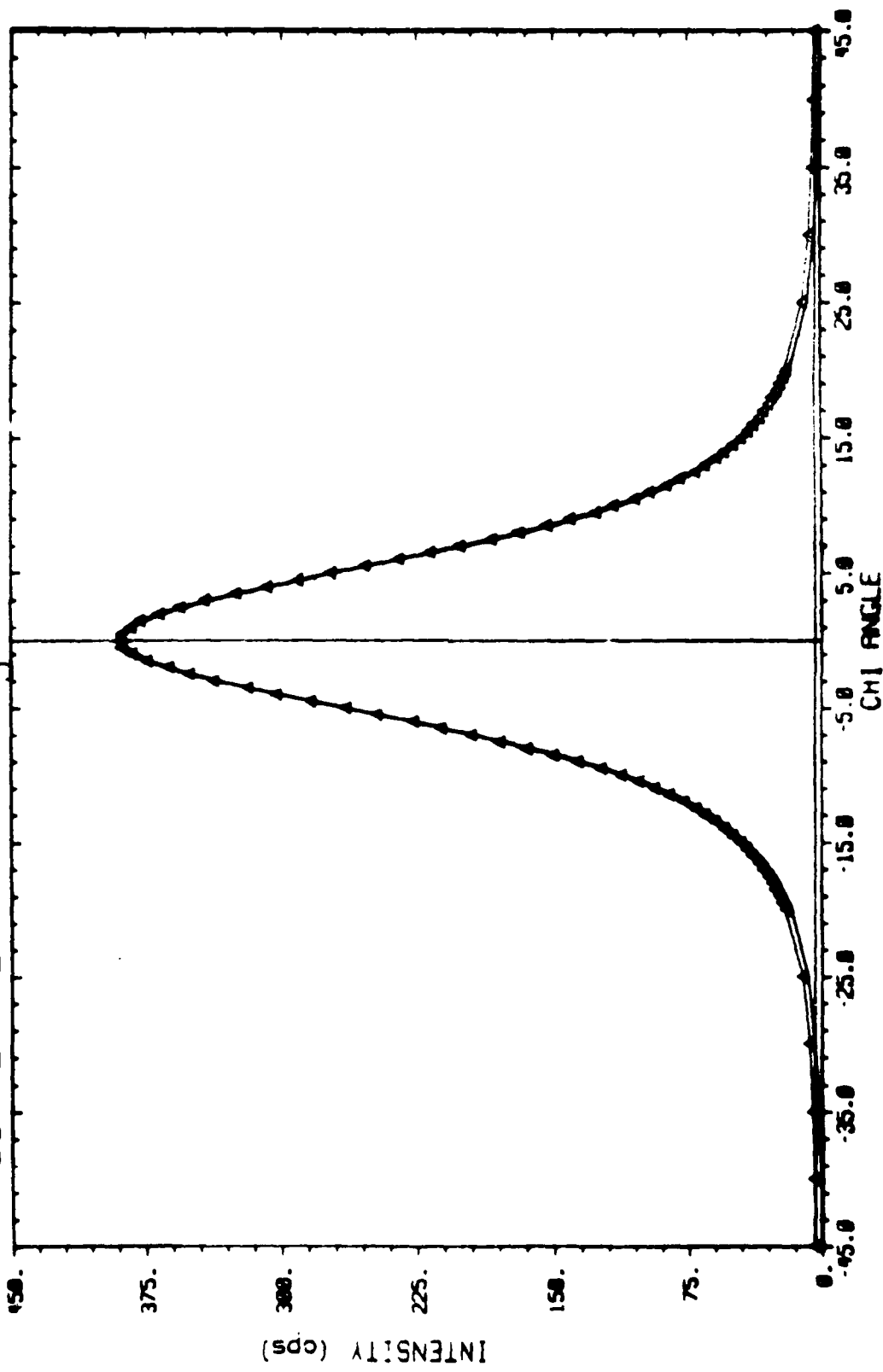


Figure 27. Curve-Fit (00,2) Azimuthal Scan of P-55.

and AS4, P-55 and T-50, and P-75 and GY-70. The first and third pairs' properties are roughly equivalent. In the second pair P-55 appears to have made the morphological jump to larger, more perfect crystals and T-50 is intermediate between the higher and lower modulus morphology indicating some lag in the development of larger structures in PAN-based fibers as the modulus is built-up in processing.

The vapor grown Applied Sciences carbon fiber does not have as highly oriented planes ( $Z_{00,2} = 14.8^\circ$ ) but the graphitization is much higher than the other fibers since the  $d_{00,2} = 3.373\text{\AA}$  is the closest to the ideal  $3.3535\text{\AA}$  and the crystal size,  $L_c = 345\text{\AA}$ , is the largest measured.

#### 4.3 ADVANCED $L_c$ RESULTS

The advanced  $L_c$  techniques of Hosemann or Buchanan and Miller require higher order reflections. Figure 28 shows a complete equatorial scan of P-100 with the higher order (00,1) reflections. Only 8 of the 15 fibers examined had all three (00,1) reflections resolvable for use in determining which of the techniques to use (the remaining 7 fibers did have two orders).

The two techniques for separating crystalline disorder from size broadening of Hosemann and Buchanan and Miller each expressed for both Gaussian (equations 9 and 10) or Cauchy distributions yield four possible plots. Figures 29-32 show these four plots for P-55. Table 3 gives each plot's correlation coefficient and root mean square error (averages for the 8 fibers used here).

While the correlation coefficient for both of the Buchanan and Miller plots is only slightly smaller than the Hosemann plots and the Gaussian line actually gives the lowest RMS, this method was not considered correct since as often as not the intercept values were negative. This would give a physically impossible negative crystallite size.

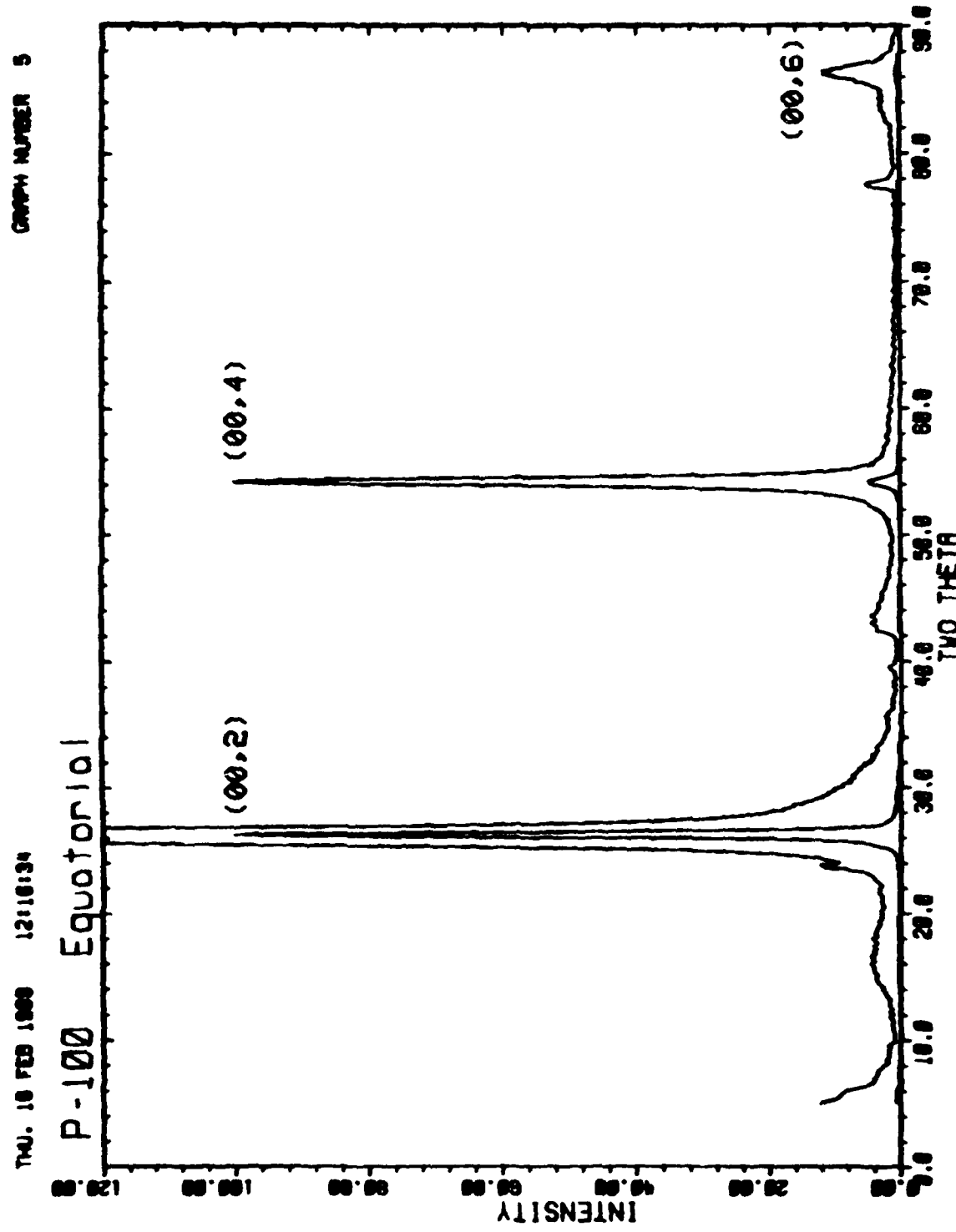


Figure 28. Complete Equatorial Bragg Scan of P-100.

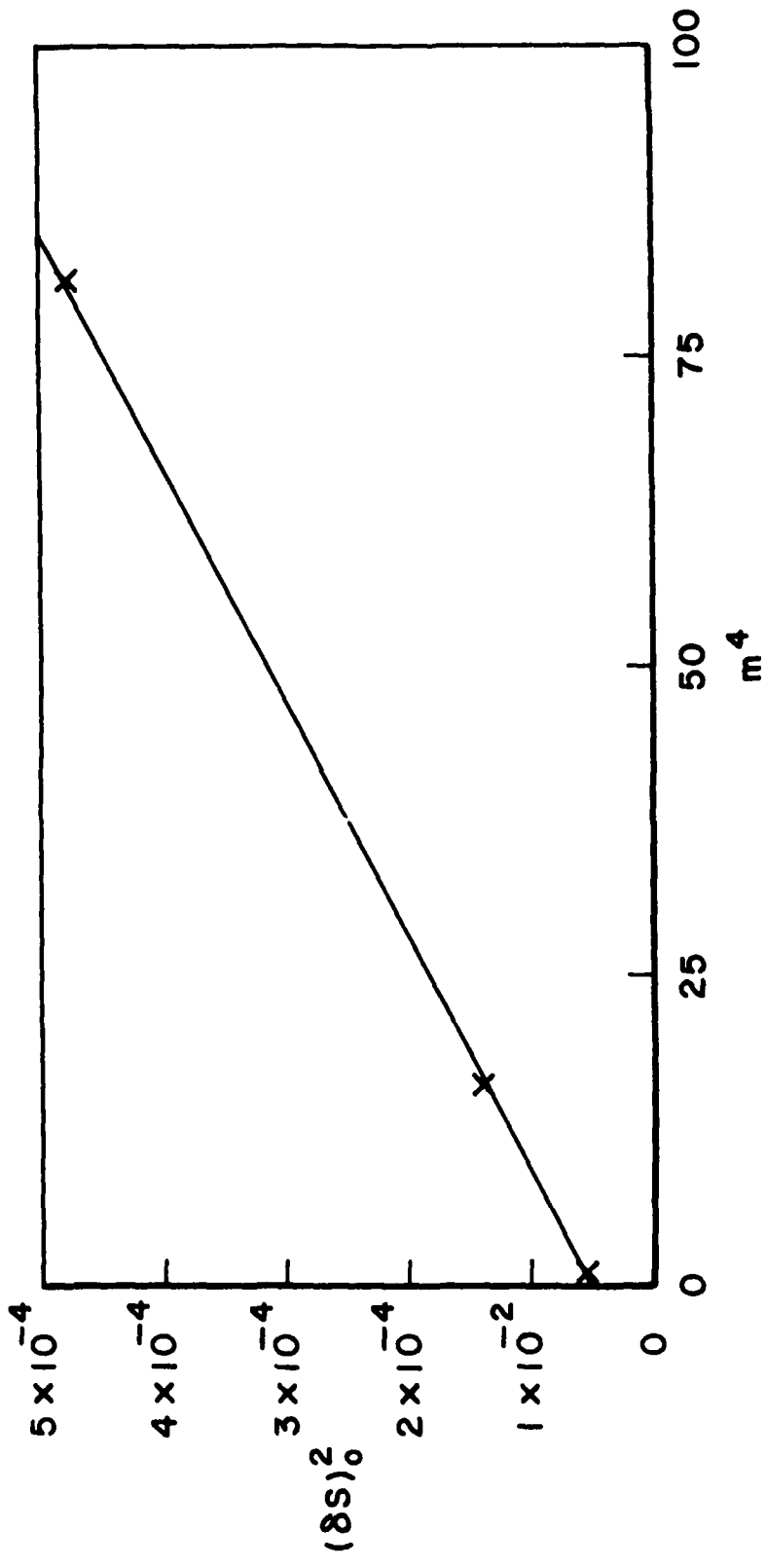


Figure 29. Hossemann Plot for P-55 Assuming a Gaussian Distribution for Crystalline Disorder.

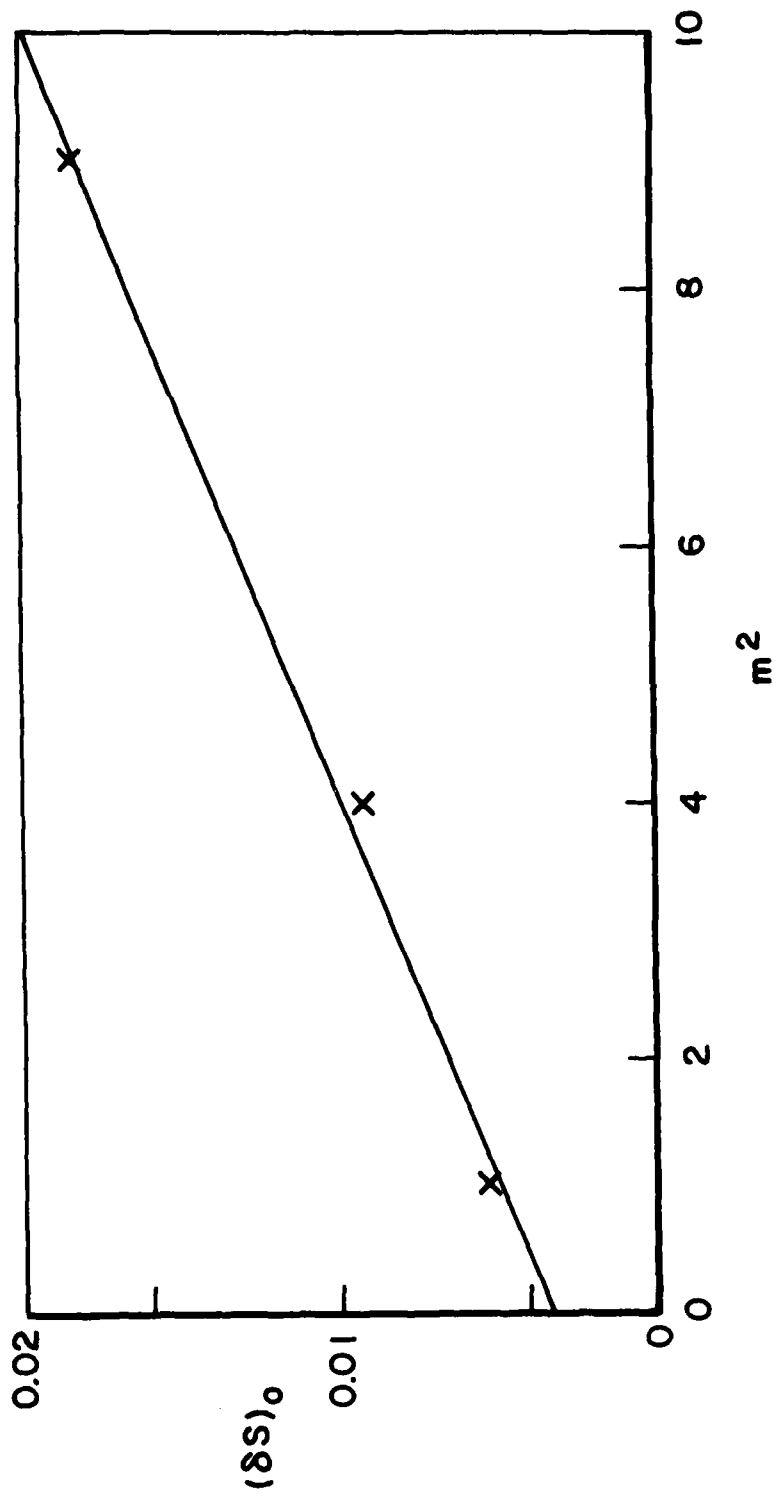


Figure 30. Hosemann Plot for P-55 Assuming a Cauchy Distribution for Crystalline Disorder.

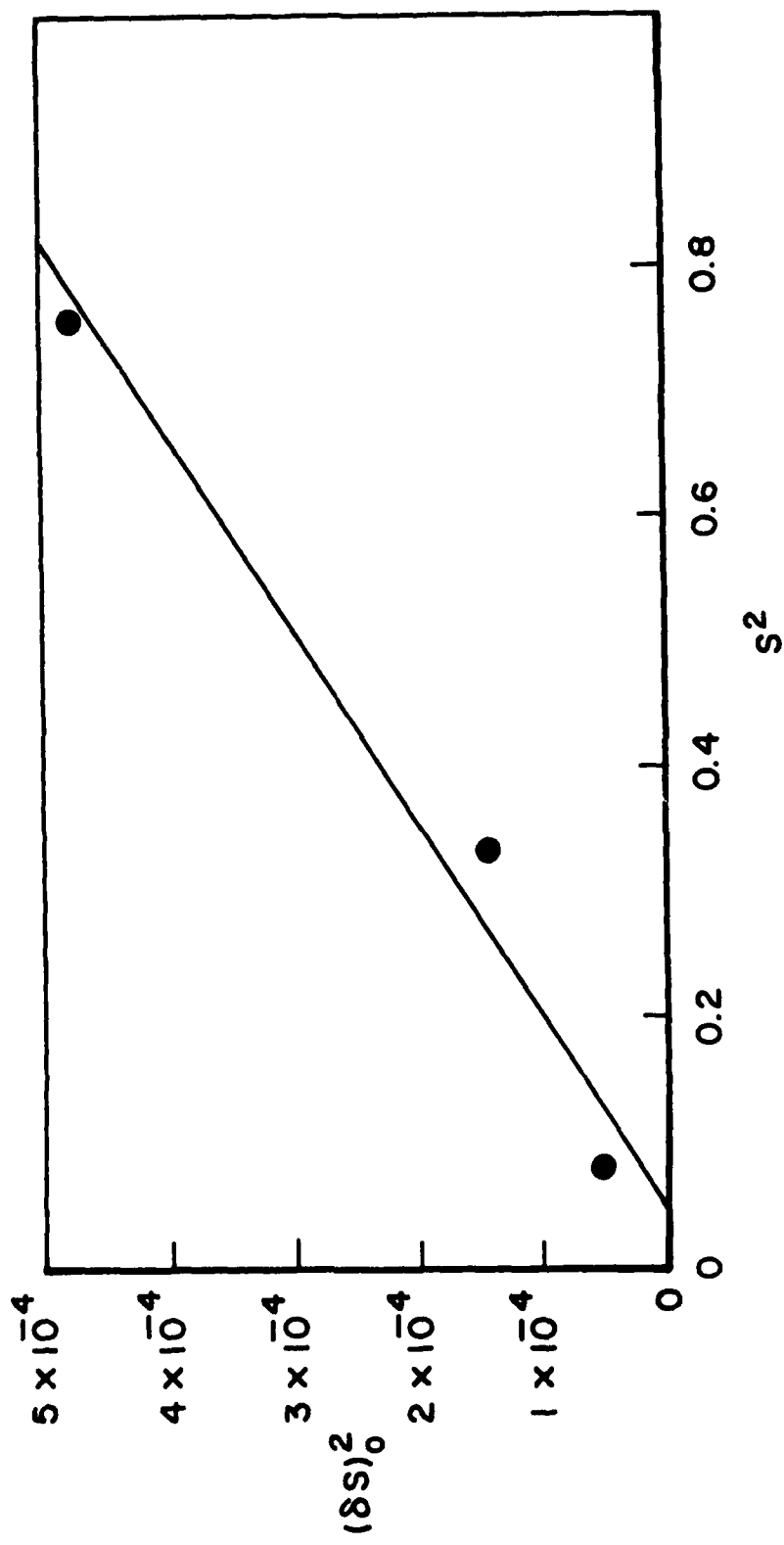


Figure 31. Buchanan and Miller Plot for P-55 Assuming a Gaussian Distribution for Crystalline Disorder.

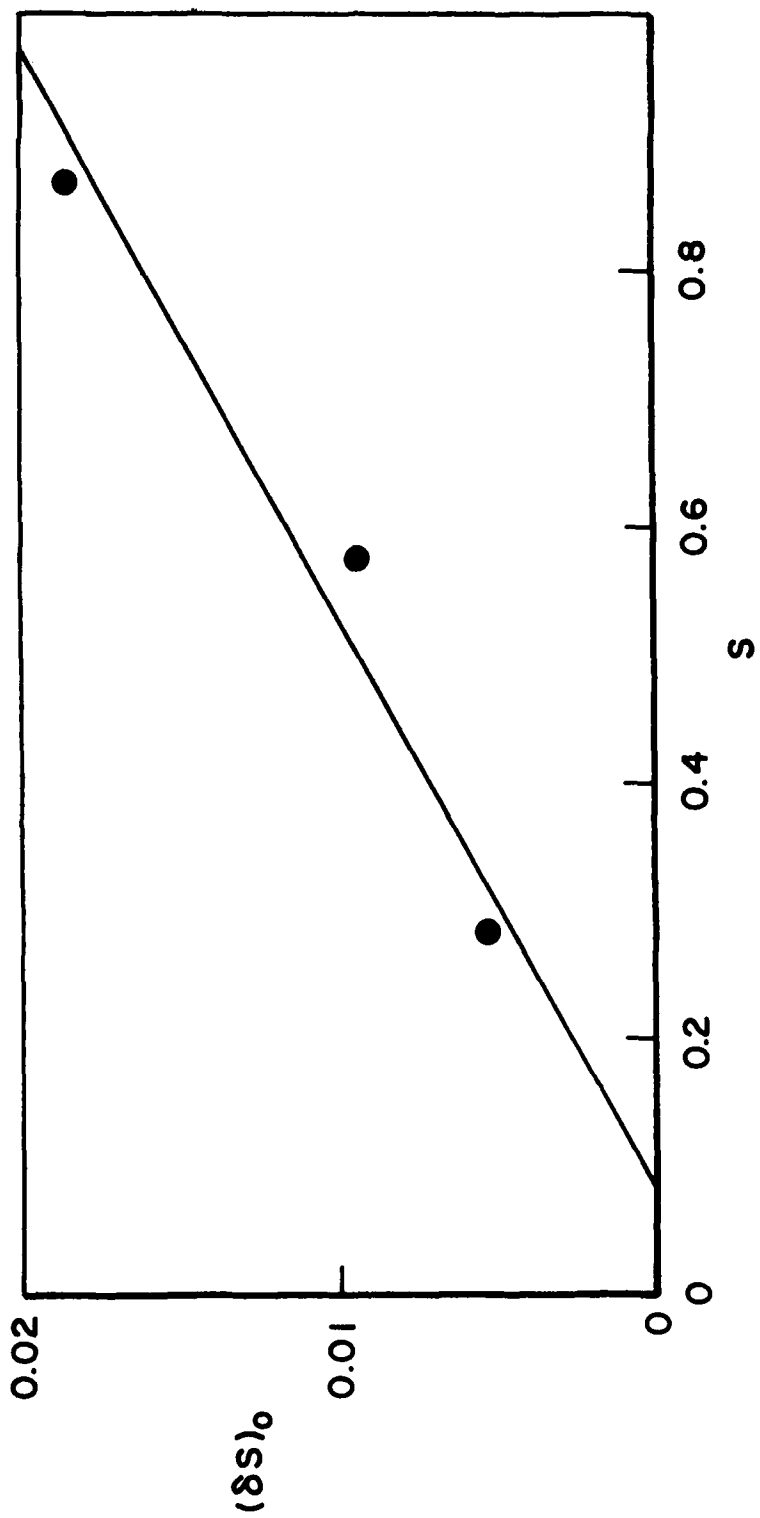


Figure 32. Buchanan and Miller Plot for P-55 Assuming a Cauchy Distribution for Crystalline Disorder.

TABLE 3  
ADVANCED  $L_c$  ANALYSIS COMPARISON

	<u>Correlation Coefficient</u>	<u>Root Mean Square</u>
<u>Hosemann</u>		
Gaussian	0.984	0.00014
Cauchy	0.994	0.00069
<u>Buchanan and Miller</u>		
Gaussian	0.976	0.00008
Cauchy	0.972	0.00140

The RMS for the Gaussian plots of Hosemann were less than a quarter of the Cauchy plots RMS. This, plus the fact that Gaussian is more likely from a theoretical point of view, led to its use for all of the fibers. Table 4 shows the Hosemann Gaussian results and compares the crystal sizes to the values found by the Scherrer equation. In general this Hosemann analysis gives crystal sizes slightly greater than the Scherrer equation as expected, and of course the relative rankings of the fiber's crystal sizes are the same. The break in properties near 50 Msi fiber modulus is also seen in the disorder parameter,  $g_{II}$  as it falls below 0.03 as the modulus increases past this range.

#### 4.4 3-D AND $L_a$ RESULTS

There are several factors to consider in obtaining a measure of the crystal size,  $L_a$ . The first is which of the several methods mentioned in sections 3.2 and 3.3 should be used, and second is the effects of instrumental broadening on the measured profiles. Table 5 has the calculated  $L_a$  values for two fibers (P-25 and AS4) from both the (10) and (11) reflections.

The equations of Warren and Bodenstein [14] (Eqn. 7 w/  $k' = 0.28$  and Eqn. 3) and Ruland [22] (Eqn. 7 w/  $k' = 0.32$  and Eqn. 6) were used to generate  $L_a$  values in the top half of the table from the peak maximum positions and peak breadths respectively. The

TABLE 4  
ADVANCED  $L_c$  ANALYSIS RESULTS

Fiber	Number of Orders Used	$L_c$ (Angstroms)		Disorder ( $g_{II}$ )
		Hosemann	Scherrer	
<u>Pitch-Based</u>				
P-25	2	36	26	0.0794
P-55	3	99	114	0.0301
P-75	3	140	157	0.0233
P-100	3	159	208	0.0166
P-120	3	188	228	0.0182
<u>PAN-Based</u>				
T-300	2	19	16	0.0820
AS4	3	15	10	0.0694
T-40	2	21	17	0.0688
G40-700	2	27	21	0.0707
IM6	2	24	20	0.0785
G45-700	2	29	25	0.0626
HMS	3	78	62	0.0413
T-50	3	66	57	0.0409
GY-70	3	138	173	0.0305
<u>Vapor Grown</u>				
Applied Sciences	3	374	345	0.00828

TABLE 5  
SUMMARY OF (hk) WAXD CRYSTAL PLANE SIZE ( $L_a$ ) MEASUREMENT  
TECHNIQUES (SIZES IN ANGSTROMS)

	P-25		AS4	
	(10)	(11)	(10)	(11)
<u>Warren &amp; Bodenstein</u>				
Position <sup>a</sup>	35	26	31	19
Breadth <sup>b</sup>	49	39	41	30
<u>Ruland</u>				
Position <sup>c</sup>	40	29	35	22
Breadth <sup>d</sup>	51	40	43	31
<u>Warren &amp; Bodenstein<sup>e</sup></u>				
Position	50	36	42	24
Breadth	53	42	43	31
<u>Ruland<sup>f</sup></u>				
Position	48	38	42	26
Breadth	55	44	44	33

a - Equation 7 with  $k' = 0.28$

b - Equation 3

c - Equation 7 with  $k' = 0.32$

d - Equation 6

e - Theoretical profiles [14] convoluted with the instrumental breadth profile

f - Theoretical profiles from Equations 4 and 5 [22] convoluted with the instrumental breadth profile

bottom half of the table went back to the original equations (such as equations 4 and 5) for these workers, generated a series of profiles for varying crystal sizes, and then folded the instrumental profiles into those theoretical curves. These convoluted profiles were then compared to the experimental curves to again get measures of  $L_a$  from the peak maximum positions and breadths.

As pictured in Figure 23, the instrumental broadening affects the measured profiles; but at the crystal sizes of these fibers, the differences are not as great as the differences between the position and breadth calculations. The variation between the two groups is even less. Considering the work involved in the correction for the instrumental broadening and the lack of better results when it is used (except to make the position and breadth results closer), it should be dropped. A good compromise in effort and results is to use Equation 6 to calculate  $L_a$  values.

The reason P-25 and AS4 were chosen for Table 5 is that both show no evidence of 3-dimensional crystals. The presence of 3-D crystals is another problem associated with calculating  $L_a$  since the equations used above all assume simple 2-D crystals and are not valid for 3-D or mixtures of 2-D and 3-D crystal reflections. Once the presence of 3-D crystals is detected, one can assume that mixed reflections are confounding the measurements.

Three-dimensional crystals are not easy to detect in meridional scans. As mentioned in section 2.3, off-axis reflections can be seen in meridional scans only when crystal misorientation is larger than the crystal tilt from the fiber axis; as will be seen below, 3-D crystals occur in fibers with low misorientation. Tilting fibers to  $\chi < 90^\circ$  or by the omega circle is necessary to reveal emerging 3-D reflections. This can be seen in Figure 33 which is a multiple plot of P-100 fiber diffraction obtained at  $\chi = 90^\circ$ ,  $\chi = 70^\circ$  (at  $\omega = 0^\circ$ ) and  $\chi = 90^\circ$  (at  $\omega = 20^\circ$ ). The  $\chi = 90^\circ$  or meridional scan shows absolutely no sign of the (10,1), but the other two scans are dominated by that reflection.

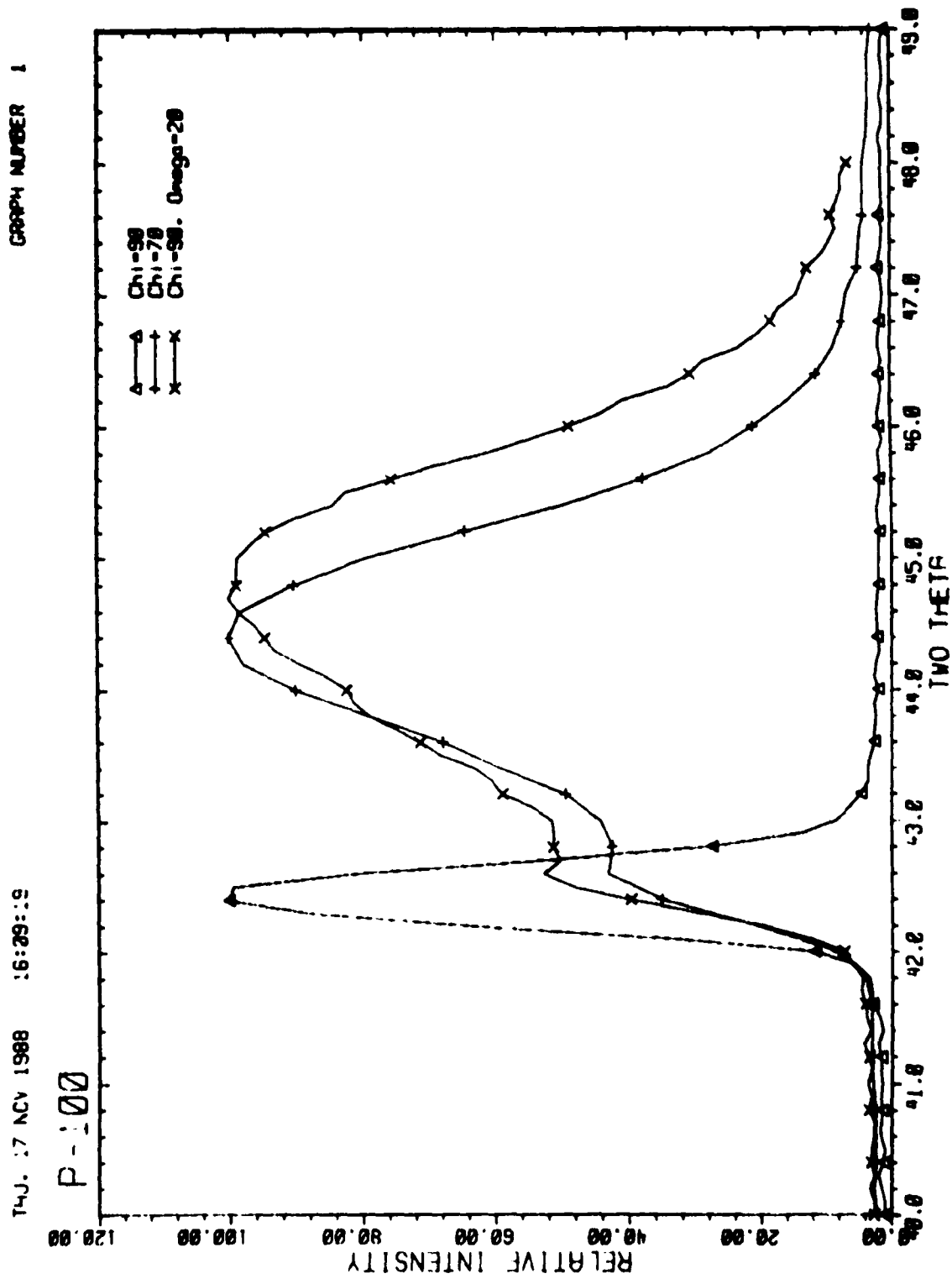


Figure 33. P-100 Diffraction Showing the Emergence of the (10,1) Off-Axis Reflection by Fiber Tilting.

Figure 34 is a complete meridional scan of P-100, and Figure 35 is a complete scan taken at  $\chi=70^\circ$ . Both scans have the major reflections annotated.

The two major off-axis reflections (10,1) and (11,2) are tilted  $17.6^\circ$  and  $20.2^\circ$  from the fiber axis so that  $\chi=70^\circ$  ( $90^\circ - 20^\circ$ ) (or  $\omega=20^\circ$ ) is close enough to the crystal tilt angle to observe either reflection. The error in (10,1) of  $2.4^\circ$  is less than any of these fibers misorientation and errs at an angle on the far side of the (10,0) reflection which is the major source of interference. Ideally each reflection should be examined at its optimum tilt angle, but practical considerations limited the current data collection.

The ideal locations [18] of the (10,0) and (10,1) reflections are  $42.4^\circ$  and  $44.6^\circ$  respectively. Since each of these peaks have typical full-widths at half-maximum of a few degrees, finite crystal sizes push the 2-D reflections to higher angles, and crystalline disorder of 3-D crystals push their reflections to lower angles, these reflections will almost always overlap. This overlap is shown in Figure 33 for P-100 which is generally accepted as having significant 3-D crystalline character. Only in the Applied Sciences' vapor grown carbon fiber are the (10,0) and (10,1) reflections resolved (see Appendix B).

The (11,2) off-axis reflection is more useful than the (10,1) to look for since it can be resolved better as the ideal locations [18] of the (11,0) and (11,2) reflections are  $77.5^\circ$  and  $83.5^\circ$  (see Appendix C). This is particularly obvious in transition fibers such as P-75 and GY-70; their (10,1) regions show what appears to be overlapping peaks, but their (11,2) regions show definite emergence of the off-axis reflection. Individual scans are in Appendices B and C, while multiple plots of several Pitch-based fibers are shown in Figures 36 (10,1) and 37 (11,2) and in Figures 38 (10,1) and 39 (11,2) for PAN-based fibers.

In the (10,1) region multiple plots, the overlap between (10,0) and (10,1) apparent in P-75 and GY-70 is also possible for

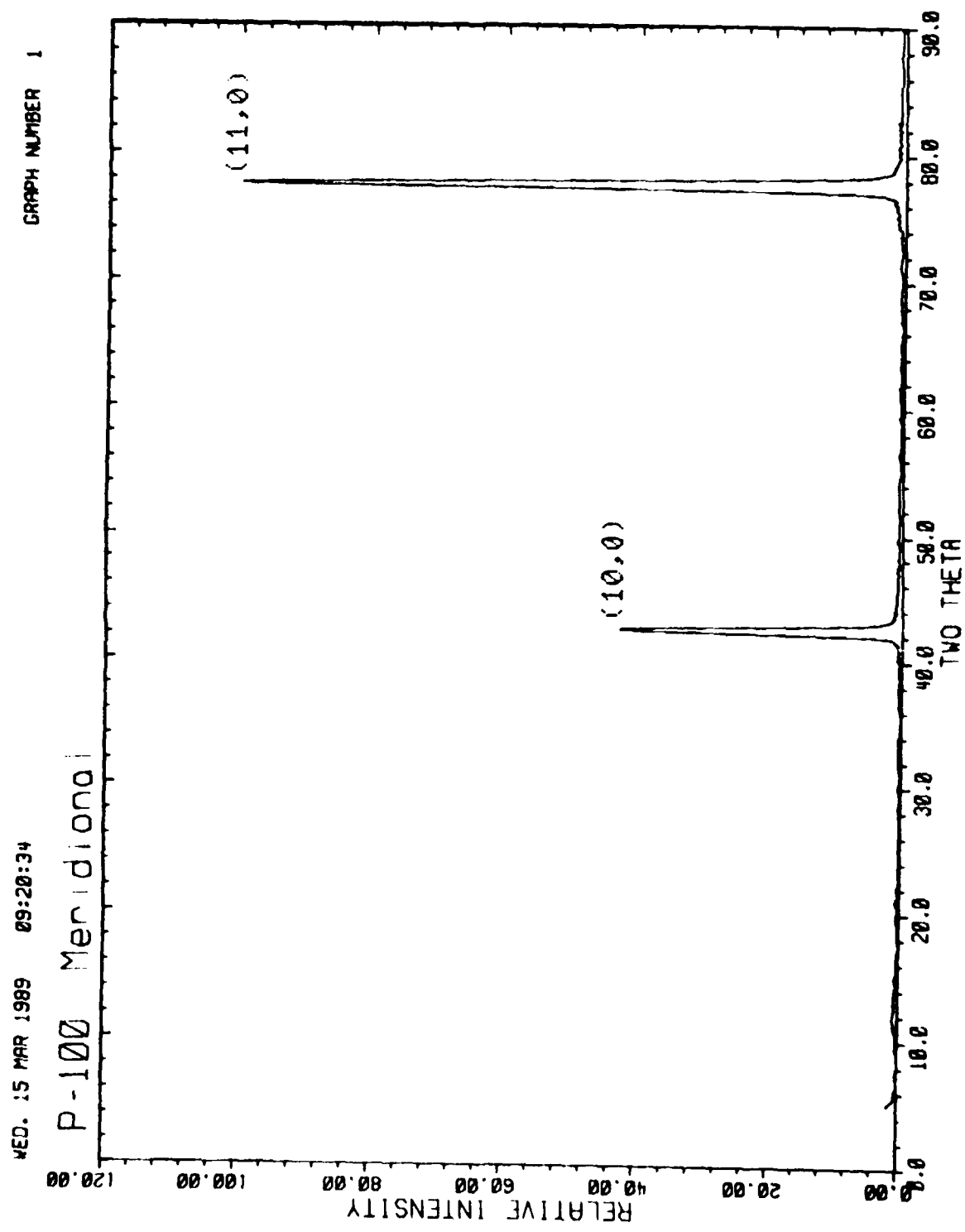


Figure 34. Complete Meridional ( $\text{Chi}=90^\circ$ ) Bragg Scan of P-100.

THU. 16 FEB 1989

12:46:18

P-100 OFF-Axis

GRAPH NUMBER 2

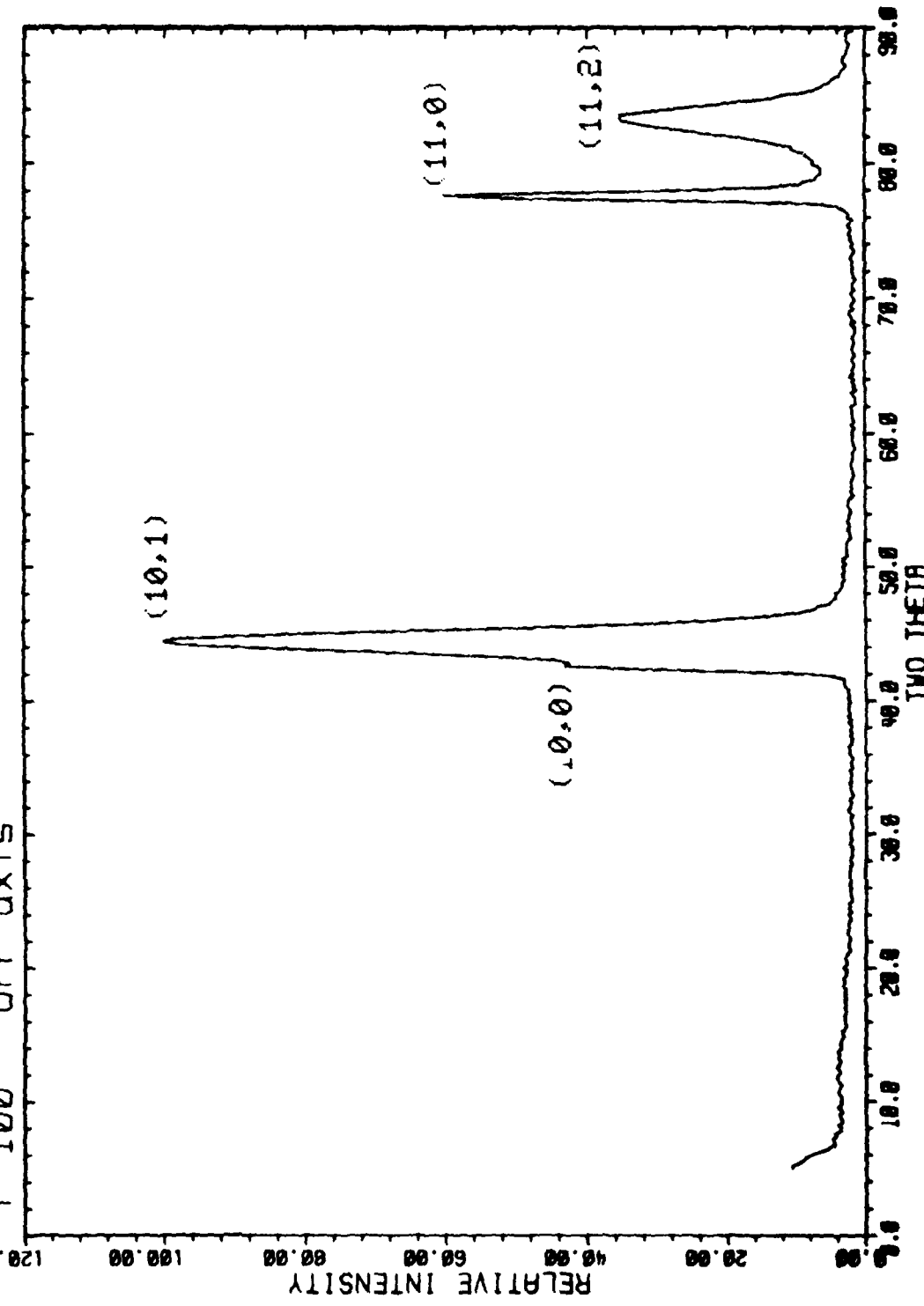


Figure 35. Complete Off-Axis ( $\chi = 70^\circ$ ) Bragg Scan of P-100.

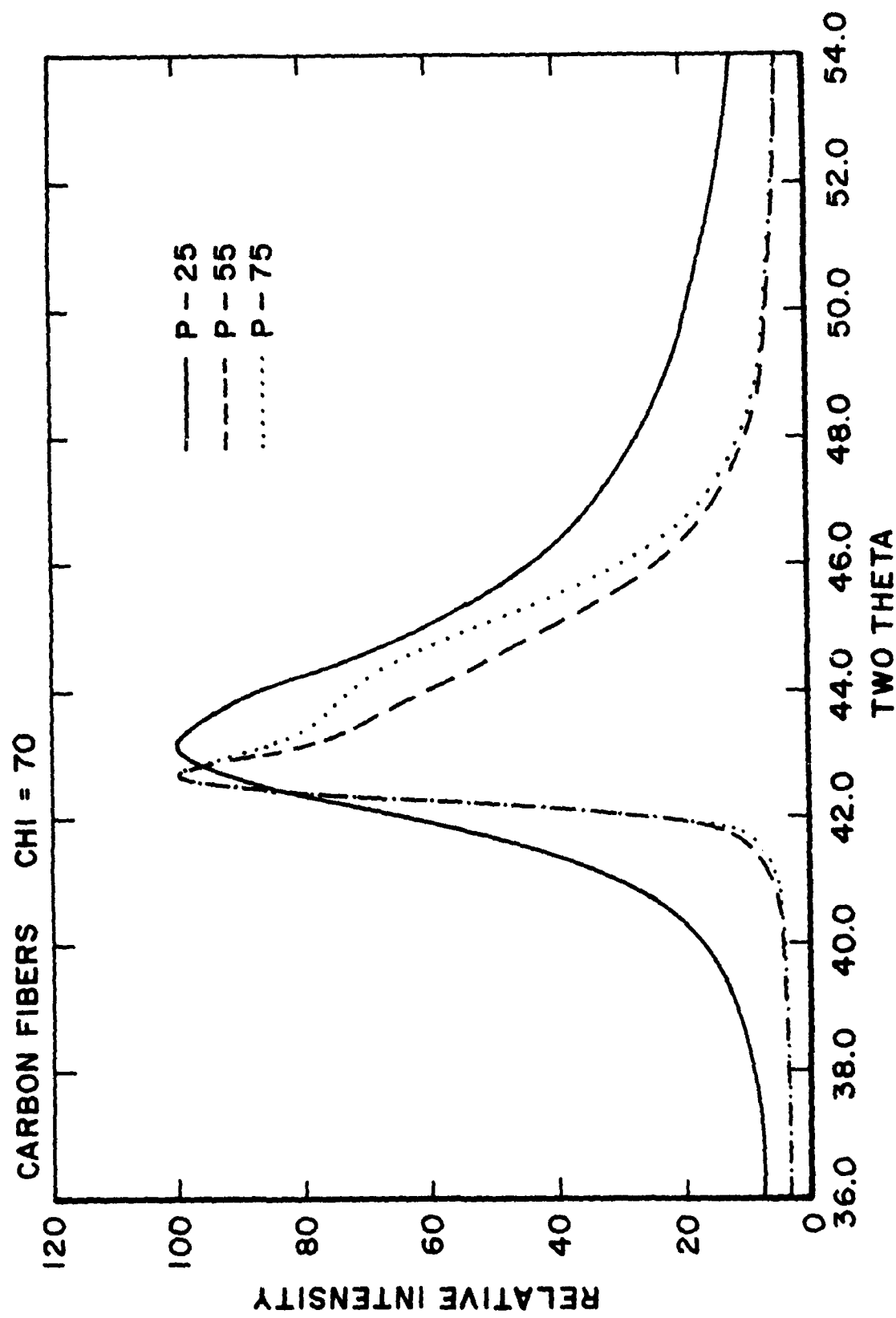


Figure 36. Bragg Scan of  $(10,1)$  Region in Some Pitch-Based Fibers.

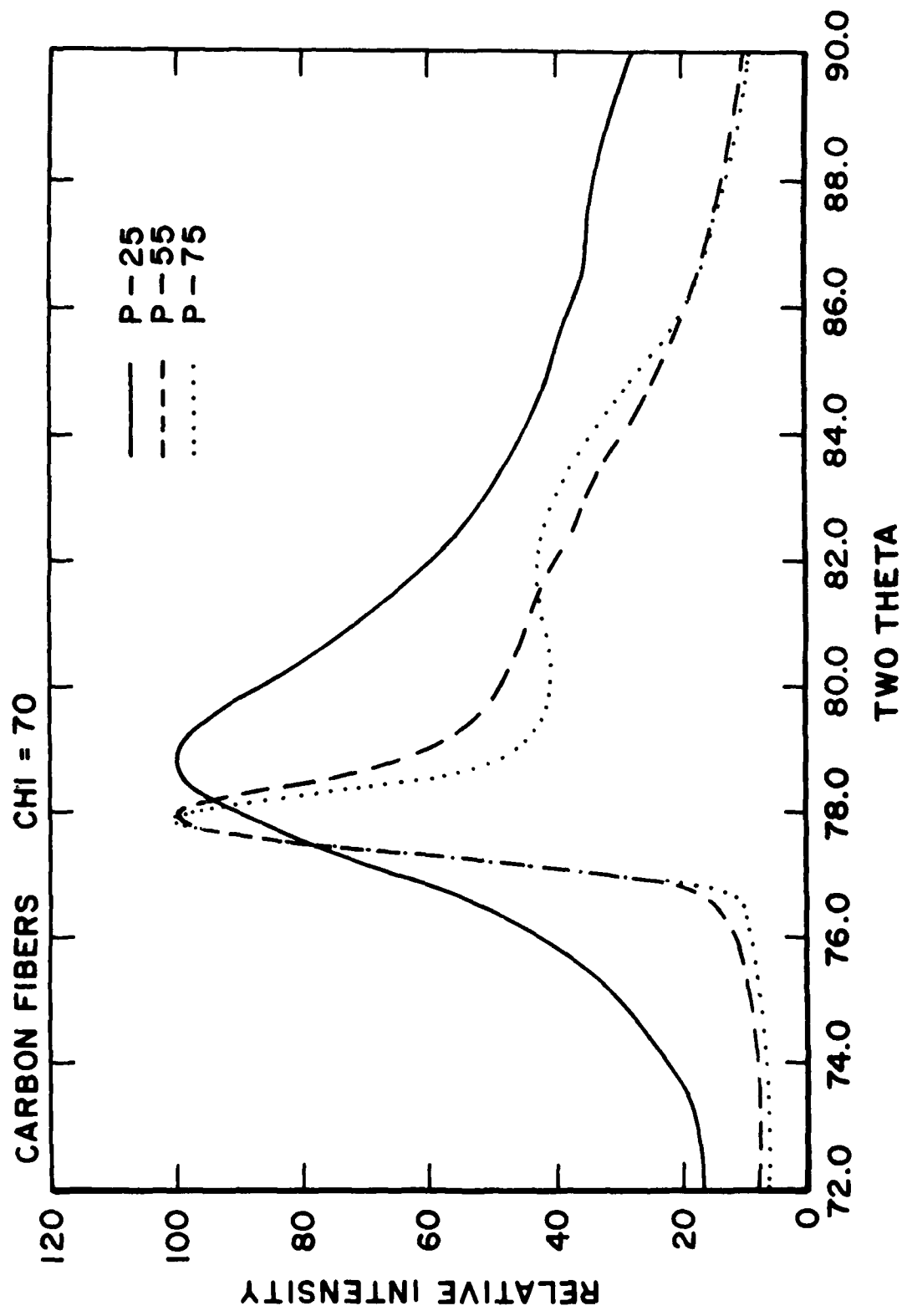


Figure 37. Bragg Scan of (11,2) Region in Some Pitch-Based Fibers.

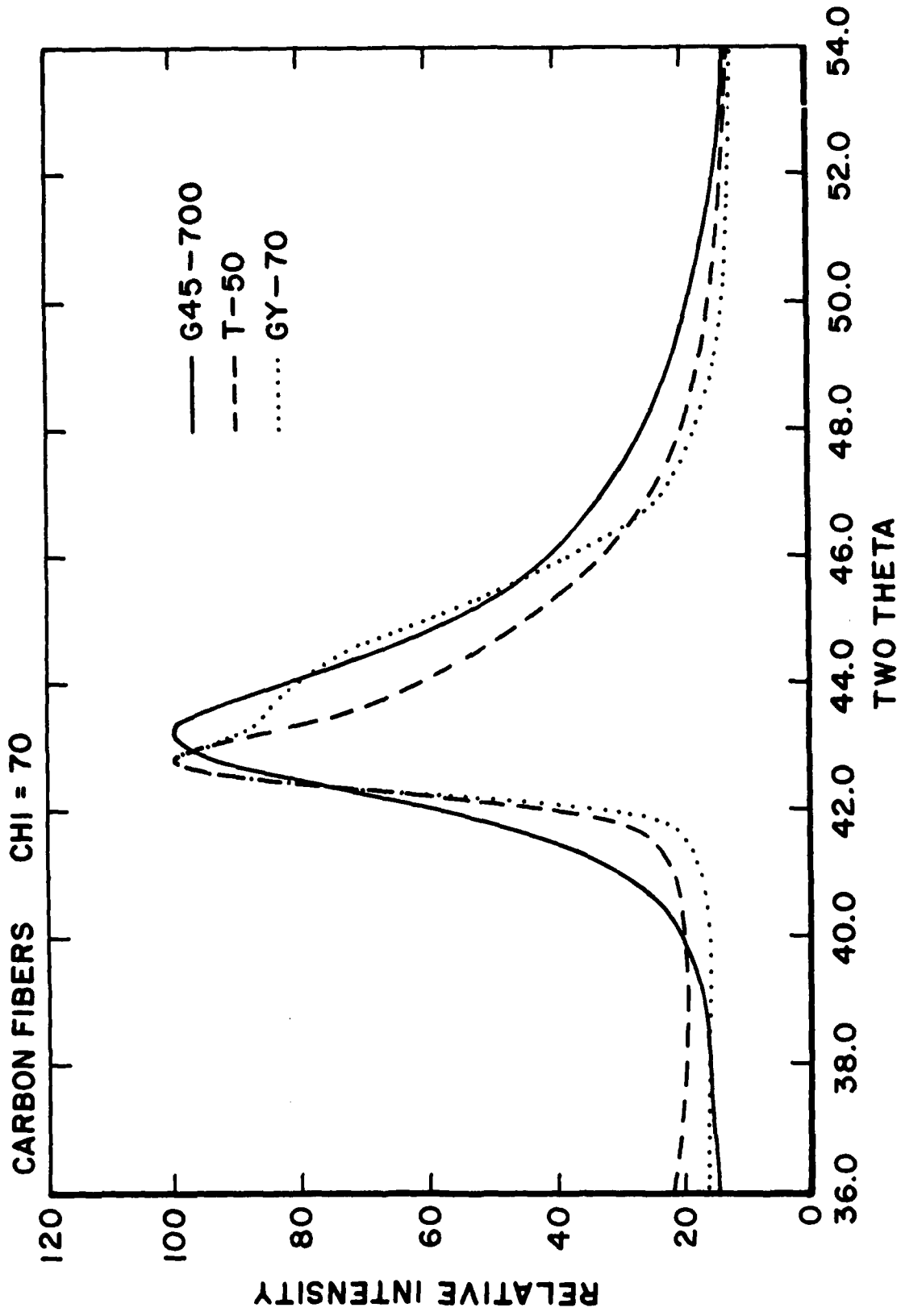


Figure 38. Bragg Scan of  $(10,1)$  Region in Some PAN-Based Fibers.

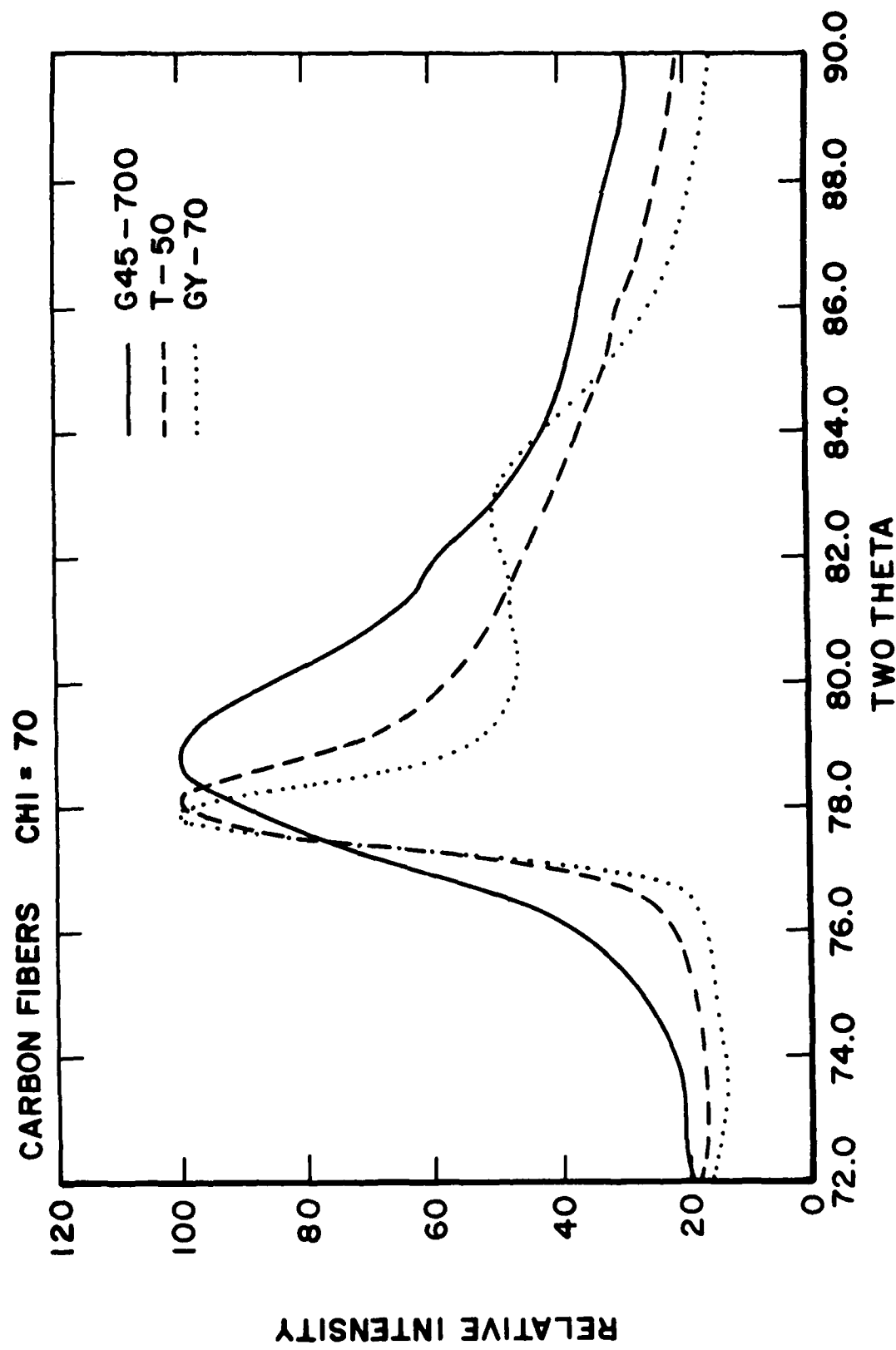


Figure 39. Bragg Scan of (11,2) Region in Some PAN-Based Fibers.

the next lower modulus pairs of P-55 and T-50. Claiming partial 3-D crystals from this data alone is definitely unwarranted. The fact that each series peak maxima coincide precisely for P-55 and P-75, and T-50 and GY-70 but not with the lower modulus fiber, supports the claim of some 3-D crystals. Returning to Table 5, note that the (10) reflection yields larger  $L_a$  values than the (11) reflection for both of those fibers. This is true for other fibers as well, as seen in Table 6 ( $L_a$  values calculated using equation 6) except in the cases of known or surmised 3-D crystals.

Three-dimensional crystals have been reported for both Pitch and PAN-based carbon fibers [34] but only at moduli at or greater than 100 MsI. The observation of 3-D crystals at lower moduli in this study is a direct result of the use of the tilted fiber technique.

Table 6 should have been the last word on  $L_a$  values here but for the 3-D crystal problem and the truncation in  $2\theta$  of the (hk) patterns as shown in Figure 19. This truncation reduces the breadth of the diffraction peak resulting in a higher value  $L_a$  although the complete lack of (hk,l) interference is helpful. These crystals should be larger as measured at the  $\chi=90^\circ$  compared to  $\chi=70^\circ$  leading to the conclusion that the last two columns in Table 6 should be considered as maximum limiting values.

If one assumes that when the value of  $L_a$  at  $\chi=70^\circ$  from (10) falls near or below the value from (11) this is an indication of 3-D crystals developing (two paragraphs above), then the suspected samples with 3-D crystals in the last paragraph are confirmed. This point also coincides with a large deviation in measured  $L_a$  between  $\chi=90^\circ$  and  $\chi=70^\circ$ , but that may be fortuitous. Table 7 lists the fibers and whether they contain 2-D crystals only, some 3-D crystals, or suspected 3-D crystals.

TABLE 6  
SUMMARY OF (hk) WAXD CRYSTAL PLANE SIZES ( $L_a$  IN ANGSTROMS)

<u>Fiber</u>	Chi = 70°		Chi = 90°	
	(10)	(11)	(10)	(11)
<u>Pitch-Based</u>				
P-25	51	40	49	43
P-55	83	111	236	201
P-75	64	172	265	276
P-100	na <sup>a</sup>	306	328	372
P-120	na <sup>a</sup>	327	379	395
<u>PAN-Based</u>				
T-300	43	37	46	36
AS4	43	31	47	39
T-40	44	34	54	38
G40-700	64	49	75	62
IM6	na <sup>b</sup>	na <sup>b</sup>	58	52
G45-700	61	45	77	61
HMS	143	96	181	171
T-50	91	88	177	165
GY-70	62	153	265	293
<u>Vapor Grown</u>				
Applied Sciences	338	394	333	395

na - Not available

a - (10,1) obviously dominating the scan area

b - Bragg scan not obtained

TABLE 7  
SUMMARY OF CARBON FIBER 2-D AND 3-D CRYSTAL CONTENT

<u>Fiber</u>	<u>2-D Crystals Only</u>	3-D Crystals	
		<u>Suspected</u>	<u>Definite</u>
<u>Pitch-Based</u>			
P-25	X	-	-
P-55	-	X	-
P-75	-	-	X
P-100	-	-	X
P-120	-	-	X
DuPont	-	-	X
<u>PAN-Based</u>			
T-300	X	-	-
AS4	X	-	-
T-40	X	-	-
G40-700	X	-	-
IM6	X	-	-
G45-700	X	-	-
HMS	X	-	-
T-50	-	X	-
GY-70	-	-	X
<u>Vapor Grown</u>			
Applied Sciences	-	-	X

#### 4.5 OTHER

In Figure 5 the diffraction of P-100 (and P-120 from Appendix A) shows satellite intensity of the (10,1) reflection at the 60° positions relative to the main intensity at chi=90°. The source of these peaks is obviously from flattened graphitic bundles with sufficiently large flat regions to allow diffraction from the equivalent (hk,l) crystal planes of the reflection generating the main peak. Preferred orientation of the large bundles is also necessary, since with random orientation of the a-axis and flattening of the bundles, a ring should develop as those equivalent crystal planes would also be random (see section 3.1). Because satellite peaks have developed only at specific locations around the ring area, only those sheet bundles properly oriented can flatten out during the general crystal orientation and perfecting processing.

Additional data, including (11,2) orientation, is required to properly interpret these hints of structure in highly oriented, high modulus carbon fibers.

## 5. CONCLUSIONS

The general crystalline structure of Pitch- and PAN-based carbon fibers is roughly equivalent for fibers of approximately the same tensile modulus. The major structural changes occur in fibers of 50-60 Ms<sup>i</sup> modulus, with the PAN-based fibers lagging behind the Pitch-based fibers only slightly in terms of structure versus modulus development. Some of the major differences between these two classes of fibers is due more to the difficulty of processing to achieve PAN-based fibers with sufficiently high modulus to compare with common Pitch-based fibers than any inherent structural differences.

The large strength differences in these classes of fibers are apparently not directly related to the crystal sizes and average orientation of those crystals. Internal crystal arrangement and gross flaws, which are not detectable in WAXD measurements on neat fibers, may be responsible for the strength characteristics.

## REFERENCES

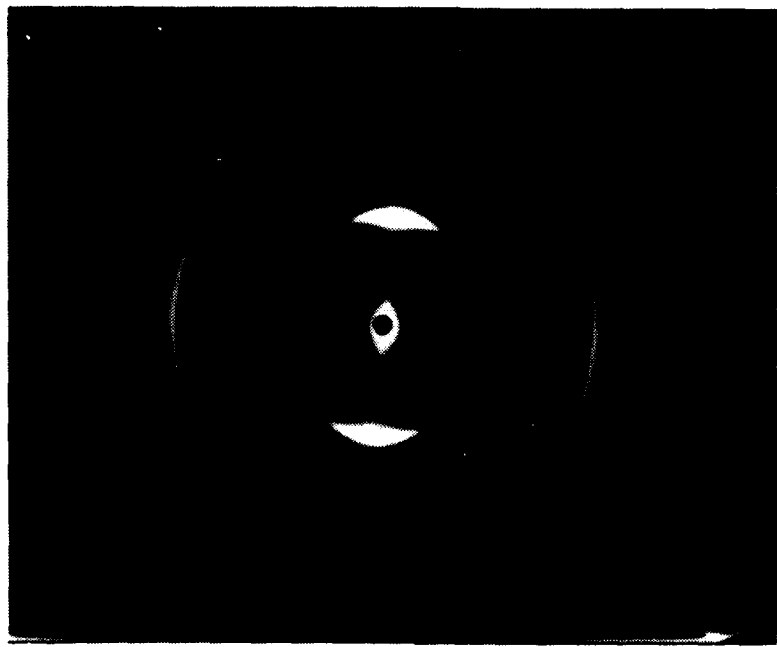
1. A. Fourdeux, C. Herinckx, R. Perret, and W. Ruland, Translated Title: "Physical Chemistry - The Structure of Carbon Fiber," C. R. Acad. Sci., 269, 1597 (1969).
2. R. Perret and W. Ruland, "The Microstructure of PAN-Base Carbon Fibres," J. Appl. Cryst., 3, 525 (1970).
3. A. Fourdeux, R. Perret, and W. Ruland, Proc. First Int. Conf. on Carbon Fibers, London, Plastics Inst. (1971).
4. J. V. Larsen and T. G. Smith, "Carbon Fiber Structure," NOLTR 71-166, Naval Ordnance Laboratory, White Oak, Silver Spring, MD, October 1971.
5. R. Bacon, "Carbon Fibers from Rayon Precursors," in Chemistry and Physics of Carbon: A Series of Advances, Vol. 9 (1973), P. L. Walker Jr. and Peter A. Thrower, Eds., Marcel Dekker, Inc., New York.
6. F. R. Barnet and M. K. Noor, Proc. Second Int. Conf. on Carbon Fibers, London, Plastics Inst. (1974).
7. F. R. Barnet and M. K. Noor, "A Three-Dimensional Structural Model for a High Modulus PAN-Based Carbon Fiber," NOLTR 73-154, Naval Ordnance Laboratory, White Oak, Silver Spring, MD, June 1974.
8. R. J. Diefendorf and E. W. Tokarsky, "High-Performance Carbon Fibers," Polymer Eng. Sci., 15, 150 (1975).
9. S. C. Bennett, D. J. Johnson, and R. Murray, "Structural Characterization of a High-Modulus Carbon Fibre by High-Resolution Electron Microscopy and Electron Diffraction," Carbon, 14, 117 (1976).
10. S. C. Bennett and D. J. Johnson, "Electron-Microscope Studies of Structural Heterogeneity in PAN-Based Carbon Fibers," Carbon, 17, 25 (1979).
11. M. Guigon, A. Oberlin, and G. Desarmot, "Microtexture and Structure of Some High Tensile Strength, PAN-Base Carbon Fibres," Fibre Sci. Technol., 20, 55 (1984).
12. M. Guigon, A. Oberlin, and G. Desarmot, "Microtexture and Structure of Some High-Modulus, PAN-Base Carbon Fibres," Fibre Sci. Technol., 20, 177 (1984).
13. M. Guigon and A. Oberlin, "Heat-Treatment of High Tensile Strength PAN-Based Carbon Fibres: Microtexture, Structure and Mechanical Properties," Compos. Sci. Technol., 27, 1 (1986).

14. B. E. Warren and P. Bodenstein, "The Shape of Two-Dimensional Carbon Black Reflections," Acta Cryst., 20, 602 (1966).
15. L. E. Alexander, X-Ray Diffraction Methods in Polymer Science, Wiley-Interscience, New York, 1969.
16. A. Fourdeux, R. Perret, and W. Ruland, "The Effect of Preferred Orientation on (hk) Interferences as Shown by Electron Diffraction of Carbon Fibres," J. Appl. Cryst., 1, 252 (1968).
17. W. Ruland, "X-Ray Diffraction Studies on Carbon and Graphite," in Chemistry and Physics of Carbon: A Series of Advances, Vol. 4 (1968), Philip L. Walker Jr., Ed., Marcel Dekker, Inc., New York.
18. Joint Committee on Powder Diffraction Standards, "Graphite," JCPDS 23-64 (1973).
19. M. von Laue, Z. Kristallogr., 82, 127 (1932).
20. B. E. Warren, Phys. Rev., 59, 693 (1941).
21. A. J. C. Wilson, "X-Ray Diffraction by Random Layers: Ideal Line Profiles and Determination of Structure Amplitudes from Observed Line Profiles," Acta Cryst., 2, 245 (1949).
22. W. Ruland, "Fourier Transform Methods for Random-Layer Line Profiles," Acta Cryst., 22, 615 (1967).
23. W. Ruland and H. Tompa, "The Effect of Preferred Orientation on the Intensity Distribution of (hk) Interferences," Acta Cryst., A24, 93 (1968).
24. W. Braun and E. Fitzer, "A Modified Structural Model Describing the Interference-Function of Pyrolyzed Non-Graphitizing Carbon," Carbon, 16, 81, (1978).
25. P. Scherrer, Göttinger Nachrichten, 2, 98 (1918).
26. R. Bonart, R. Hosemann, and R. L. McCullough, Polymer, 4, 1 (1963).
27. D. R. Buchanan, R. I. McCullough and R. L. Miller, "Crystallite Size and Lattice Distortion Parameters from X-ray Line Broadening," Acta Cryst., 20, 922 (1966).
28. W. N. Reynolds and J. V. Sharp, "Crystal Shear Limit to Carbon Fibre Strength," Carbon, 12, 103 (1974).
29. J.-B. Donet and R. C. Bansal, Carbon Fibers, Marcel Dekker, Inc., New York, 1984, Chapter 2.

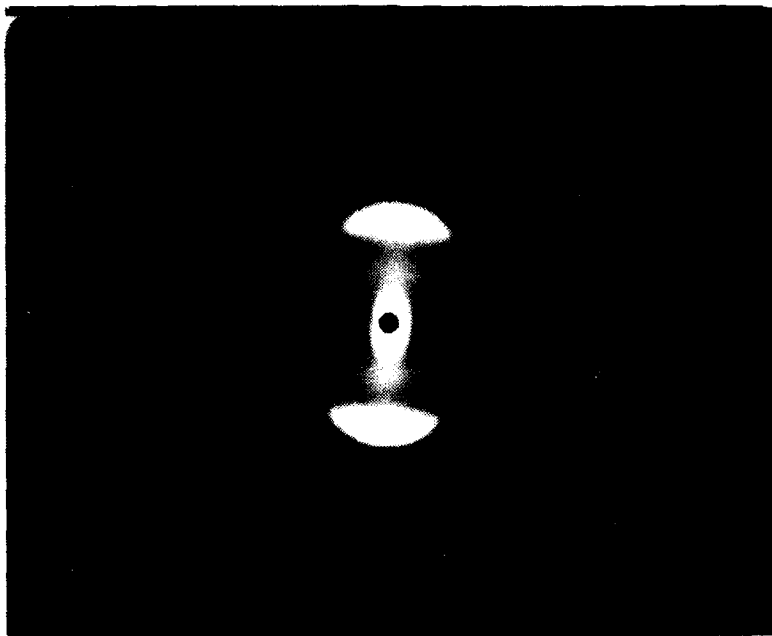
30. S. Kumar, W. W. Adams, and T. E. Helminiak, "Uniaxial Compressive Strength of High Modulus Fibers for Composites," J. Rein. Plast. Compos., 7, 108 (1988).
31. S. Kumar, "Structure and Properties of High Performance Polymeric and Carbon Fibers - An Overview," Fiber Prod. Conf. Proc. (1988).
32. K. Strong, personal communications.
33. J. D. H. Hughes, "The Evaluation of Current Carbon Fibres," Phys. D: Appl. Phys., 20, 276 (1987).
34. M. S. Dresselhaus, G. Dresselhaus, K. Sugihara, I. L. Spain, and H. A. Goldberg, Graphite Fibers and Filaments, Springer-Verlag, New York, 1988, Chapt. 3.

**APPENDIX A**  
**FLAT-FILM WAXD PHOTOGRAPHS OF CARBON FIBERS**

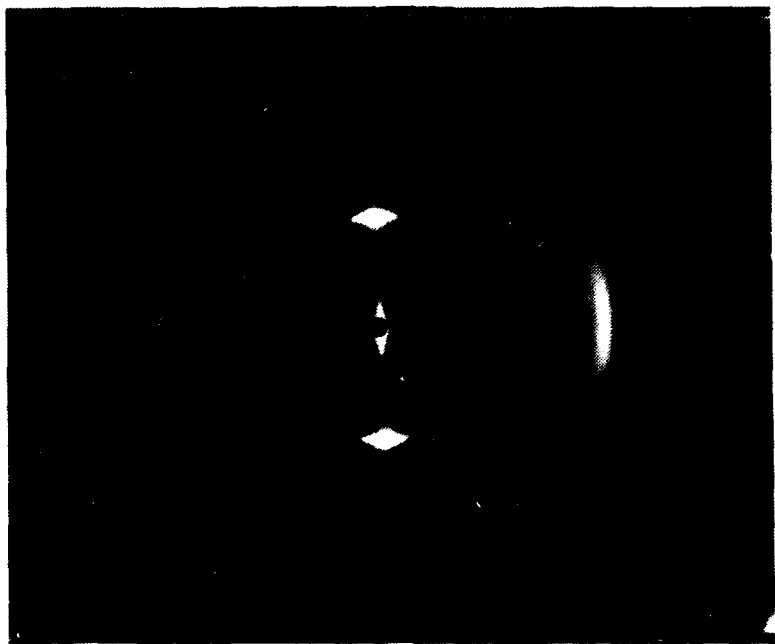
<u>Pitch</u>		<u>PAN</u>
P-25	T-300	G45-700
P-55	AS4	HMS
P-75	T-40	T-50
P-100	G40-700	GY-70
P-120	IM6	



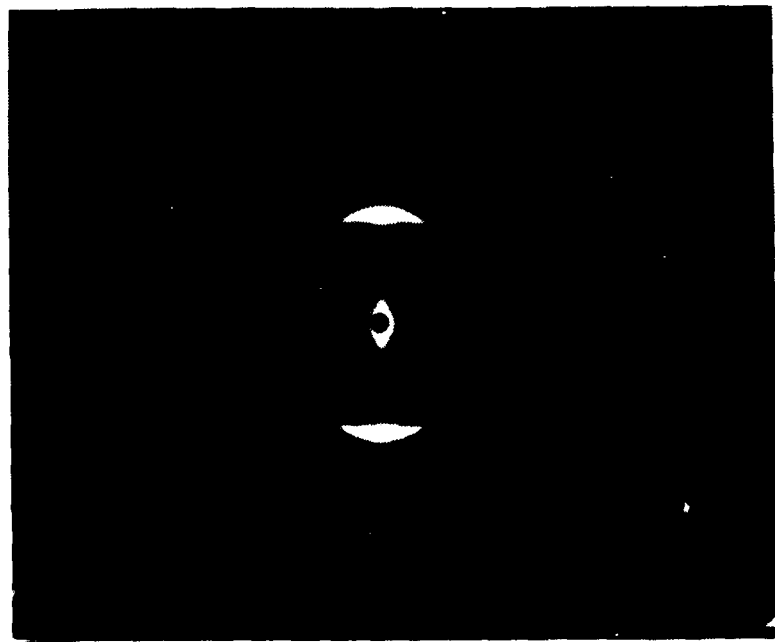
P-55



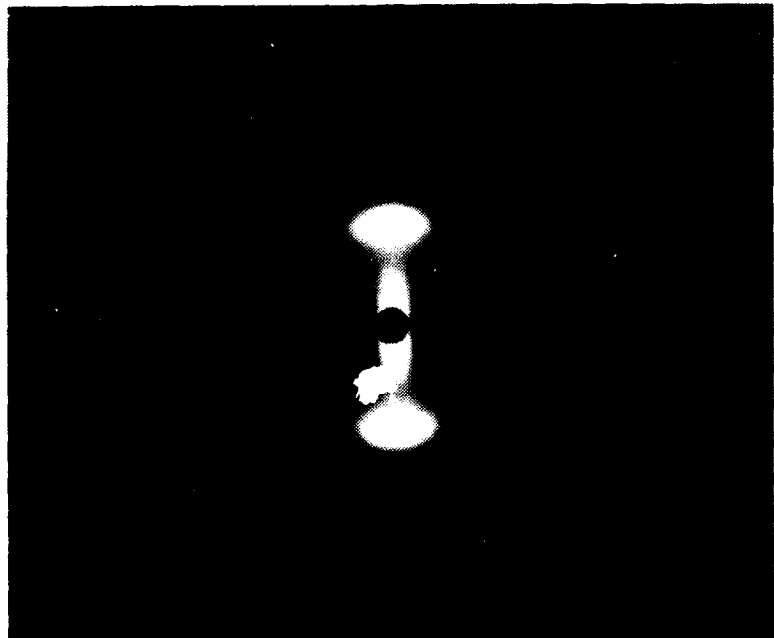
P-25



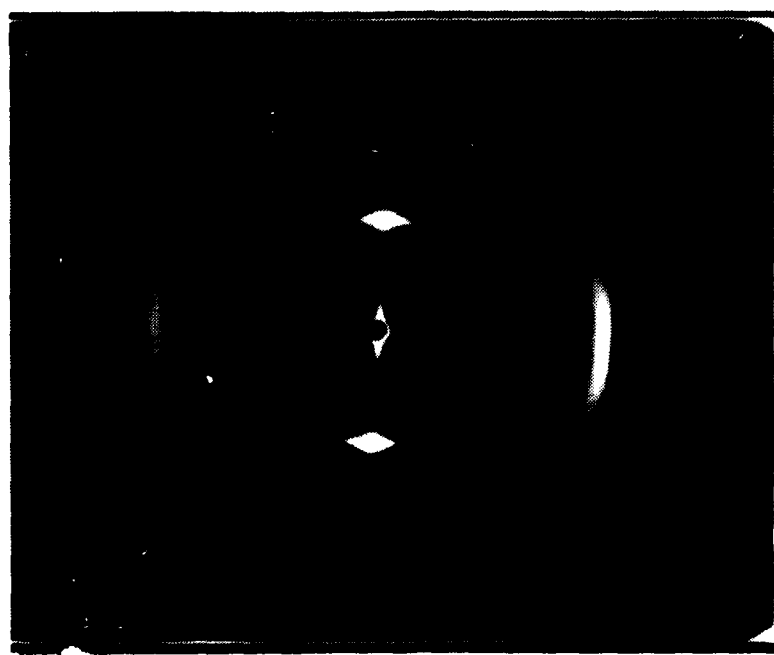
P-100



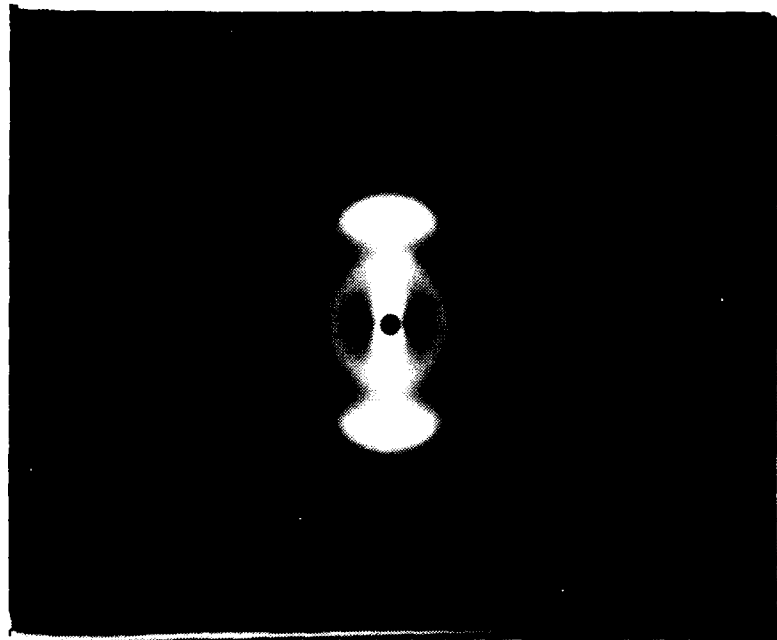
P-75



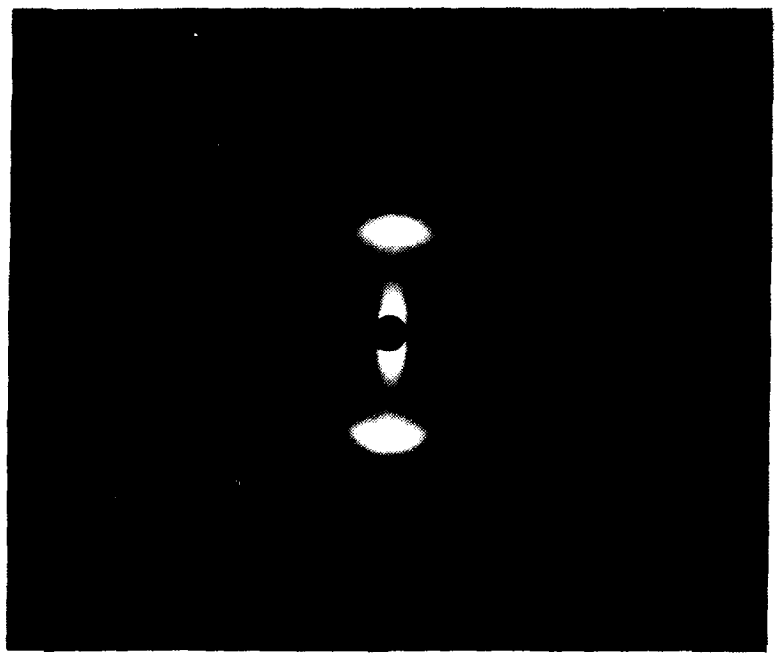
T-300



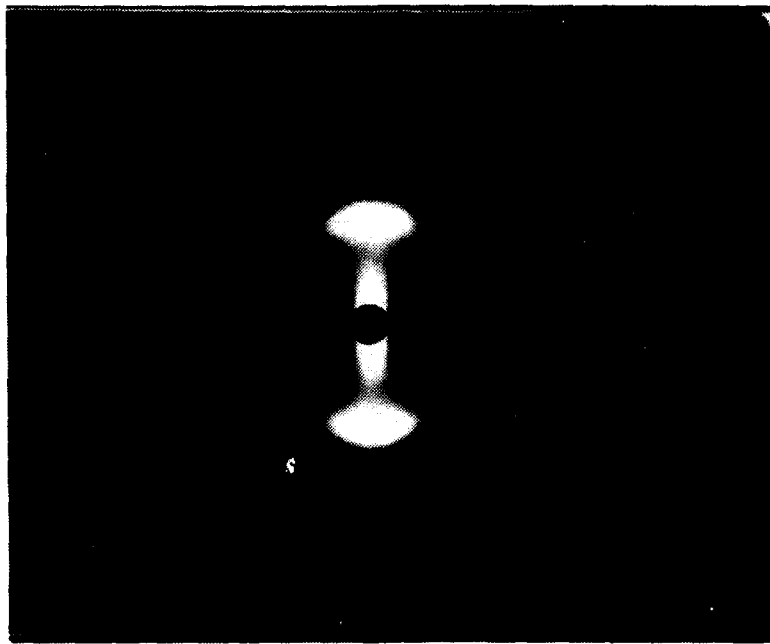
P-120



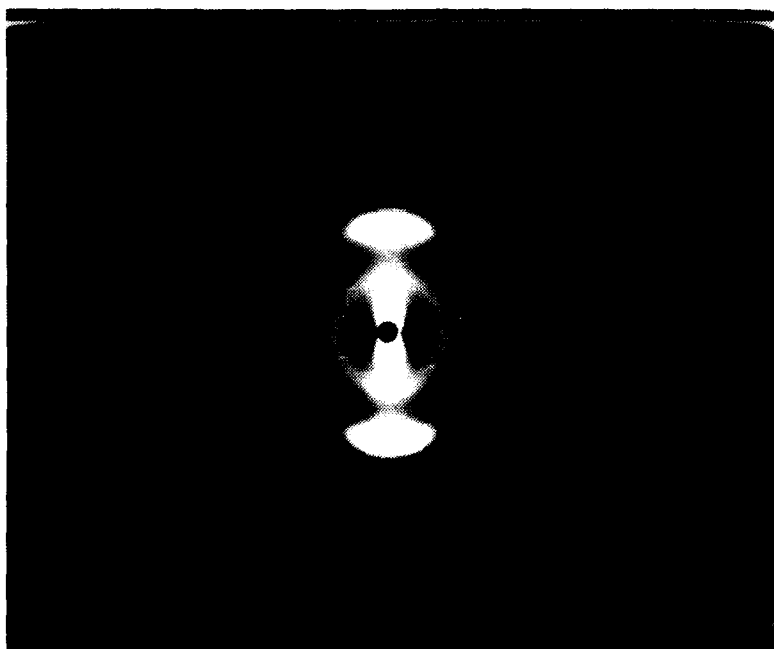
T-40



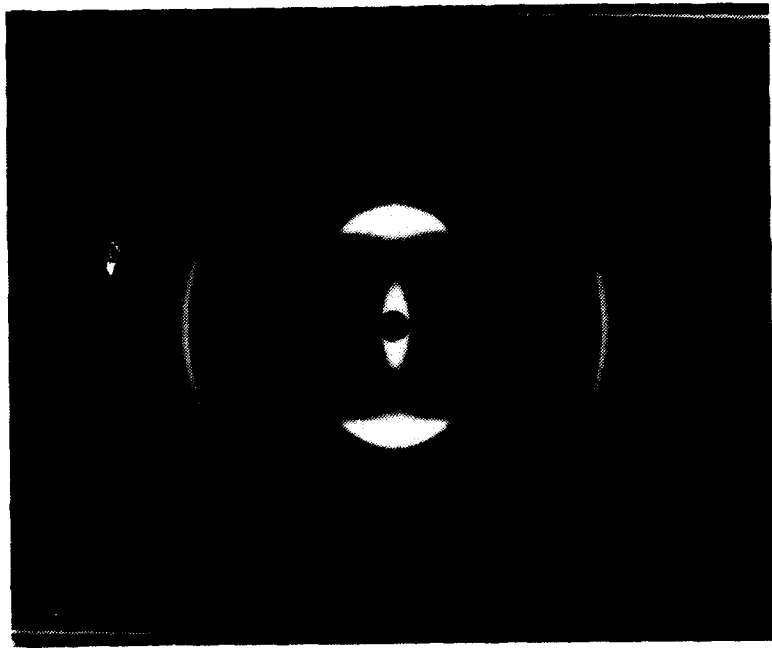
AS4



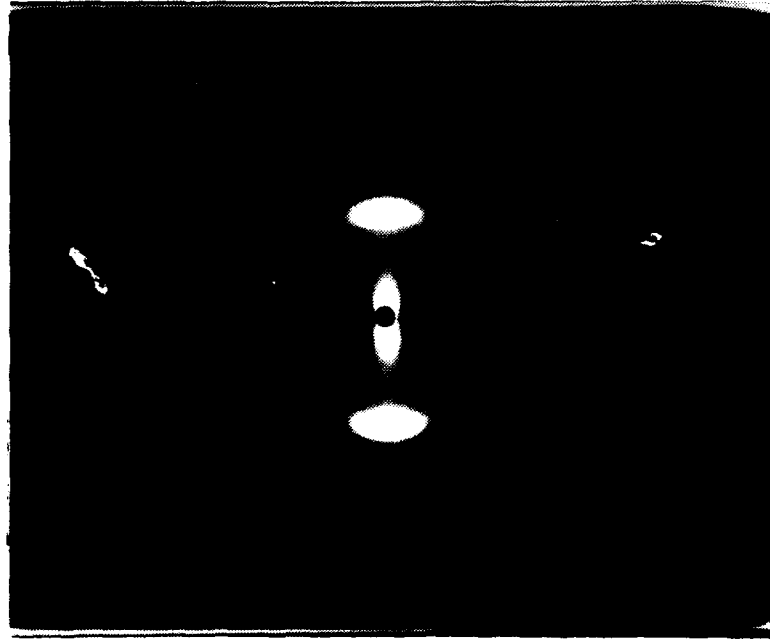
IMG



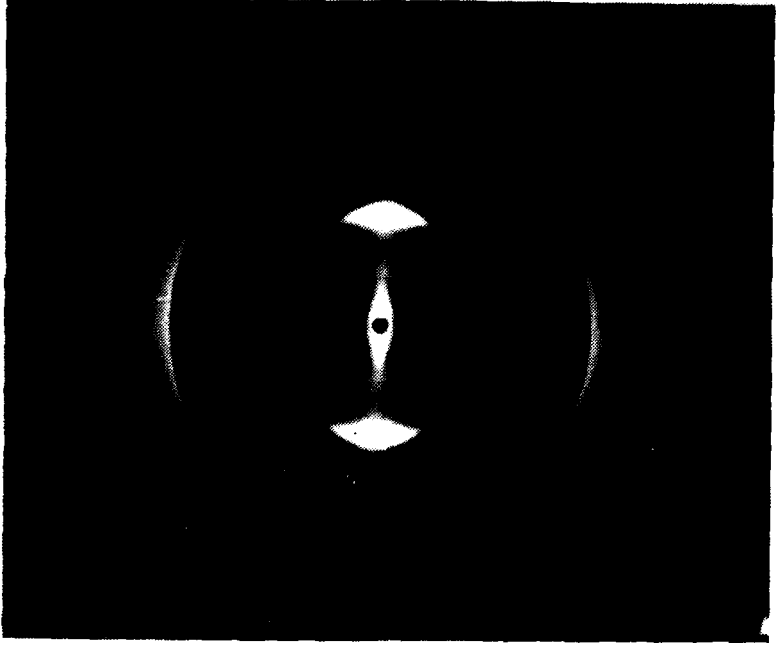
G40-700



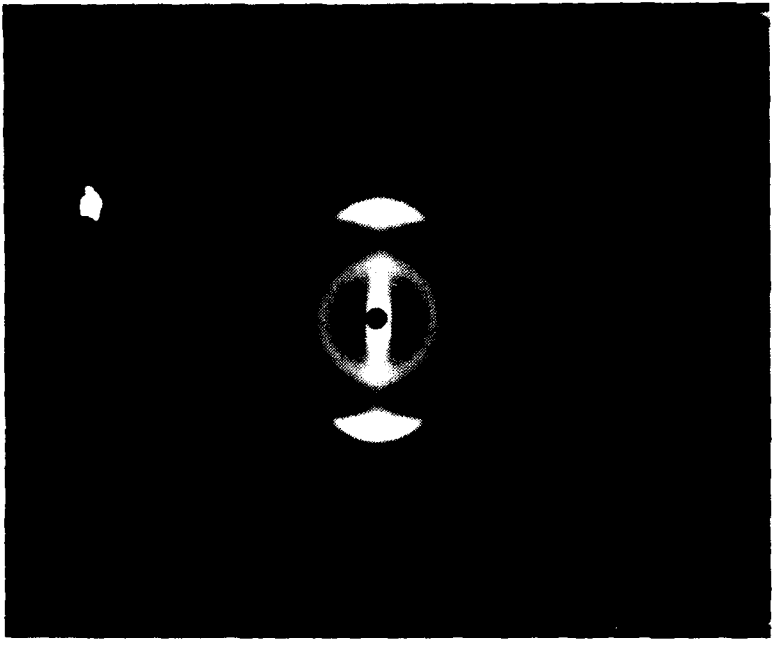
HMS



G45-700



GY-70

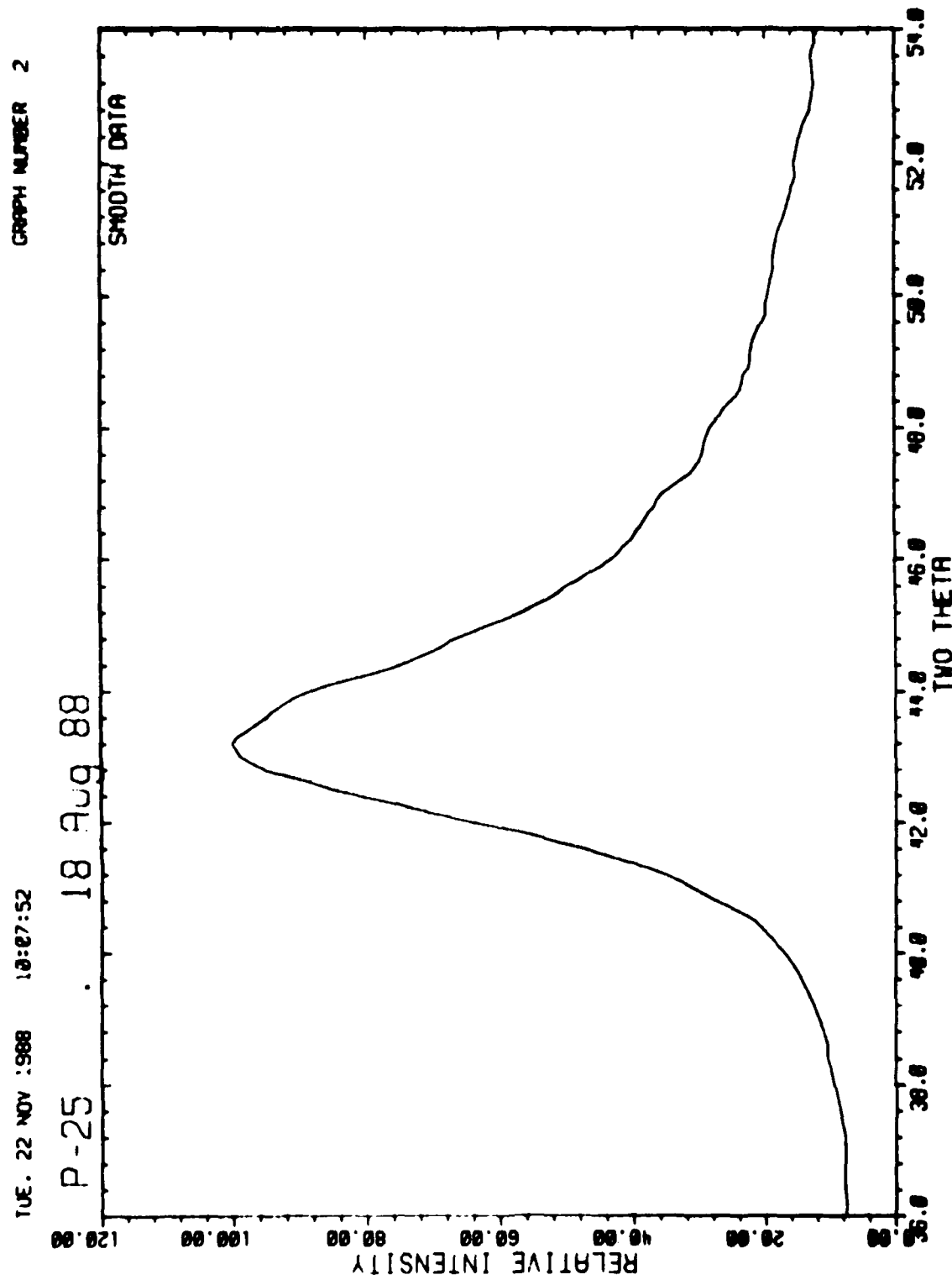


T-50

## APPENDIX B

DIFFRACTION SCANS (CHI=70°) OF THE (10) AND (10,1) REGION  
OF THE CARBON FIBERS

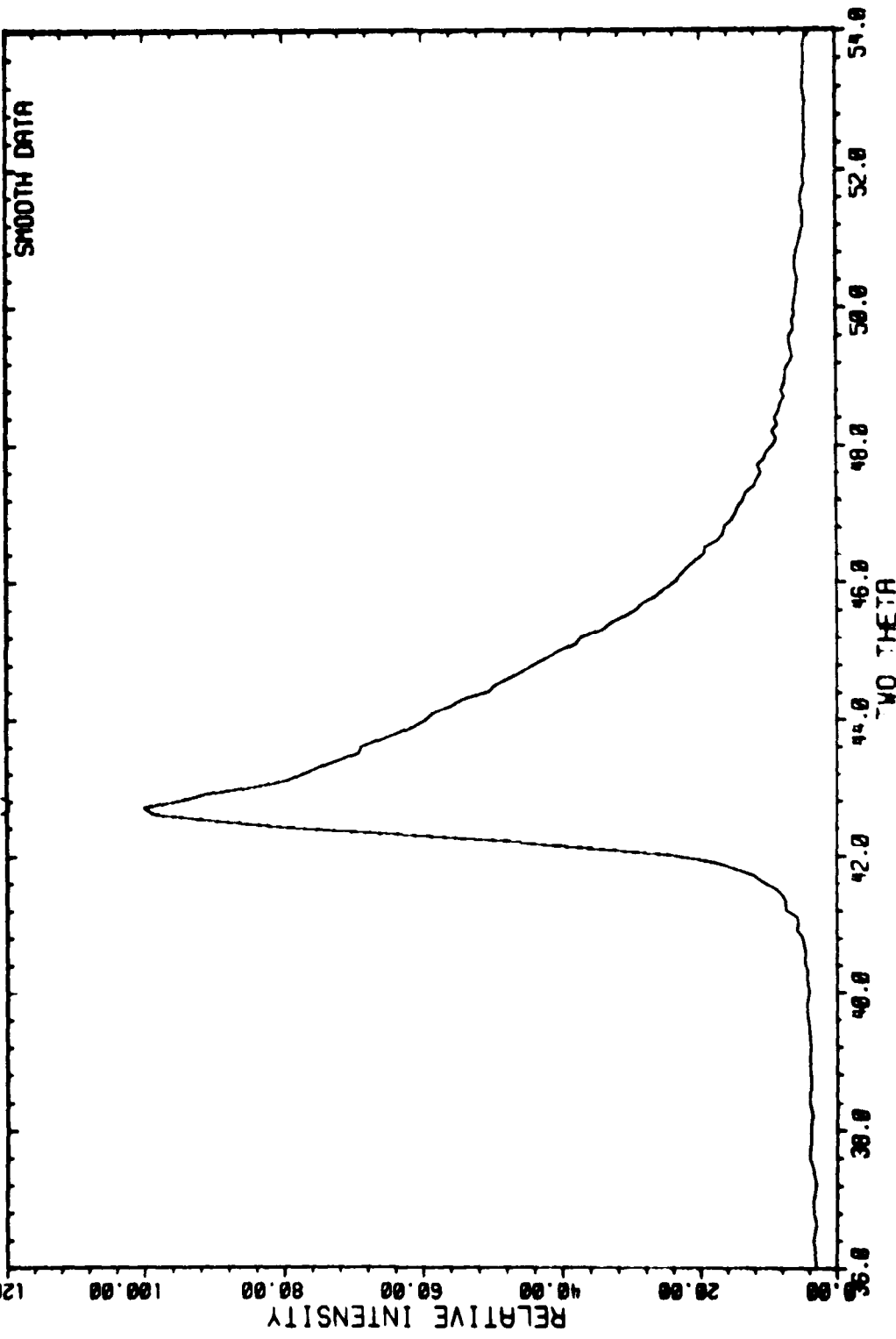
<u>Pitch</u>	<u>PAN</u>	<u>Vapor Grown</u>
P-25	T-300	G45-700 Applied Sciences
P-55	AS4	HMS
P-75	T-40	T-50
P-100	G40-700	GY-70
P-120		



GRAPH NUMBER 4

15. 22 NOV 1988 :0:12:8:

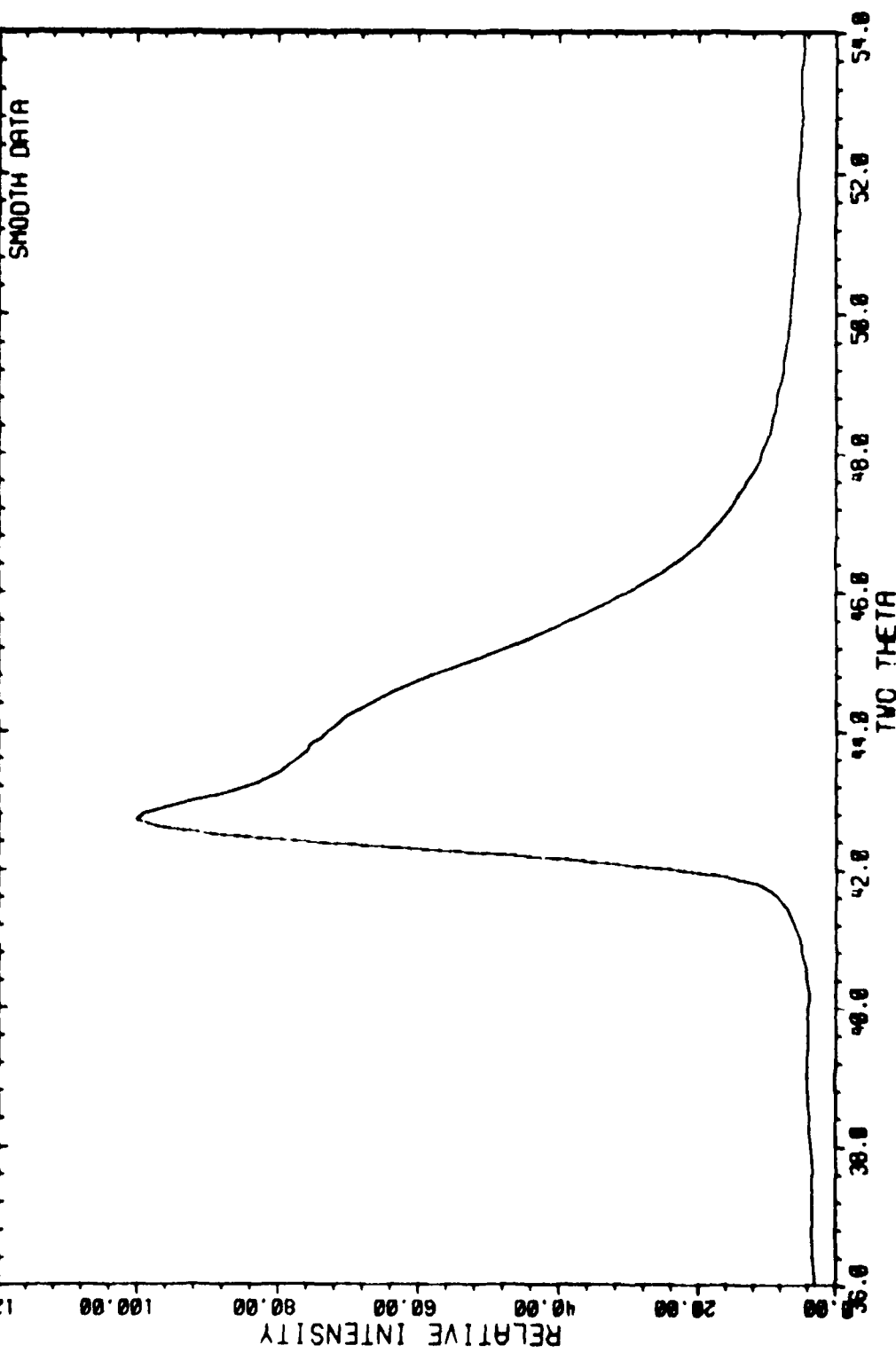
P-55 . 18 Aug 88



1.E. 22 NCV 1988 :02:13:58

P - 75

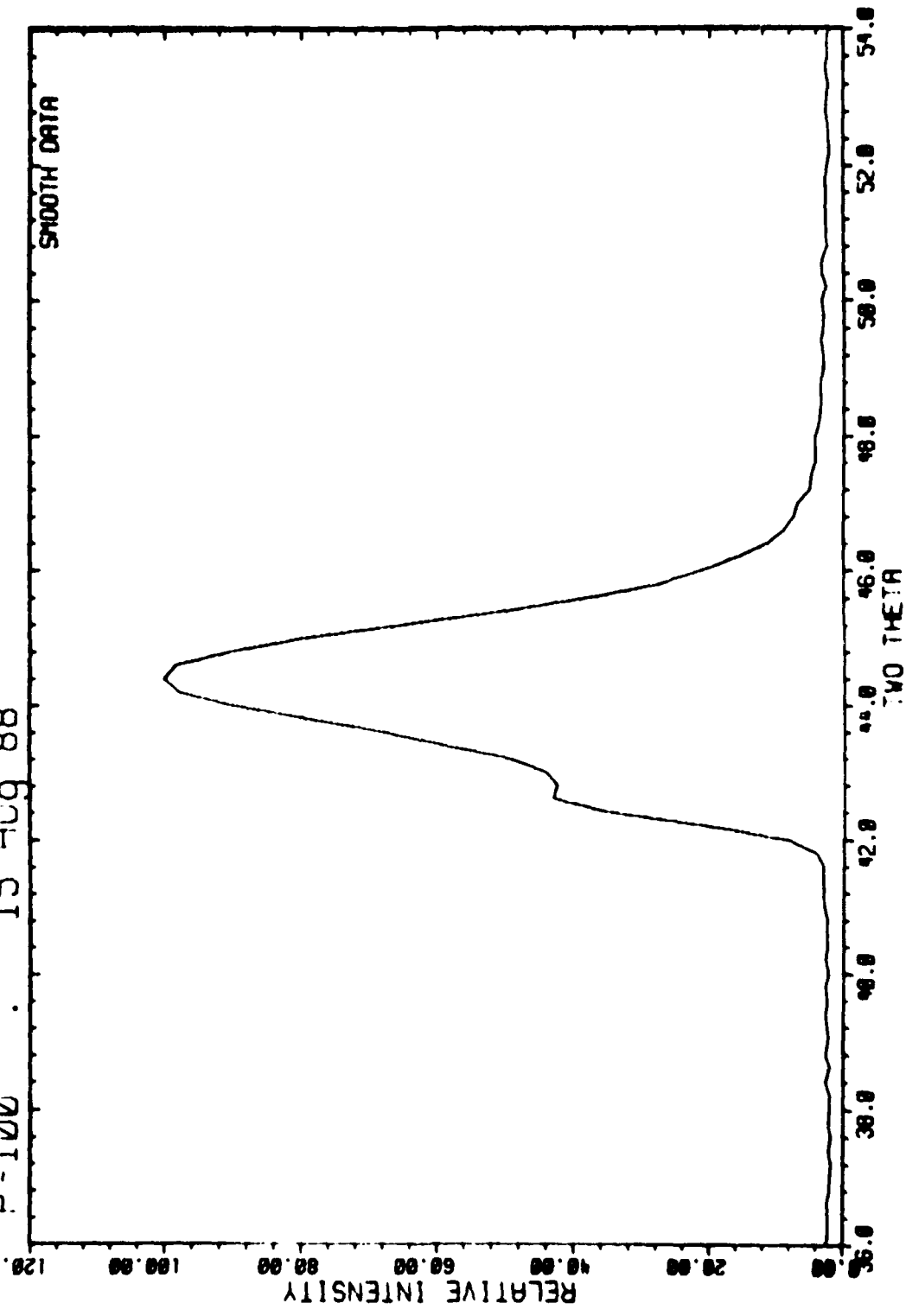
GRAPH NUMBER 8



UE. 22 NOV 1988 13:15:43

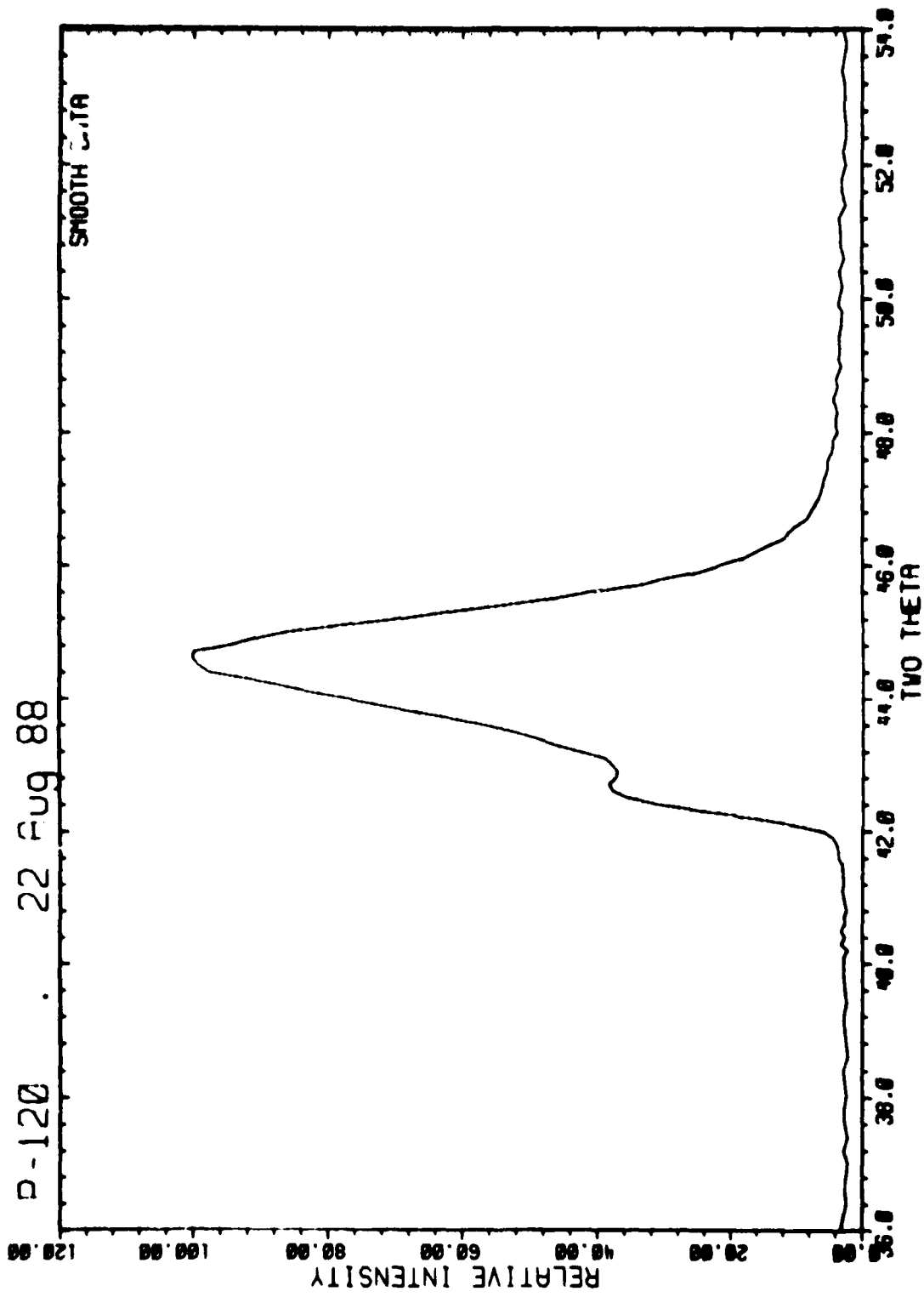
GRAPH NUMBER 10

P-100 . 15 Aug 88



TUE. 22 NOV 1988 :00:07:37

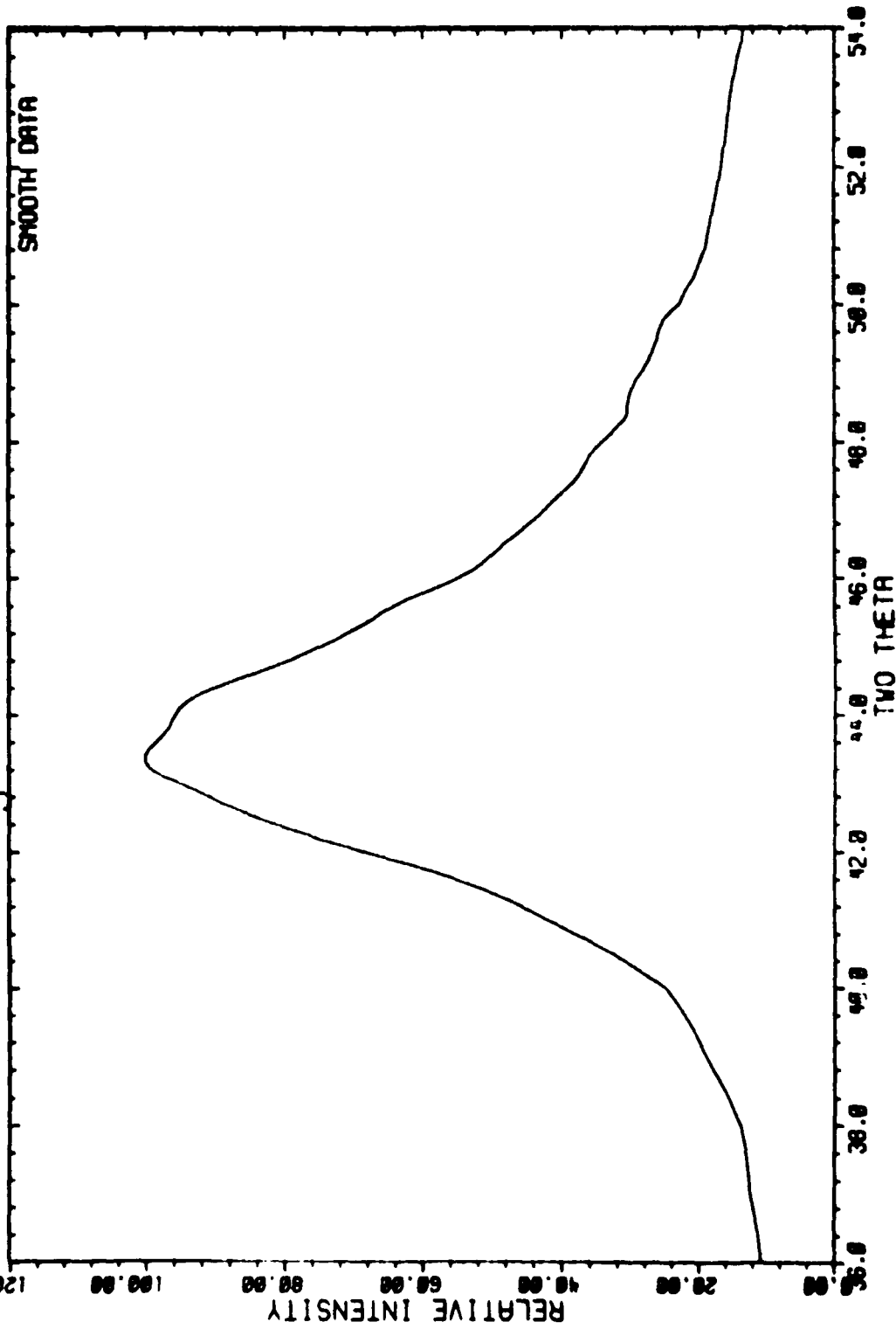
GRAPH NUMBER 12

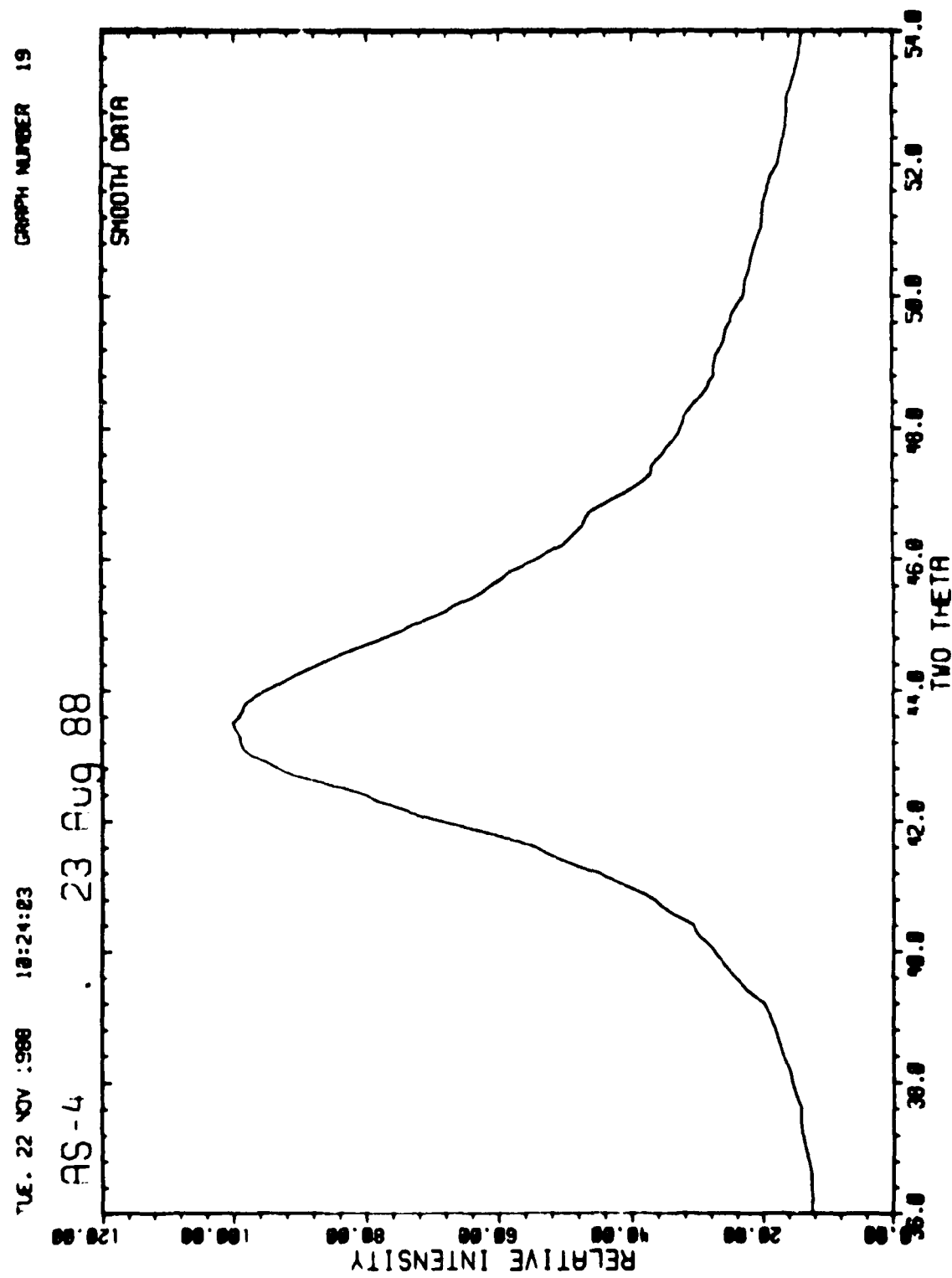


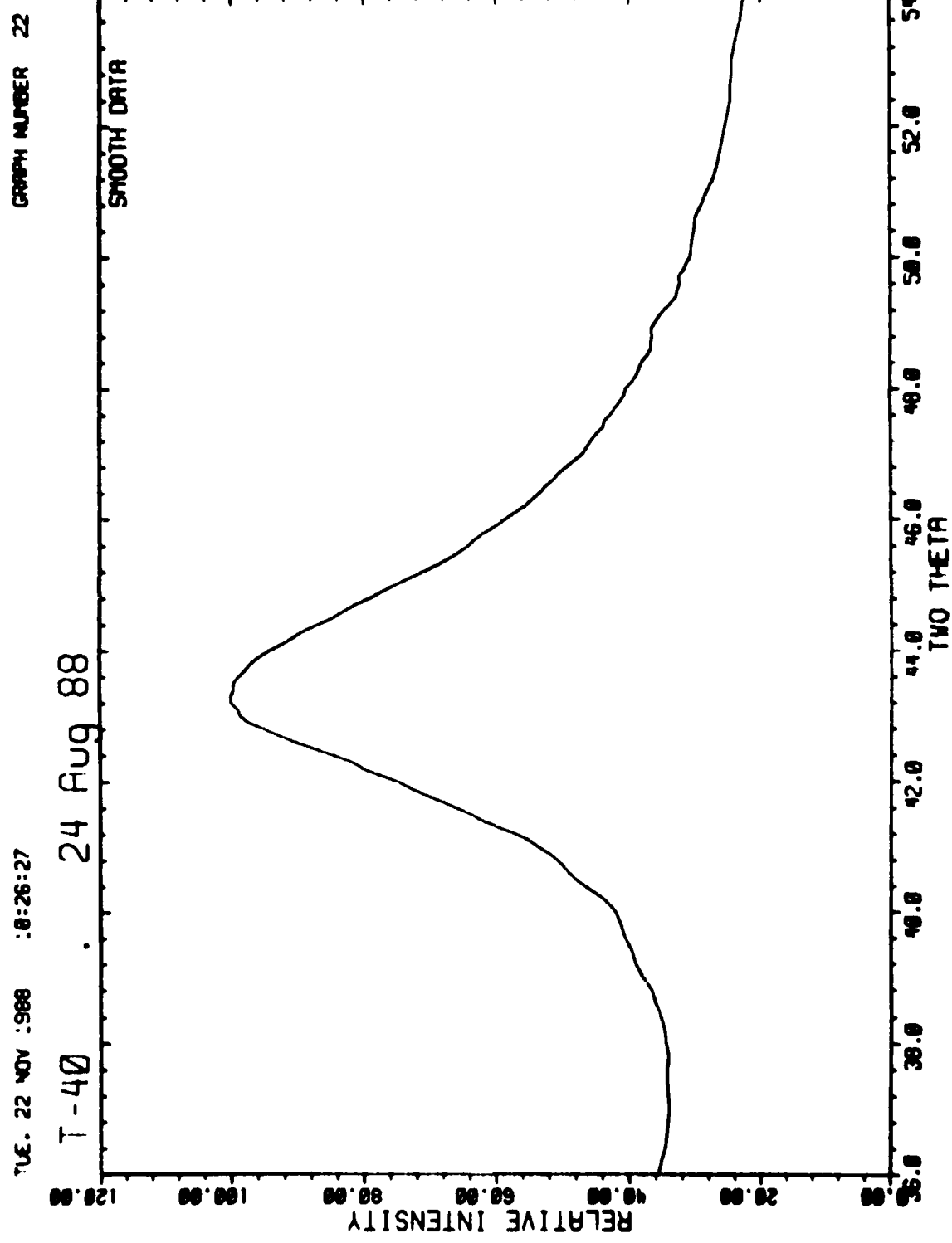
TUE. 22 NOV 1988 10:22:19

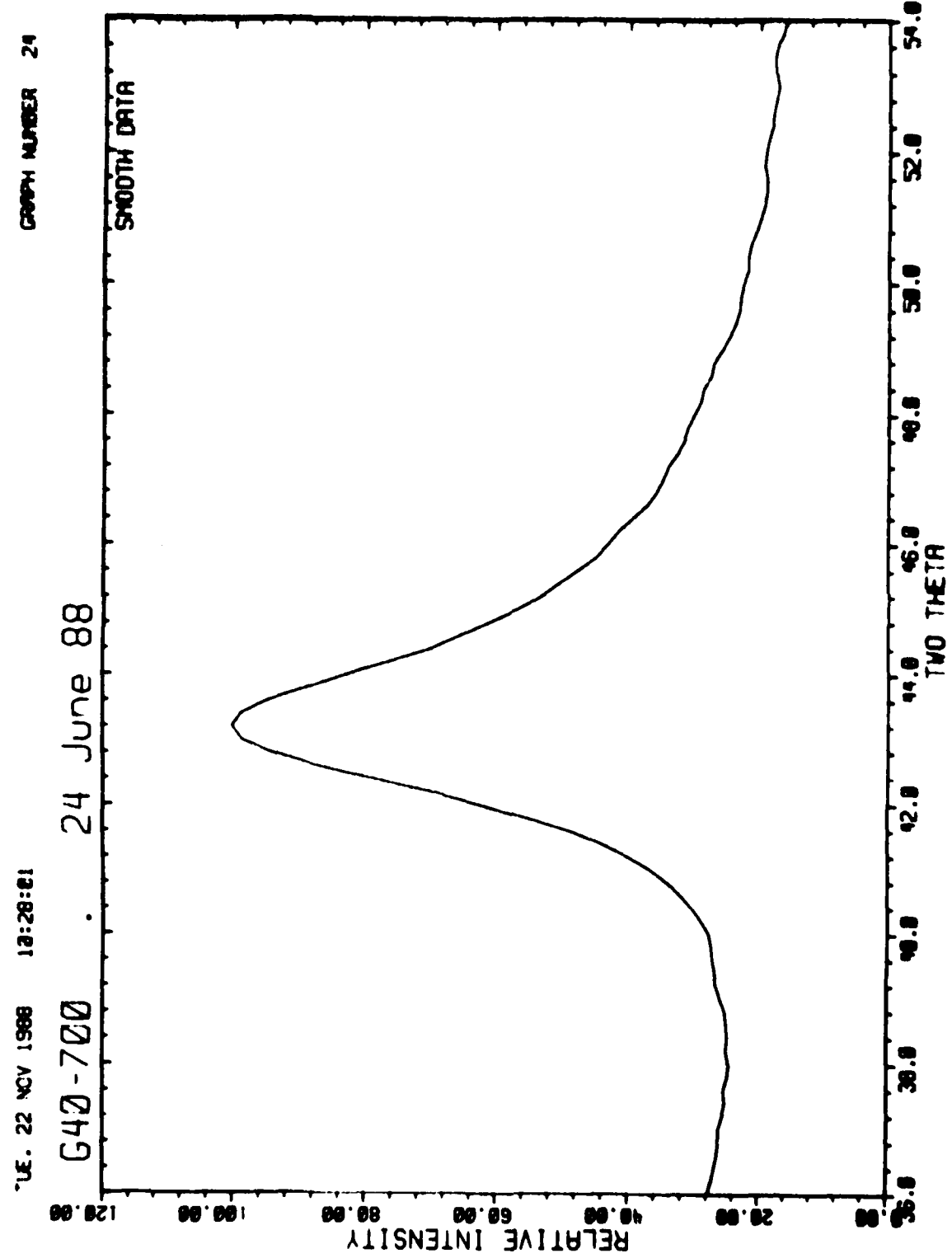
T - 300 . 19 Aug 88

GRAPH NUMBER 17





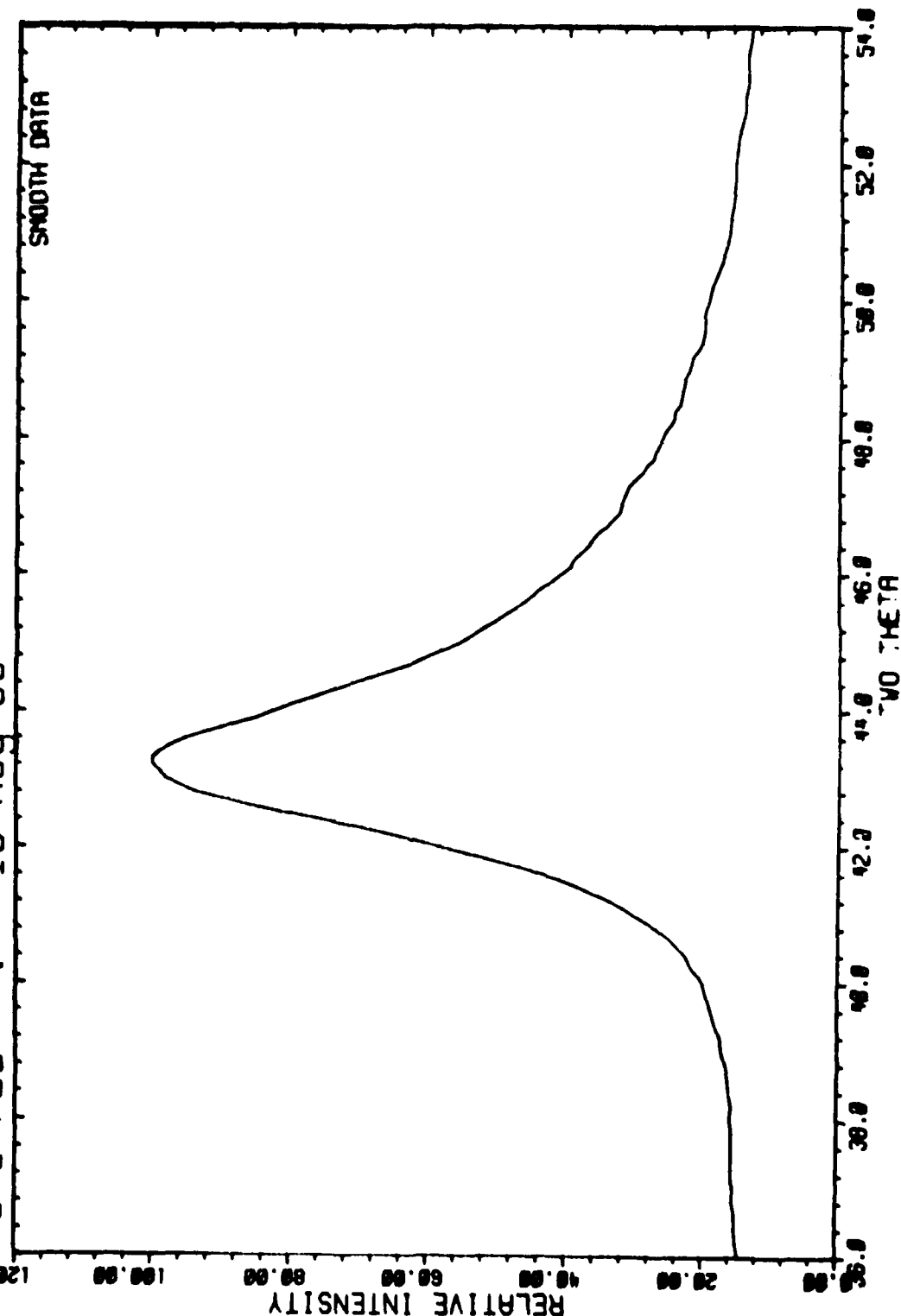


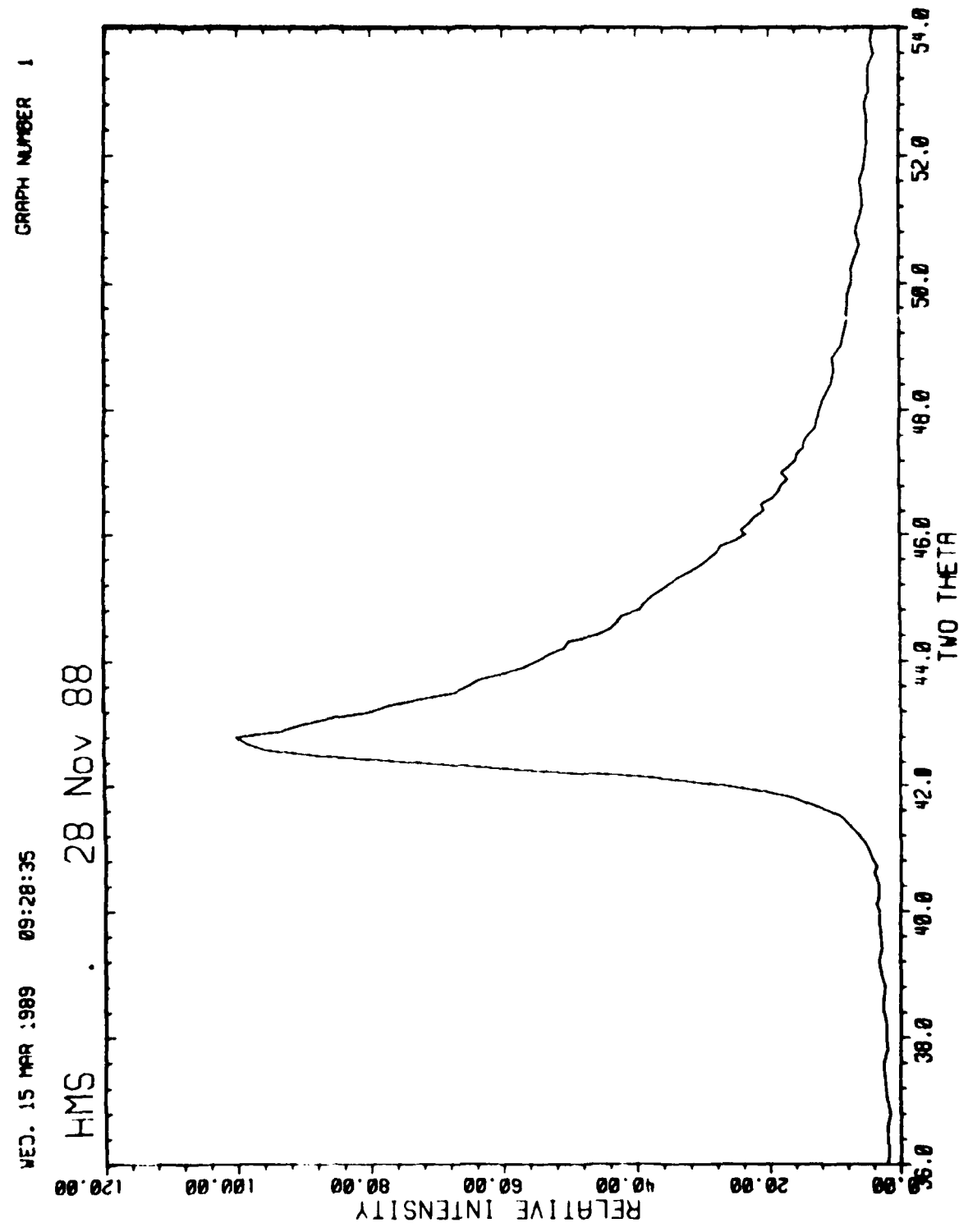


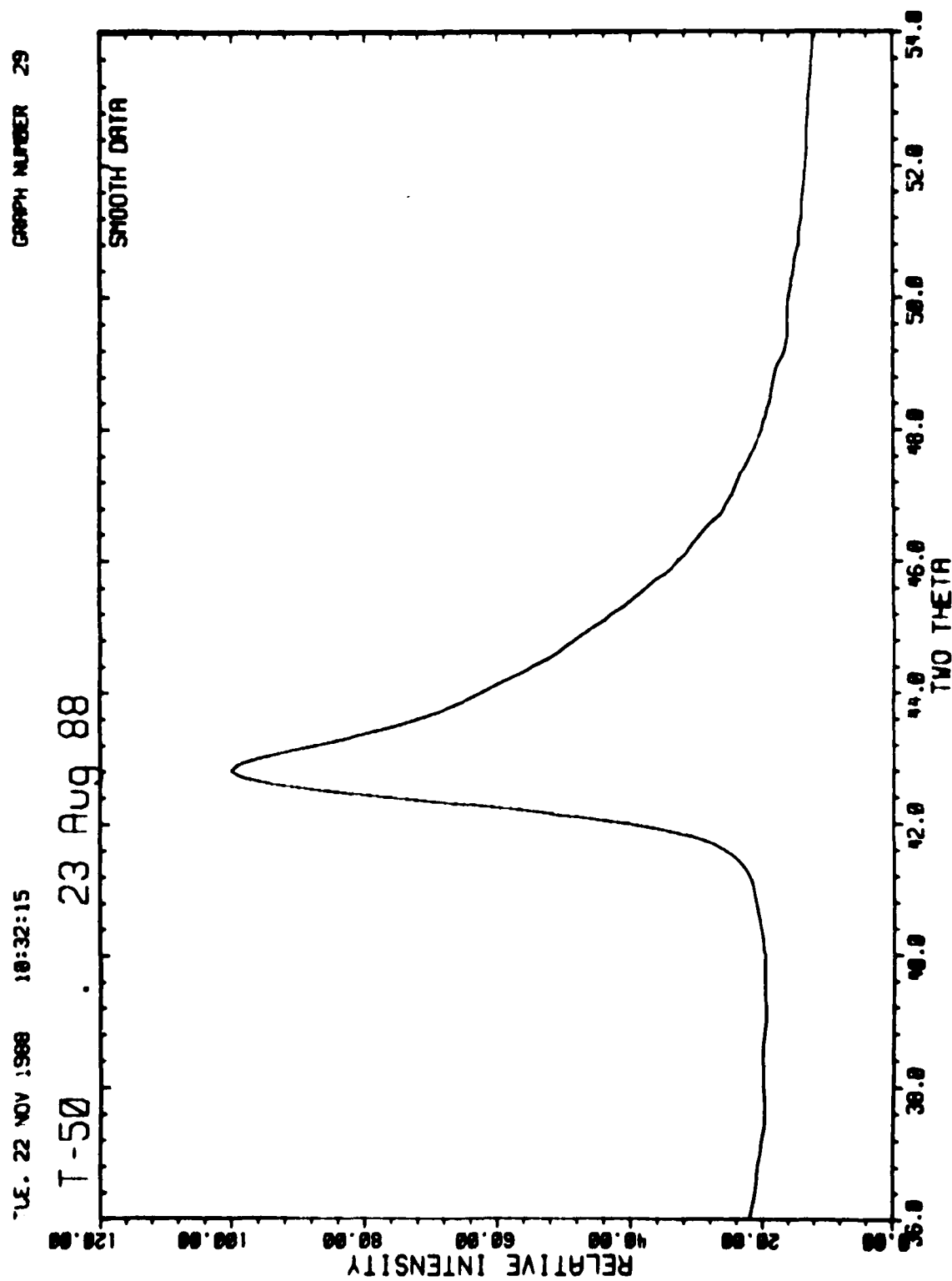
TUE. 22 NOV 1988 18:29:47

G45-700 . 19 Aug 88

GRAPH NUMBER 26



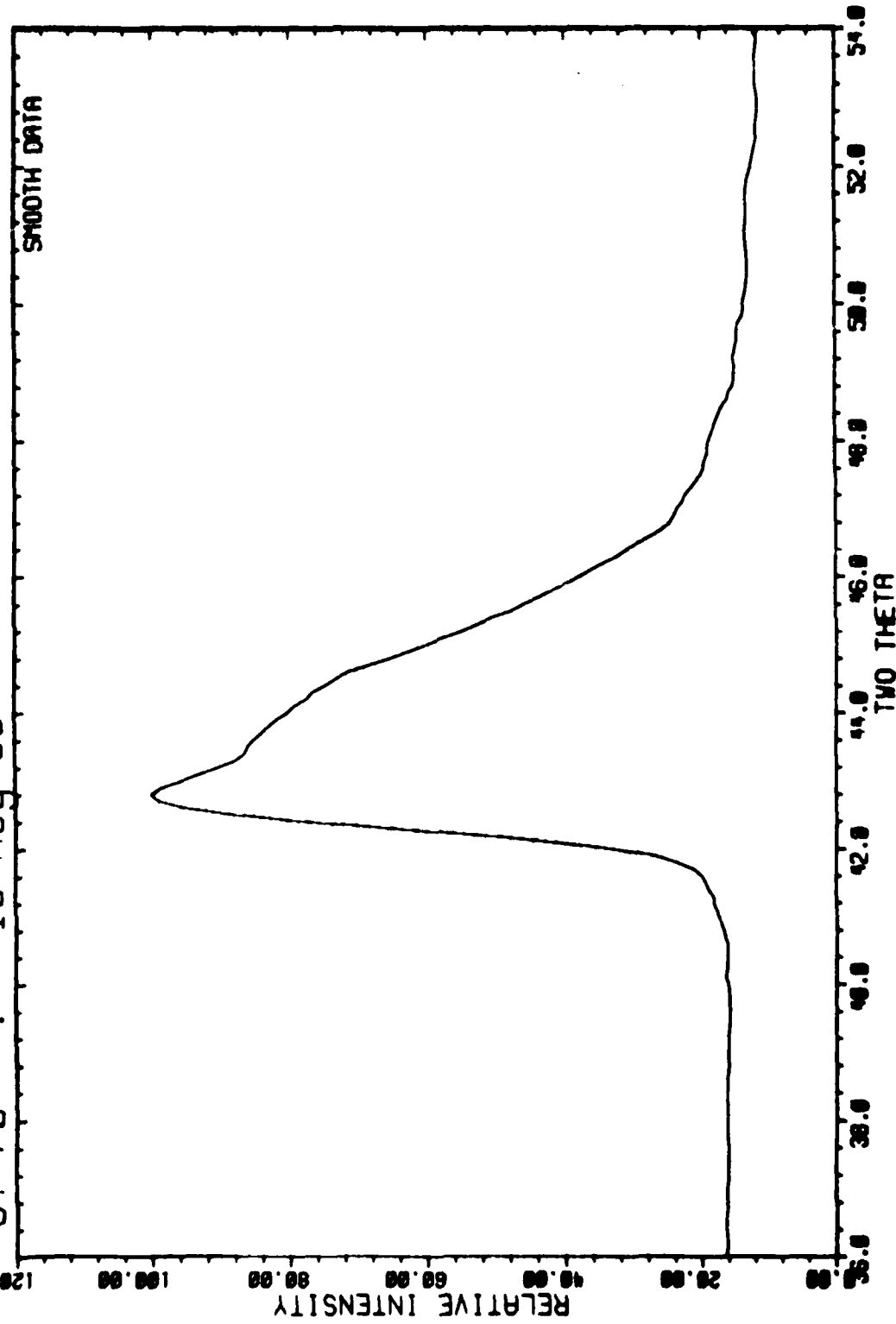


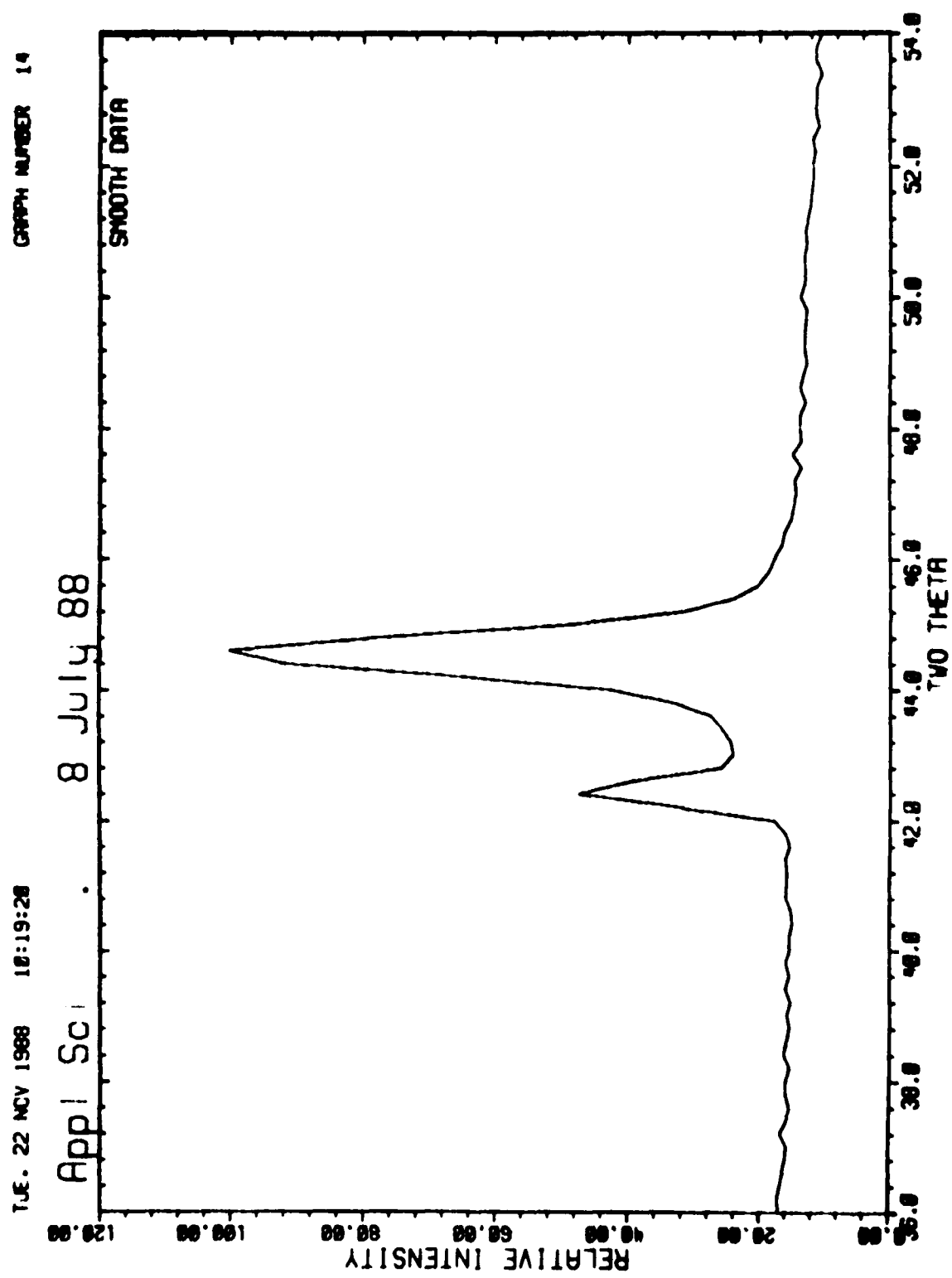


16. 22 Nov 1988 10:30:32

GY-70 . 16 Aug 88

GRAPH NUMBER 22

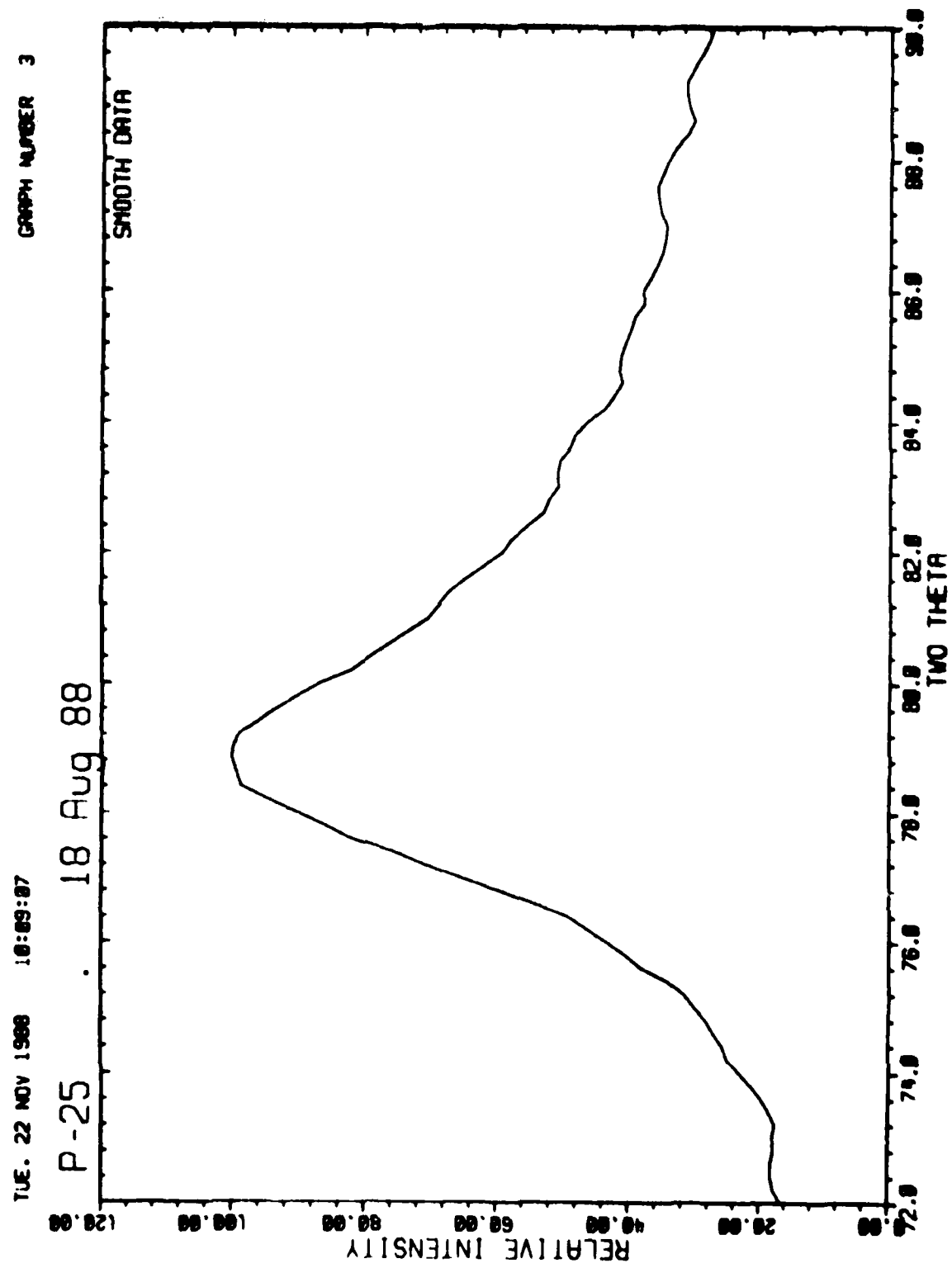




## APPENDIX C

DIFFRACTION SCANS (CHI=70°) OF THE (11) AND (11,2) REGION  
OF THE CARBON FIBERS

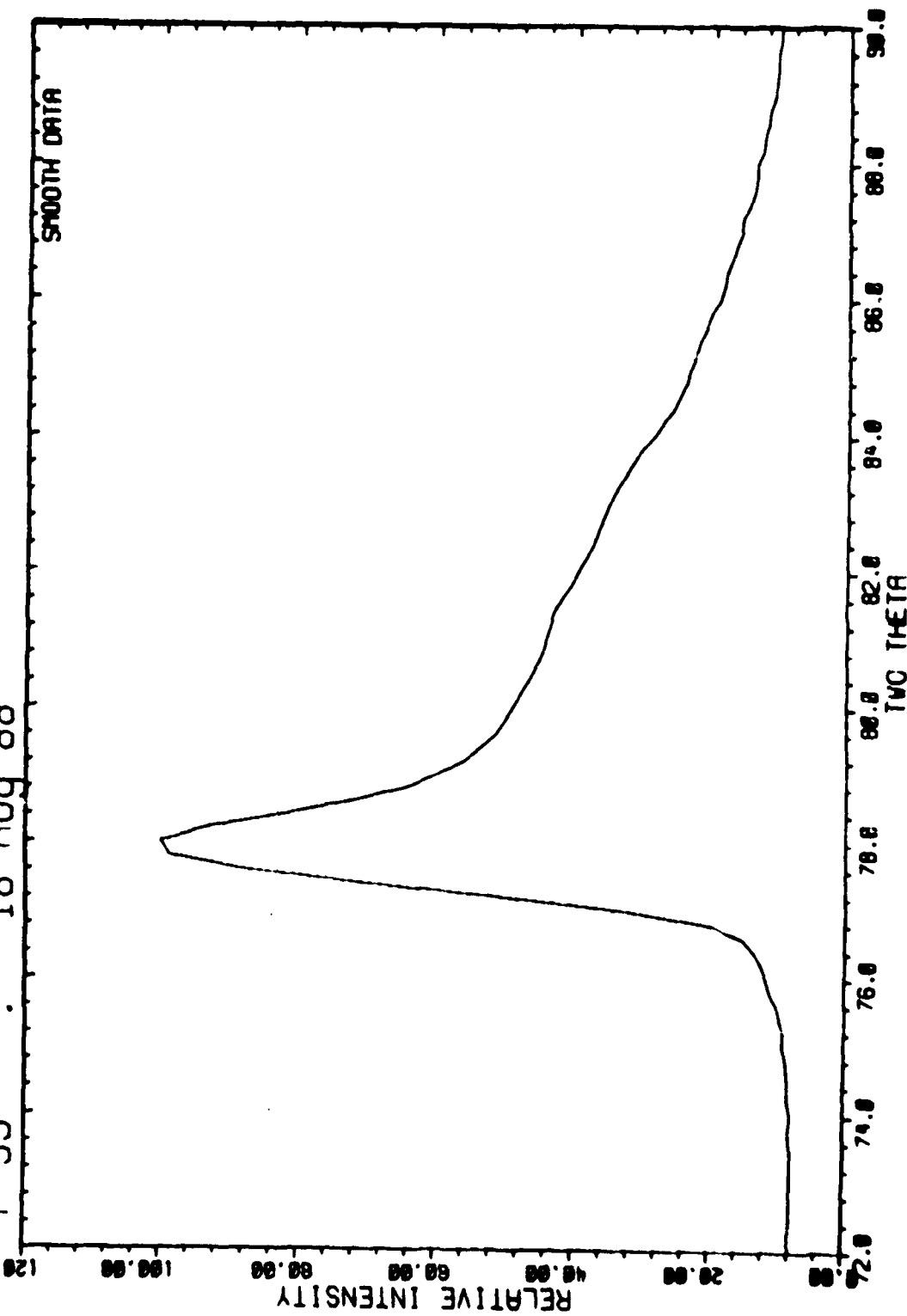
<u>Pitch</u>	<u>PAN</u>	<u>Vapor Grown</u>
P-25	T-300	G45-700
P-55	AS4	HMS
P-75	T-40	T-50
P-100	G40-700	GY-70
P-120		

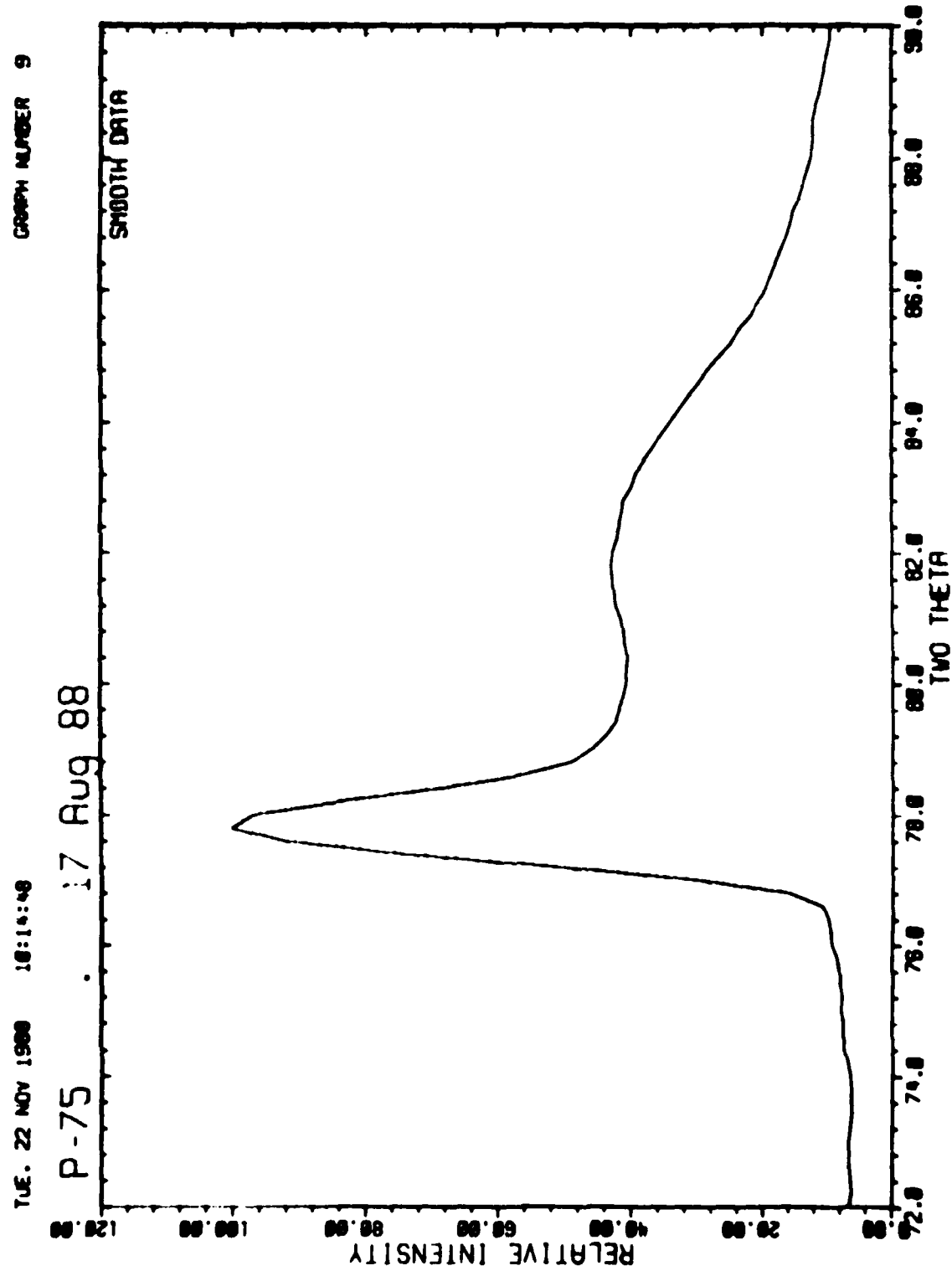


TUE. 22 NOV 1988 :0:12:10

P - 55 . 18 Aug 88

GRAPH NUMBER 6

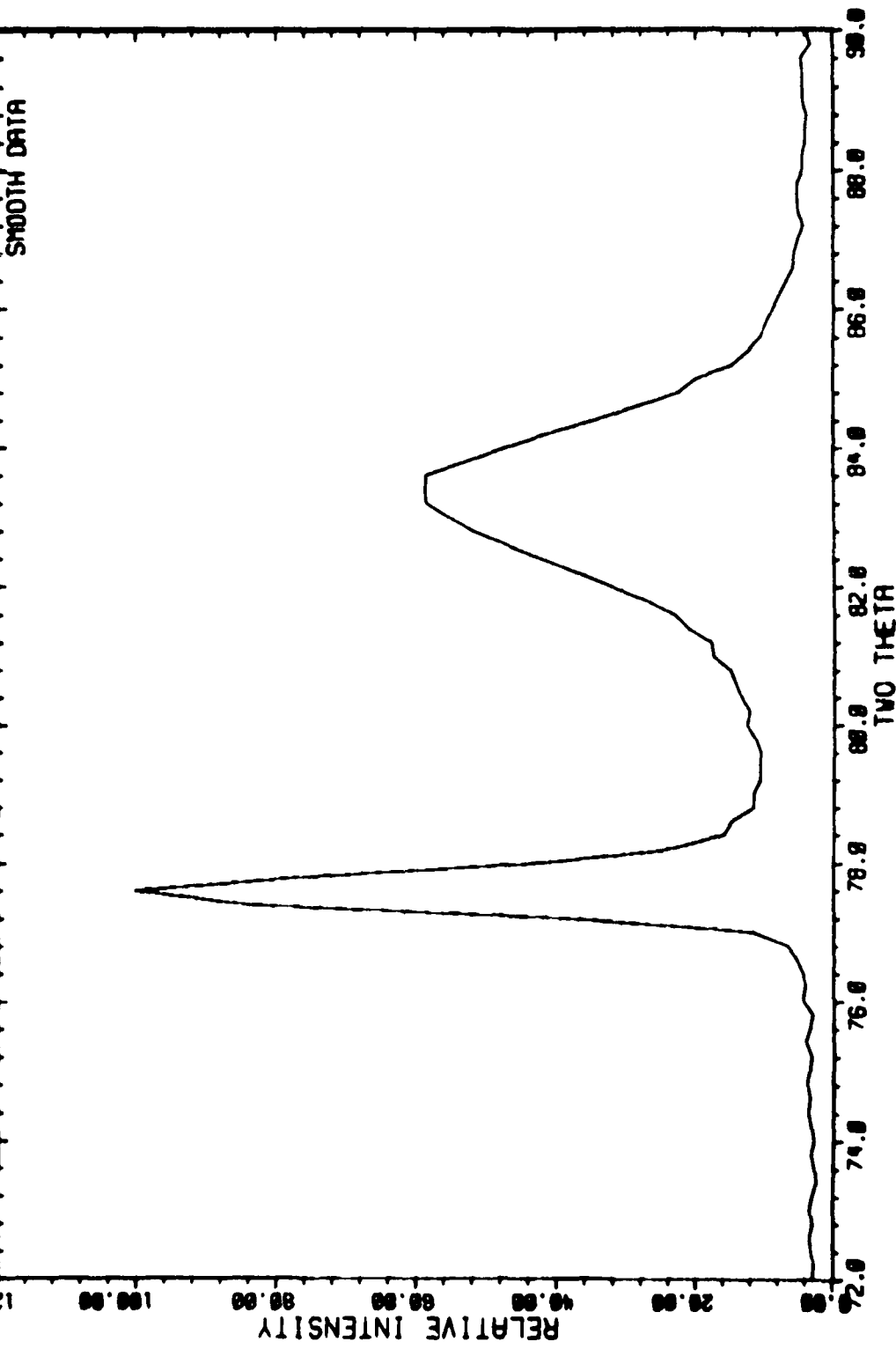


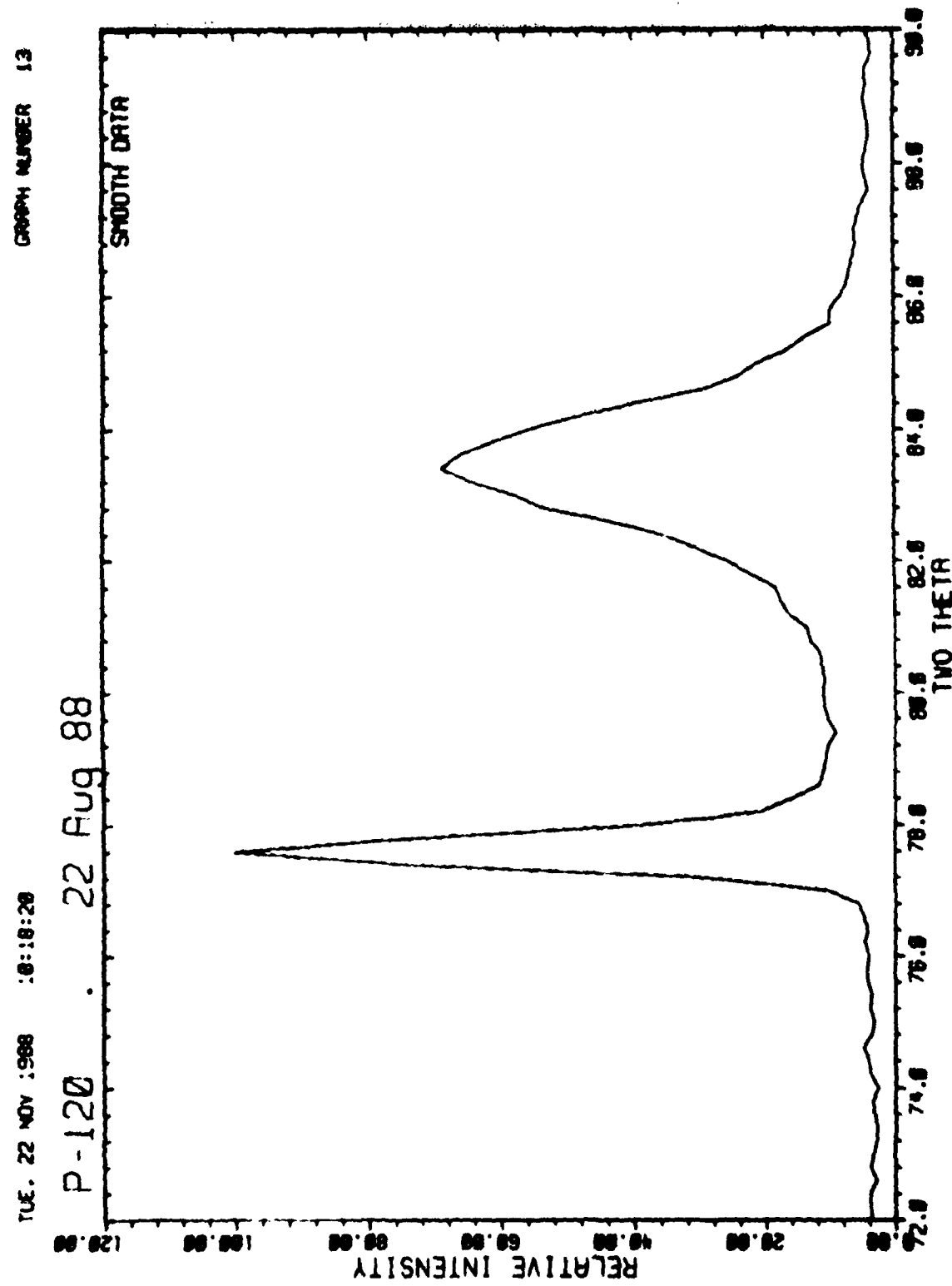


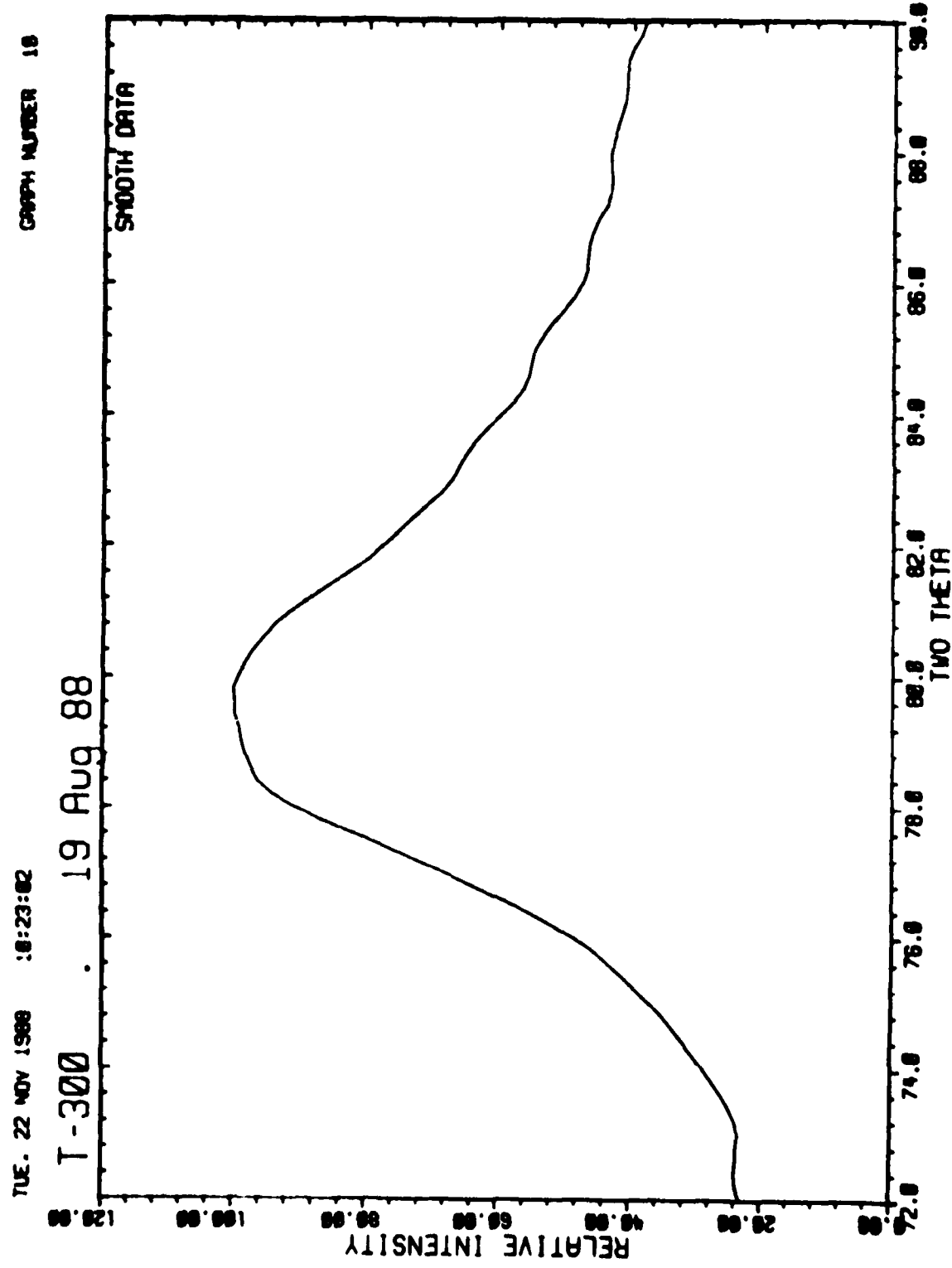
TUE. 22 NOV 1988 12:16:39

P - 100 15 Aug 88

GRAPH NUMBER 11



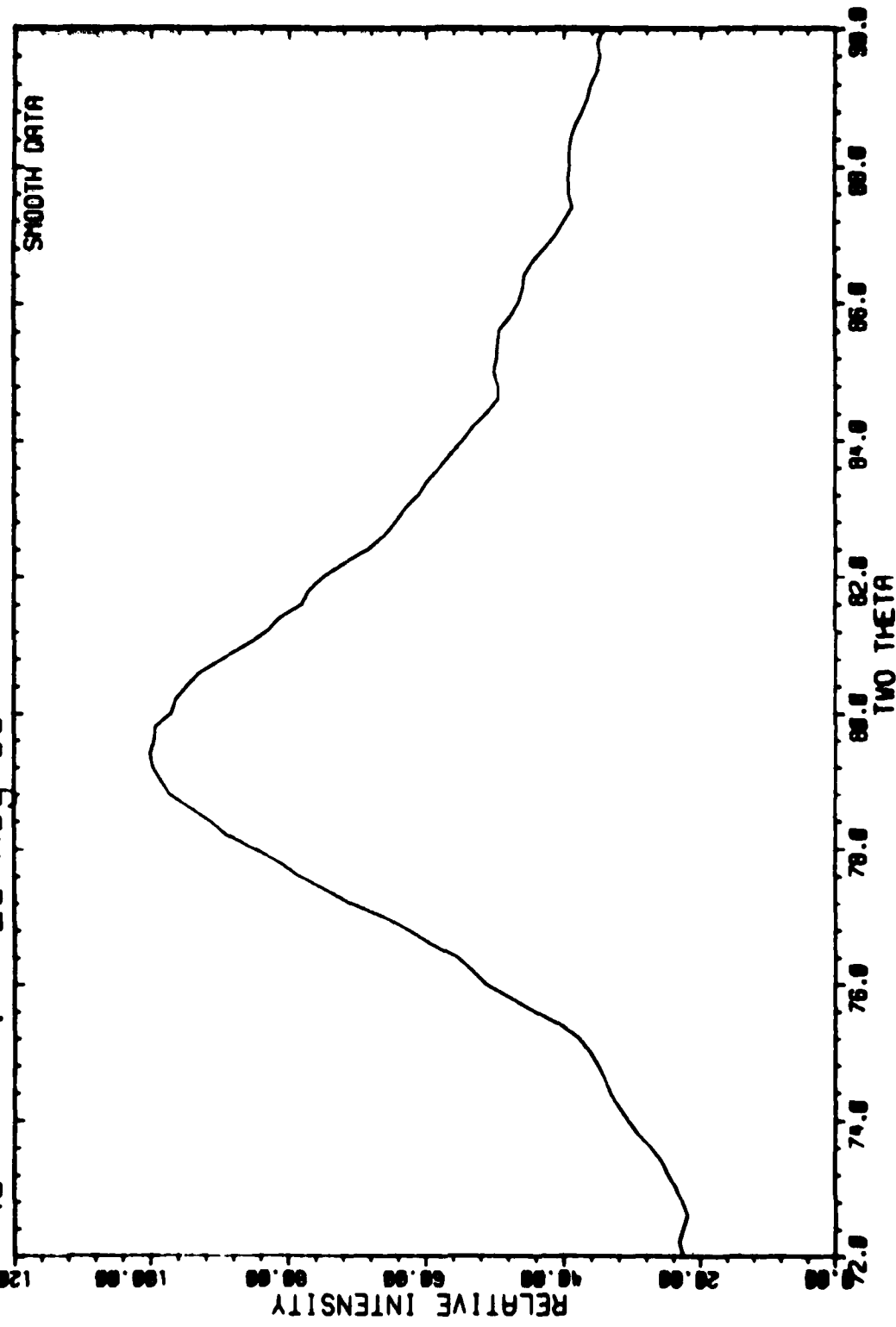




GRAPH NUMBER 29

TUE. 22 NOV. 1988 :06:24:45

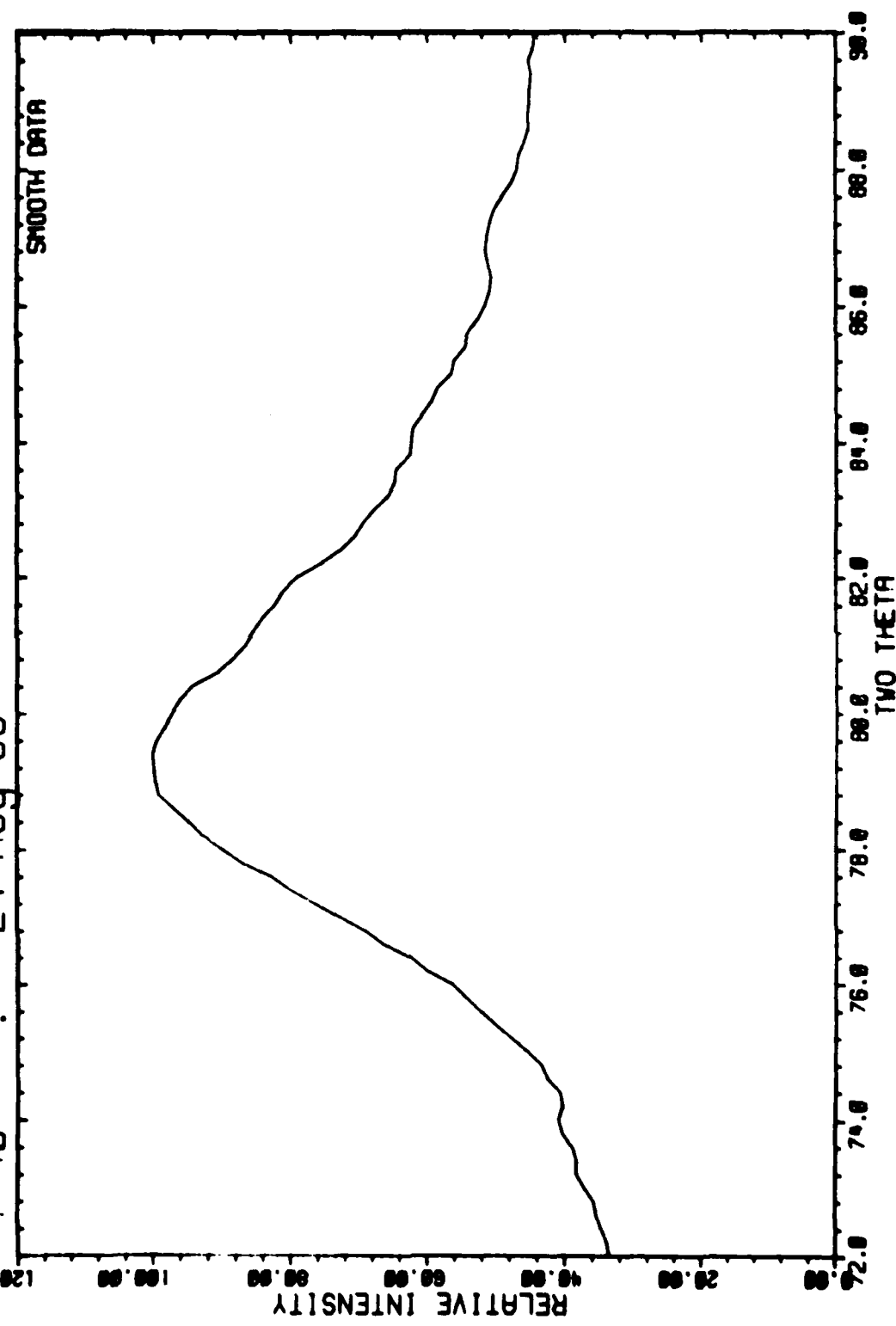
AS-L . 23 Aug 88

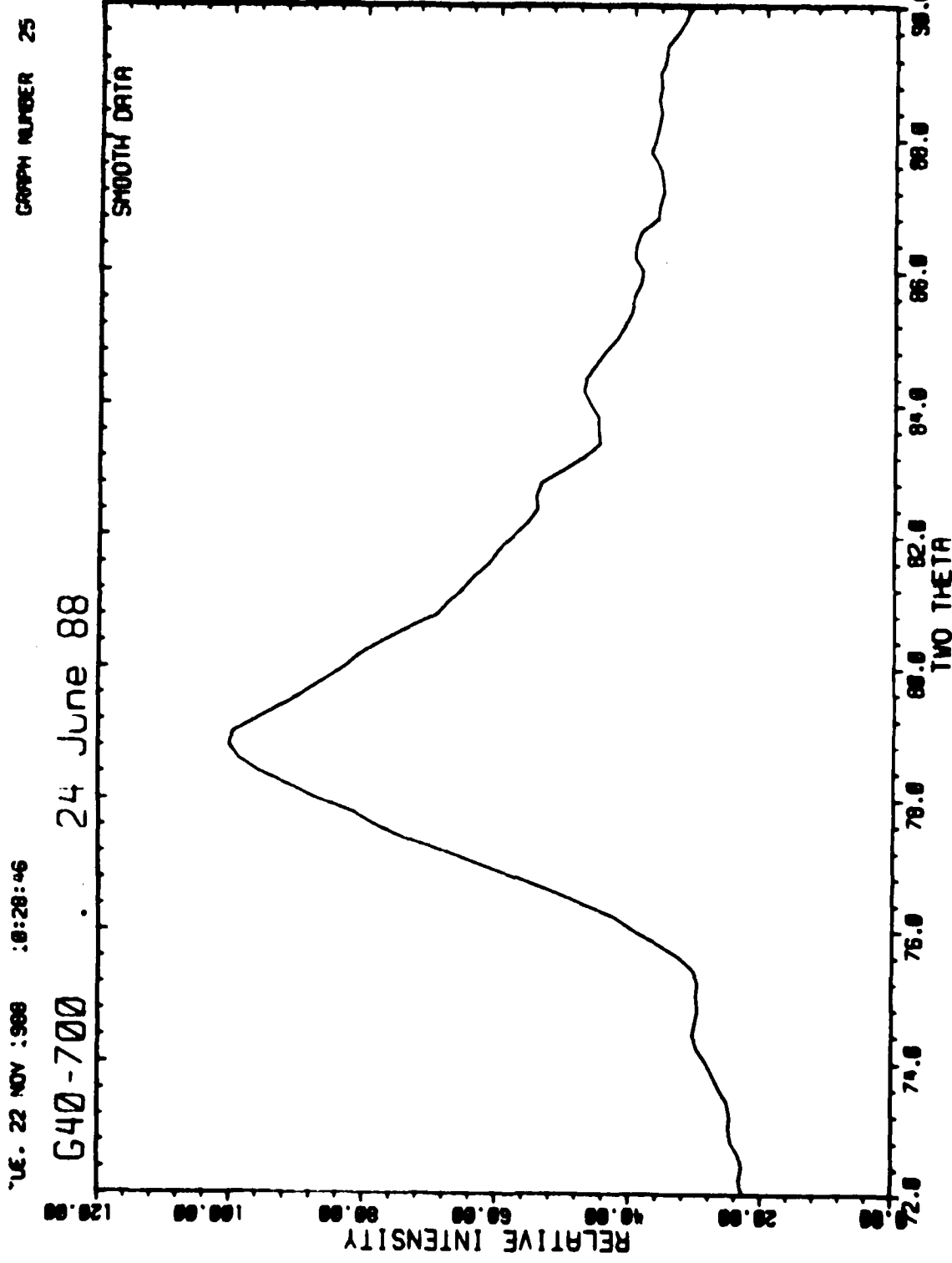


TUE. 22 NOV. 1988 10:27:08

CARD NUMBER 23

L-40 . 24 Aug 88

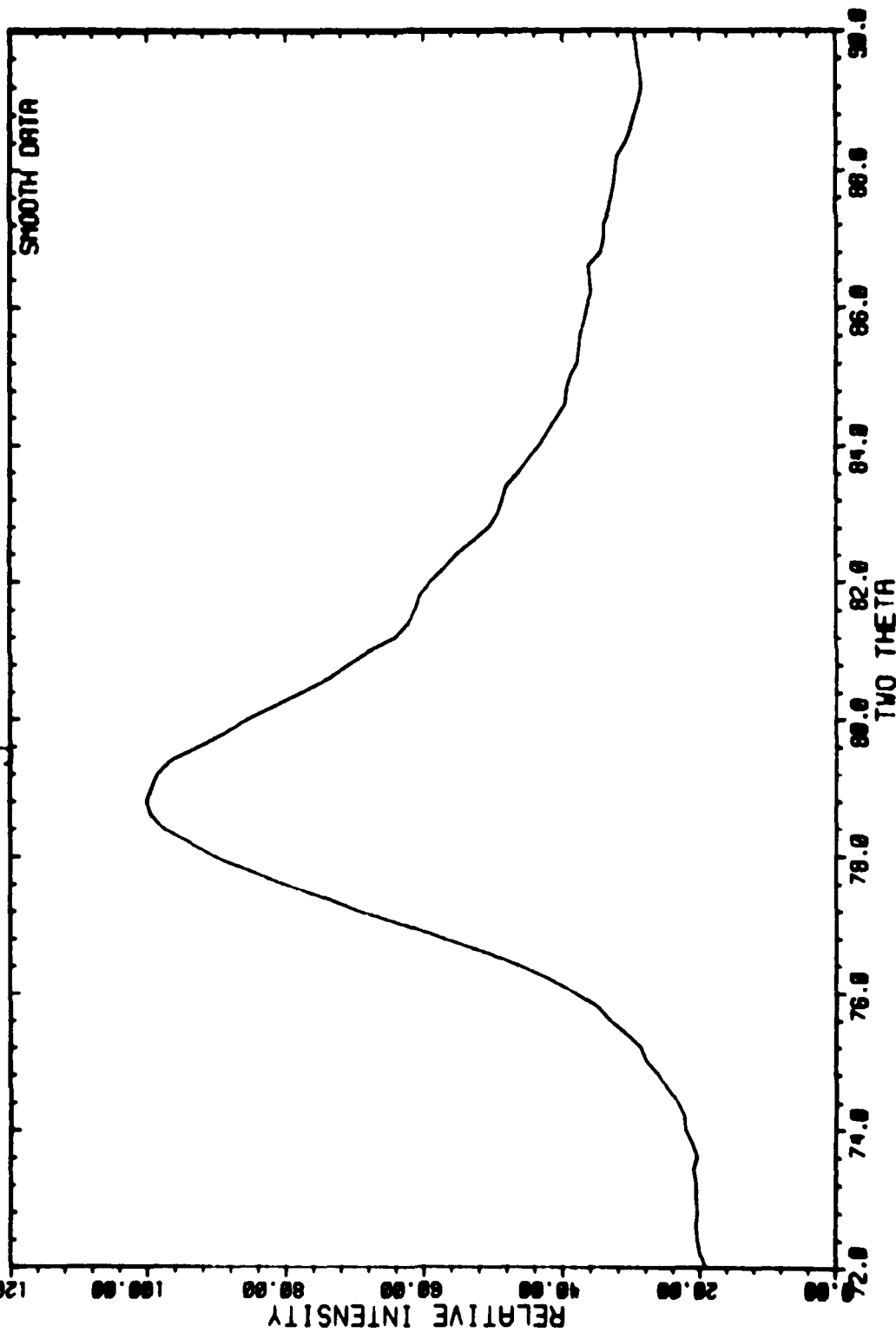




GRAPH NUMBER 27

TUE. 22 NOV 1988 10:32:32

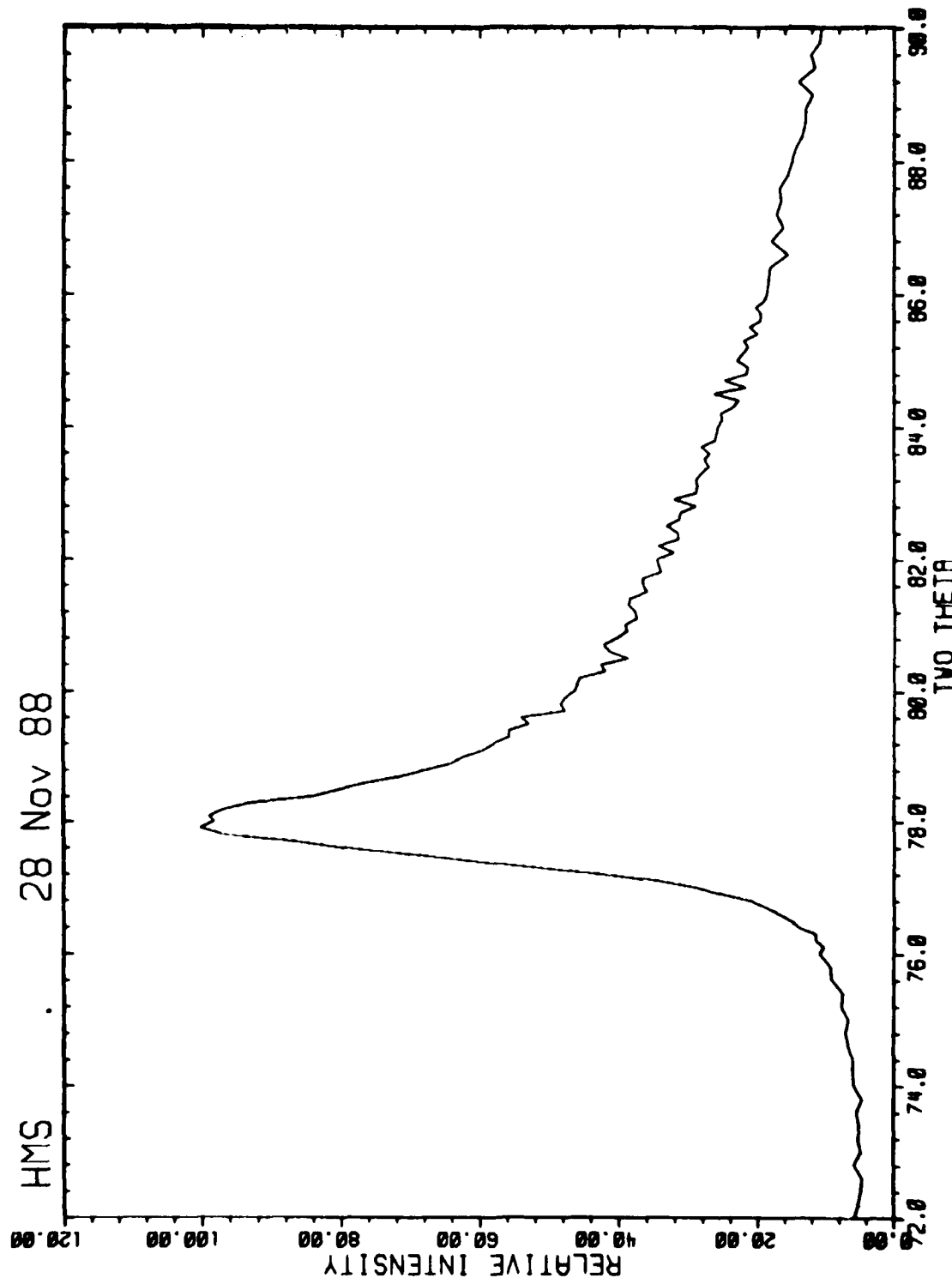
G45-700 19 Aug 88



VED : 15 Mar ; 989 09:29:29

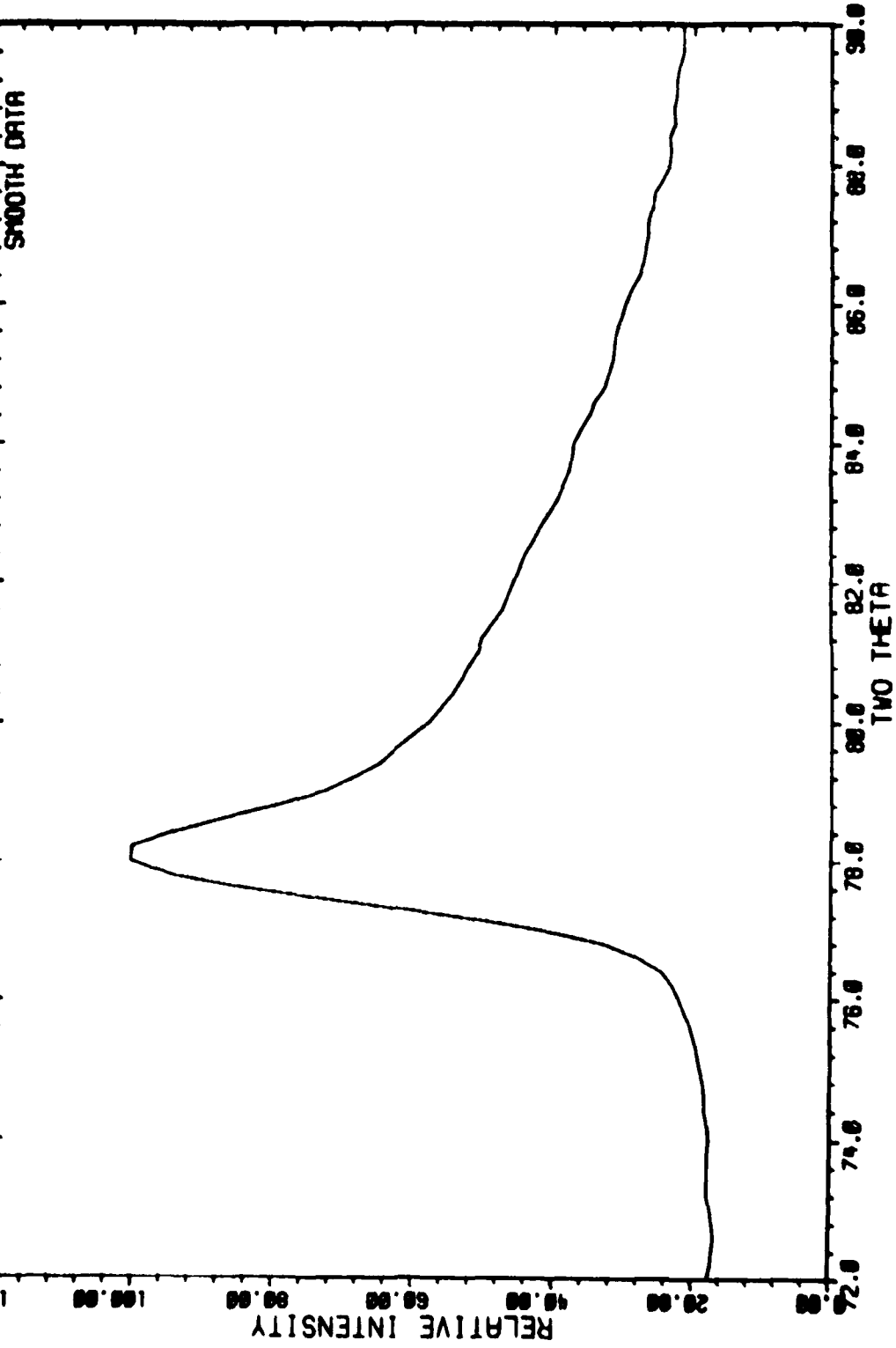
HMS . 28 Nov 88

GRAPH NUMBER 2



GRAPH NUMBER 38

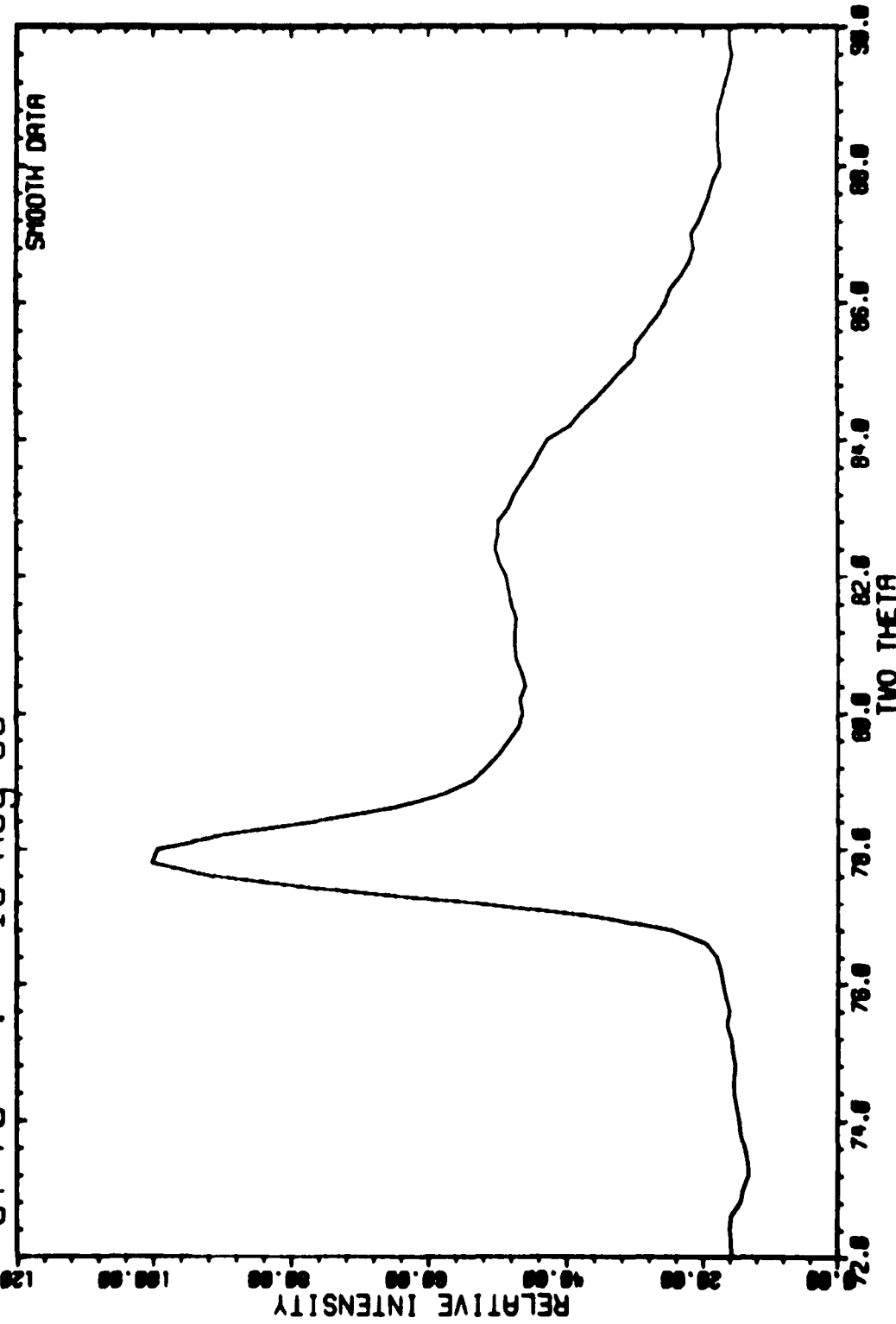
TUE. 22 NOV 1988 . 08:33:00  
T -50 . 23 Aug 88



NE. 22 Nov 1988 16:35:18

GY-70

GRAPH NUMBER 22



GRAPH NUMBER 15

TUE. 22 NOV 1988 10:28:08

FPPPI SCI 8 July 88

